UNIVERSITY OF TRENTO - Italy

Doctoral Programme in Physics

Cycle XXVIII

Solar water splitting for hydrogen production: development of photocatalysts based on earth abundant and biocompatible materials (TiO_2 and Fe_2O_3)

PhD candidate:

Zakaria El koura

Supervisor:

Prof. Antonio Miotello

March 2016

Solar water splitting for hydrogen production: development of photocatalysts based on earth abundant and biocompatible materials (TiO_2 and Fe_2O_3)

by

Zakaria El koura

B.S. in Physics University of Trento, Italy (2010)

M.S. in Experimental Physics University of Trento, Italy (2012)

Thesis submitted to the Doctoral Programme in Physics
in partial fulfilment of the requirements for the degree of
Doctor of Philosophy in Physics

Committee members:

Prof. Maurizio Montagna
University of Trento - Department of Physics, Italy.

Prof. Giovanni Mattei
University of Padova – Department of Physics and Astronomy, Italy.

Dr. Chiara Maurizio
University of Padova – Department of Physics and Astronomy, Italy.

Zakaria El koura, "*Solar water splitting for hydrogen production: development of photocatalysts based on earth abundant and biocompatible materials (TiO_2 and Fe_2O_3)*".

بِسْمِ اللَّهِ الرَّحْمَٰنِ الرَّحِيمِ

A mia madre e a mio padre

A Valentina, mia moglie
e al piccolo tesoro che porta in grembo

Alle future zie:
Safà, Sara, Marua e Nisrin

Abstract

Fossil fuels have been critical to the development of modern society, but concerns over pollution, environmental degradation and climate change demand humans transition to renewable sources of energy. Solar energy is, among renewables, by far the largest exploitable resource, providing more energy in 1 hour to the earth than all of the energy consumed by humans in an entire year. The principal problem related to solar energy use is its intermittency. Collecting and storing solar energy in chemical bonds (solar fuel), as nature accomplishes through photosynthesis, is possible through photo-electrochemical water splitting, a clean and sustainable way for hydrogen production. The materials used as photo-electrodes in a photo-electrochemical cell must fulfil a variety of thermodynamic and kinetic requirements to ensure good efficiency and durability. Since there is no material in nature satisfying all these requirements, tailoring the optical, electrical, and morphological properties of the existing materials to construct photo-electrodes with the desired performance is a big task for materials scientists. In this thesis, we study TiO_2 based photo-catalysts and Fe_2O_3 based water oxidation catalysts. TiO_2 thin films were deposited by radio frequency magnetron sputtering technique and their optical, electrical and morphological properties were changed to enhance the visible light absorption and/or limit the recombination rate of charge carriers. More specifically, the effect of compensated (V and N) and non compensated (Cu and N) n-p codoping of TiO_2 was studied. The role of coupling TiO_2 thin films with indium tin oxide films in single and multilayer structures, compact and porous morphologies was underlined. The effect of hydrogen doping in passivating dangling bonds in TiO_2 was demonstrated. Fe_2O_3 nanoparticles assembled coatings were synthesized by pulsed laser deposition and studied for the functionalization of electrodes and absorbers surfaces as water oxidation catalysts. The response of the optical and electrochemical properties of the coating to the tuning of film morphology was studied, ranging from a low-transmittance compact layer to a porous nanoparticle-assembled coating, which resulted to be highly transparent. Materials properties

were characterized by various techniques such as Raman spectroscopy, x-ray diffraction, UV-vis spectroscopy, x-ray photoelectron spectroscopy, energy dispersive x-ray spectroscopy, and scanning electron microscopy. Electrochemical and photo-electrochemical properties of the samples were studied by testing them as electrodes in a photoelectrochemical cell. Both materials were chosen because they are widespread, non-hazardous, biocompatible and scalable. This enables the large-scale application of photo-electrochemical water splitting and the full exploitation of the green potential of this technology.

Thesis Outline

The main body of this thesis can be divided into three parts. The first part is introductive and comprises the first two chapters. **Chapter 1** gives a general overview on the energetic and environmental problem, and underlines the importance and urgency of switching to a green and sustainable economy. The great potential of solar water splitting for hydrogen production is pointed out. **Chapter 2** describes the working principles of a photo-electrochemical cell and lists the main requirements that a photo-electrode should fulfil to ensure a good performance (efficiency and stability). Moreover, it introduces briefly the two selected materials and explains the reasons of the choice.

The second part of the thesis includes chapters from 3 to 6 and presents the work done on TiO_2 based photo-electrodes. **Chapter 3** deals with V and N codoping of TiO_2, which is a compensated n-p codoping. The role of indium tin oxide/ TiO_2 interface in enhancing the charge separation is explained along with the efficacy of the multilayer structure. **Chapter 4** is focused on the fabrication and characterization of mesoporous ITO/TiO_2 thin films. The enhanced electrochemical properties are explained in terms of increased surface area and improved charge transfer properties. **Chapter 5** concerns the fabrication of H-doped Anatase TiO_2 and the study of the effect of H inclusion on TiO_2 properties. In **Chapter 6**, the effect of Cu and N codoping (non-compensated n-p codoping) on the optical, electrical, and photo-electrochemical properties of TiO_2 is investigated.

The third part of the thesis presents the work done on iron oxide water oxidation catalysts and is formed by chapters 7 and 8. In **chapter 7**, we study the validity of pulsed laser deposition for the functionalization of indium tin oxide surface with iron oxide coatings. The resulting electrodes showed enhanced electro-activity towards water oxidation. In **chapter 8**, the response of the optical and electrochemical properties of the coating to the tuning of film

morphology is studied. PLD coatings with different properties were coupled with hematite-based absorbers and their performances were compared.

Concluding remarks and future perspectives are summarized in the **Conclusions** chapter. Two appendixes follow, where a detailed description of the deposition techniques (**Appendix A**) and characterization techniques (**Appendix B**) employed in this thesis are given.

Contents

Chapter 1

Climate change and renewable energy

The supply of secure, clean and sustainable energy is arguably the most important scientific and technical challenge facing humanity in the 21st century. At the present time, the rate of global energy consumption is in the region of 18.5 TW [1]. In future, this global value will rise owing to industrialization in underdeveloped and developing countries coupled with increasing world population. Based on current projections, the global annual energy consumption rate will reach 27 TW by 2050 and almost 50 TW by the end of the century [2]. About 85 per cent of the total global energy consumed at present comes from burning fossil fuels. Future energy demand could also be met, in principle, from fossil fuels, particularly coal. Indeed, many sources indicate there are ample fossil energy reserves, in one form or another, to supply the future energy demand at the expected consumption rate for at least several centuries [3]. However, consumption of fossil energy at that rate would result in significant greenhouse gas emissions, in particular carbon dioxide, with irreversible effects on global climate. Therefore, meeting global energy demand in a sustainable fashion will require not only increased energy efficiency and new methods of using existing carbon-based fuels but also a daunting amount of new carbon-neutral energy.

To use Ban Ki-moon's words at "Conference on Energy for All: Financing Access for the Poor", held in Oslo (Norway) in 2011: "*We cannot continue to burn our way to prosperity. The only way to minimize the risks of dangerous climate change is by ensuring that energy is sustainable. In short, we need a clean energy revolution. … Saving our planet, lifting the poor from poverty, and advancing economic growth for all are one and the same cause. Sustainable energy for all is critical for human progress – health, education, security, job generation, and economic competitiveness*."

A replacement for fossil fuels will not appear overnight. Extensive research and development is required before alternative sources can supply energy in quantities and at costs competitive with fossil fuels. Moreover, making those alternative sources available commercially will itself require developing the proper economic infrastructure.

1.1 Climate change

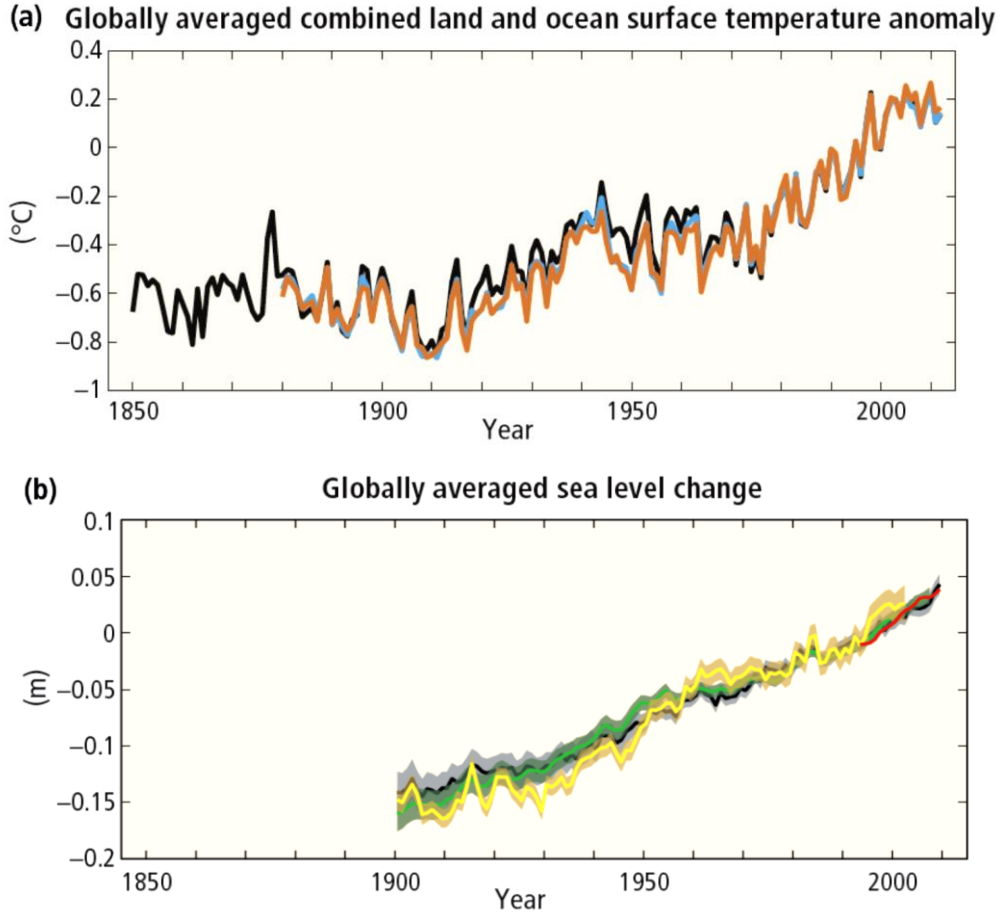

Figure 1.1: Observations of a changing global climate system: (a) annually and globally averaged combined land and ocean surface temperature anomalies relative to the average over the period 1986 to 2005. Colours indicate different data sets. (b) Annually and globally averaged sea level change relative to the average over the period 1986 to 2005 in the longest-running dataset. Colours indicate different data sets. All datasets are aligned to have the same value in 1993, the first year of satellite altimetry data (red). Where assessed, uncertainties are indicated by coloured shading (source [4]).

Multiple lines of scientific evidence show that the climate system is warming [5]. Although the increase of near-surface atmospheric temperature is the measure of global warming often reported in the popular press, most of the additional energy stored in the climate system since

1970 has gone into ocean warming. The remainder has melted ice, and warmed the continents and atmosphere [6].

Five observed changes in the climate system are described in the Climate Change 2014: Synthesis Report [4]:

1. **Earth's surface warming**: multiple independently produced datasets show that the globally averaged combined land and ocean surface temperature data as calculated by a linear trend show a warming of 0.85 ± 0.08 °C, over the period 1880 to 2012 (*figure 1.1a*). Each of the last decades has been successively warmer at the Earth's surface than any preceding decade since 1850.
2. **Ocean surface salinity variation measurements** provide indirect evidence for changes in the global water cycle over the ocean due to ocean warming and increase of precipitations. Data show that regions of high salinity, where evaporation dominates, have become more saline, while regions of low salinity, where precipitation dominates, have become fresher since the 1950s.
3. **Acidification of the ocean:** the pH of ocean surface water has decreased by 0.1, corresponding to a 26% increase in acidity, measured as hydrogen ion concentration. This happened because of the oceanic uptake of CO_2, since the beginning of the industrial era.
4. **Glaciers melting:** over the period 1992 to 2011, the Greenland and Antarctic ice sheets have been losing mass, likely at a larger rate over 2002 to 2011. Glaciers have continued to shrink almost worldwide. Northern Hemisphere spring snow cover has continued to decrease in extent. There is high confidence that permafrost temperatures have increased in most regions since the early 1980s in response to increased surface temperature and changing snow cover.
5. **Rise of global mean sea level:** Over the period 1901 to 2010, global mean sea level rose by 0.19 ± 0.01 m (*figure 1.1b*). The rate of sea level rise since the mid-19th century has been larger than the mean rate during the previous two millennia.

Many of the observed changes since the 1950s are unprecedented over decades to millennia [7]. These changes in climate have caused impacts on natural and human systems on all continents and across the oceans. Evidence of observed climate change impacts is stronger and more comprehensive for natural systems. Many terrestrial, freshwater and marine species have shifted their geographic ranges, seasonal activities, migration patterns, abundances and species

interactions in response to ongoing climate change. Impacts from recent climate-related extremes, such as heat waves, droughts, floods, cyclones and wildfires, reveal significant vulnerability and exposure of some ecosystems and many human systems to current climate variability.

1.1.1 What are the causes of climate change?

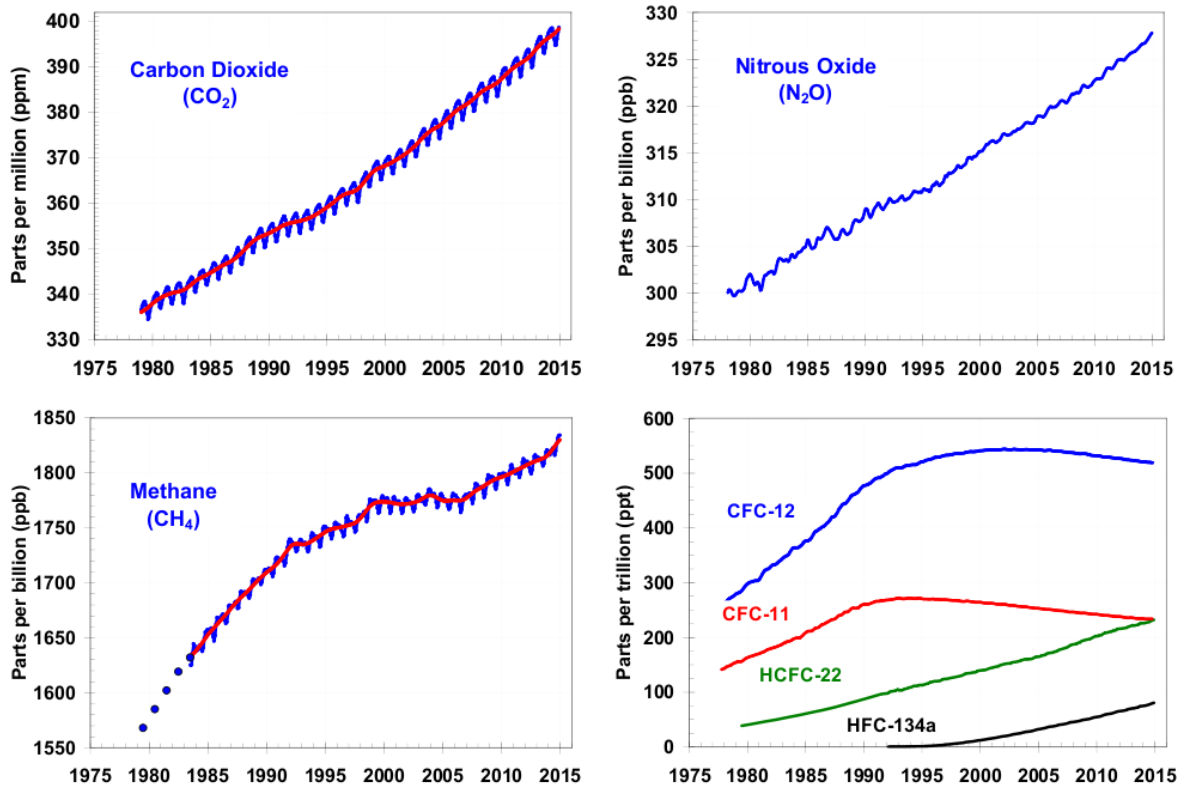

Figure 1.2: Global average abundances of the major, well-mixed, long-lived greenhouse gases - carbon dioxide, methane, nitrous oxide, CFC-12 and CFC-11 - from the NOAA global air sampling network are plotted since the beginning of 1979. These five gases account for about 96% of the direct radiative forcing by long-lived greenhouse gases since 1750. The remaining 4% is contributed by an assortment of 15 minor halogenated gases including HCFC-22 and HFC-134a, for which NOAA observations are also shown in the figure. Methane data before 1983 are annual averages from D. Etheridge [Etheridge et al., 1998], adjusted to the NOAA calibration scale [Dlugokencky et al., 2005]. (Source: [8])

The view that human activities are likely responsible for most of the observed increase in global mean temperature ("global warming") since the mid-20th century is an accurate reflection of current scientific thinking. The Intergovernmental Panel on Climate Change (IPCC) reported [4] that scientists are more than 95% certain that global warming is being caused mostly by increasing concentrations of greenhouse gases and other anthropogenic activities (deforestation, overfishing, intensive agriculture, land degradation…). In particular, more than half of the observed increase in global average surface temperature from 1951 to 2010 was

caused by the anthropogenic increase in greenhouse gas (GHG) concentrations and changes in land-use. Anthropogenic GHG emissions since the pre-industrial era have driven large increases in the atmospheric concentrations (*figure 1.2*) of carbon dioxide (CO_2), methane (CH_4) and nitrous oxide (N_2O), which have reached levels that are unprecedented in at least 800,000 years [9].

1.1.2 Carbon dioxide

Carbon dioxide (CO_2) is the primary greenhouse gas emitted through human activities (*figure 1.3*). In 2010, CO_2 accounted for about 76% [4] of the total emissions. Carbon dioxide is naturally present in the atmosphere as part of the Earth's carbon cycle. Human activities are altering this cycle both by adding more CO_2 to the atmosphere and by influencing the ability of natural sinks, like forests, to remove CO_2 from the atmosphere. Therefore, although CO_2 emissions come from a variety of natural sources, human-related emissions are responsible for the increase that has occurred in the atmosphere since the industrial revolution [10].

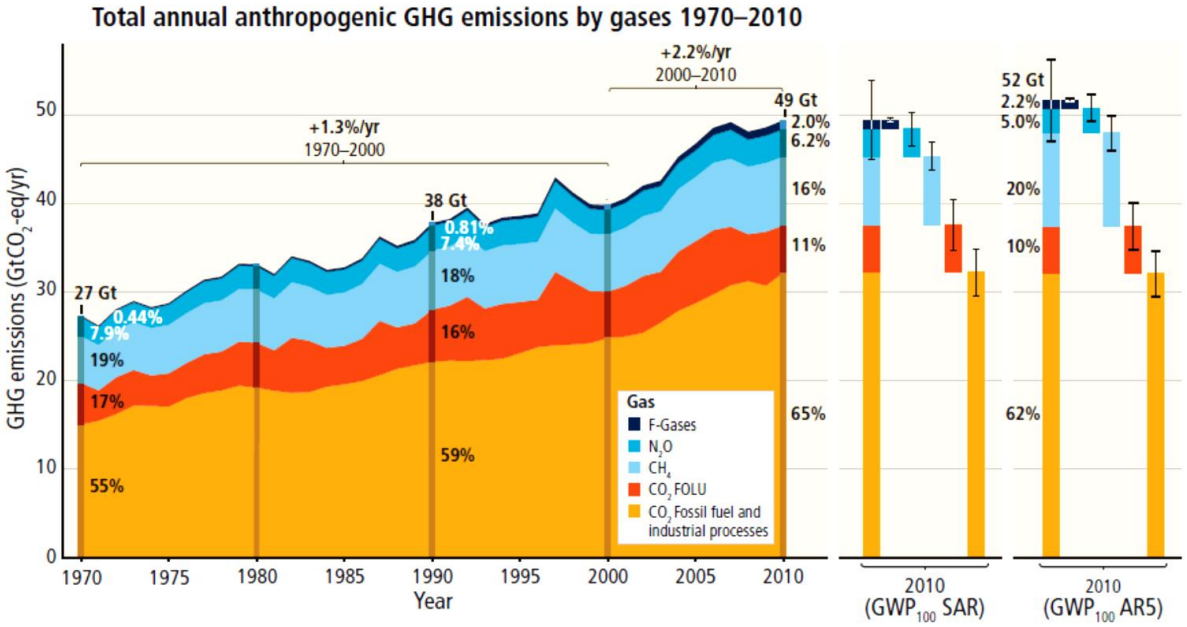

Figure 1.3: Total annual anthropogenic greenhouse gas (GHG) emissions (gigatonne of CO_2-equivalent per year, $GtCO_2$-eq/yr) for the period 1970 to 2010 by gases: CO_2 from fossil fuel combustion and industrial processes; CO_2 from Forestry and Other Land Use (FOLU); methane (CH_4); nitrous oxide (N_2O); fluorinated gases covered under the Kyoto Protocol (F-gases). Right hand side shows 2010 emissions, using alternatively CO_2-equivalent emission weightings based on IPCC Second Assessment Report (SAR) and AR5 values. (Source [4])

Cumulative anthropogenic CO_2 emissions to the atmosphere were 2040 ± 310 $GtCO_2$, between 1750 and 2011. About 40% of these emissions have remained in the atmosphere (880

± 35 $GtCO_2$); the rest was removed from the atmosphere and stored on land (in plants and soils) and in the ocean. The ocean has absorbed about 30% of the emitted anthropogenic CO_2, causing ocean acidification. About half of the anthropogenic CO_2 emissions between 1750 and 2011 have occurred in the last 40 years, with larger absolute increases between 2000 and 2010, despite a growing number of climate change mitigation policies. Since the start of high-precision instrument measurements of CO_2 in the atmosphere in 1958, the annual mean concentration of CO_2 has continuously increased from one year to the next.

The main human activity that emits CO_2 is the combustion of fossil fuels (coal, natural gas, and oil) for energy and transportation, which contributed about 78% of the total GHG emissions increase from 1970 to 2010, with a similar percentage contribution for the increase during the period 2000 to 2010 [4]. For this reason the most effective way to reduce carbon dioxide (CO_2) emissions is to reduce fossil fuel consumption.

1.1.3 Preventing dangerous climate change

Preventing dangerous anthropogenic interference with the climate system was central to the “IPCC Second Assessment: Climate Change 1995” and in 2002 was incorporated by the United Nations Framework Convention on Climate Change (UNFCCC) as the focus of its formal Framework Convention policy. The problem that arises is to decide what level of interference would lead to "dangerous" change. Since the 1990s, scientists have argued that the most serious consequences of global warming might be avoided if global average temperatures rose by no more than 2 °C above pre-industrial levels (1.4 °C above present levels). In 2005 an international conference called "*Avoiding Dangerous Climate Change: A Scientific Symposium on Stabilisation of Greenhouse Gases*" examined the link between atmospheric greenhouse gas concentration, and the 2 °C ceiling on global warming. Previously, this had generally been accepted as being 550 ppm (parts per million) [11]. The conference concluded that, at the level of 550 ppm, it was likely that 2 °C would be exceeded, according to the projections of more recent climate models. Stabilising greenhouse gas concentrations at 450 ppm would only result in a 50% likelihood of limiting global warming to 2 °C, therefore it would be necessary to achieve stabilisation below 400 ppm to give a relatively high certainty of not exceeding 2 °C [12].

Rockström and colleagues [13], set an even lower limit for atmospheric concentration of carbon dioxide (350 ppm) and gave three reasons for this boundary:

1. The climate models setting a higher limit do not include long-term reinforcing feedback processes that further warm the climate, such as decrease in the surface area of ice cover or changes in the distribution of vegetation;
2. Paleoclimate data from the past 100 million years show that CO_2 concentrations were a major factor in the long-term cooling of the past 50 million years. Moreover, the planet was largely ice-free until CO_2 concentrations fell below 450 ppm (±100 ppm), suggesting that there is a critical threshold between 350 and 550 ppm
3. Up-to-date global warming has almost reached 1°C, but we are already experiencing effects formerly assumed for 2 °C.

As can be seen from *figure 1.2* the limit proposed by Rockström (350 ppm) has been exceeded since 1988.

1.1.4 Future perspectives

In 2014 the mean concentration of CO_2 reached the value of 398.55 (Mauna Loa Observatory), with a growth of just 0.5% relative to 2013, although economic growth has been of about 3%. This is the weakest growth in CO_2 emissions since 1998 and is a sign that economic growth and carbon dioxide emissions, which have historically moved in the same direction, are starting to decouple. However, this is still not enough, because, due to the very slow removal processes, atmospheric CO_2 will continue to increase in the long term even if emissions are substantially reduced from present levels. For this reason, human-induced warming of the climate is expected to continue throughout the 21st century and beyond, independent from the followed climate policy and socio-economic development. Nevertheless, if no efficient policies will be stated and followed, the temperature will rise up to more than 5 °C by 2100 [4], as related to preindustrial level, with dangerous consequences on our planet. The only way to keep the global warming below 2 °C is by following a development with net negative emissions, which means reducing the emissions as much as possible (e.g. using bio-energy) and sequestrating GHGs, for example with reforestation and CO_2 capture and storage [4].

The greenhouse gas reduction measures for the period from 2008 to 2012 were agreed in the Kyoto Protocol in 1997. The scope of the protocol was extended until 2020 with the Doha Amendment in 2012. The 21st Conference of the Parties of the UNFCCC was held in Paris from 30th November to 12th December 2015 with the aim to achieve, for the first time in over 20 years of UN negotiations, a binding and universal agreement on climate, from all the nations of

the world. On 12th December 2015, the participating 195 countries agreed, by consensus, to the final global pact, the Paris Agreement, to reduce emissions as part of the method for reducing greenhouse gas [14]. The agreement, that will govern the climate change mitigation measures from 2020, calls for zero net anthropogenic greenhouse gas emissions to be reached during the second half of the 21st century. France's Foreign Minister, Laurent Fabius, said this "ambitious and balanced" plan was a "historic turning point" in the goal of reducing global warming. However, some others criticized the fact that significant sections are "promises" or aims and not firm commitments by the countries. Indeed, no detailed timetable or country-specific goals for emissions were incorporated into the Paris Agreement – as opposed to the previous Kyoto Protocol. Every five years, the implementation of the agreement will be evaluated by all member countries together, with the first evaluation in 2023. The outcome will be used as input for new nationally determined contributions of member states, to achieve the worldwide goals. Thus, the hope is that this first version of the agreement will be strengthened over time.

1.2 Renewable energy resources

In order to stabilize CO_2 concentration at 550 ppm, the projected carbon intensity in 2050 is ca. 0.45 kg of C yr^{-1} W^{-1}, which is lower than that of any of the fossil fuels [2]. The only way to reach this value is through a significant contribution of carbon-free power, namely nuclear and renewables, to the total energy mix. Hence, at least 10 TW carbon-free power is required in 2050 and even more will be required later in the 21st century if CO_2 levels are to be kept below 550 ppm.

1.2.1 Nuclear power

Using conventional nuclear fission to obtain 10 TW would use up all of the terrestrial U resources in few decades. For this reason nuclear power is not a viable route, at least in the near term. Fusion power, indeed, might possibly provide significant commercial energy late in the 21st century. However, this technology is still in early stages of development and cannot provide a significant contribution to the amount of carbon neutral energy production needed to meet any reasonable atmospheric CO_2 concentration target in the next 40 – 50 years.

1.2.2 Renewables

The need for clean energy can be fulfilled by using an array of renewable options: hydropower, biomass, geothermal, ocean thermal energy conversion, waves, tides, wind, solar, etc. It is

extremely unlikely that one particular type of renewable energy will solve the world's energy problems. To meet the terawatt challenge all renewables should be exploited.

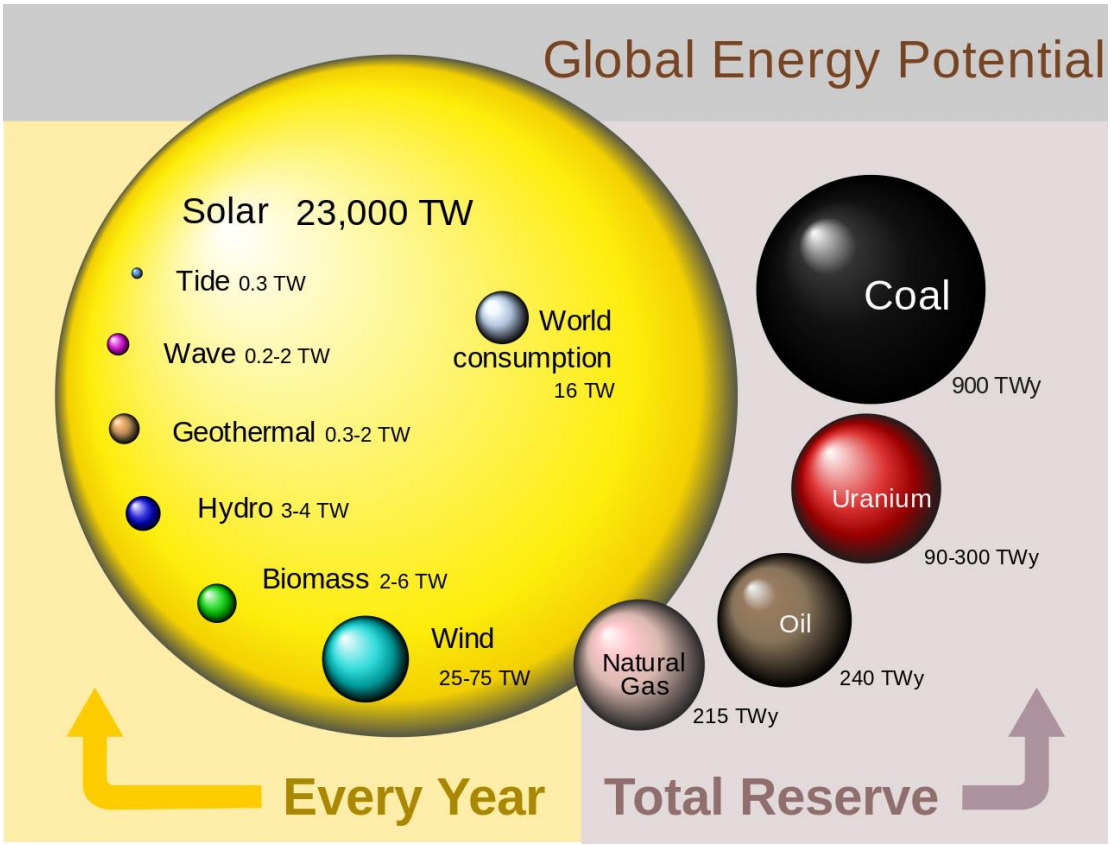

Figure 1.4: Comparing finite and renewable planetary energy reserves (Terawatt-years). The volume of each sphere represents the total amount of energy recoverable from the finite reserves and the energy recoverable per year from renewable sources (2009) [15]. Updated data: in 2014 world energy consumption was 18.3 TW, wind 75 – 130 TWy/y, geothermal 0.2 – 3 TWy/y, natural gas 220 TWy, petroleum 335 TWy, uranium 185 TWy, coal 830 TWy [1].

However, some resources have a greater potential than others in terms of how much energy they could contribute. *Figure 1.4* shows 2009 estimate renewable planetary energy reserves, for the sake of completeness also non-renewable energy reserves are reported. Total recoverable reserves are shown for the finite resources, whereas yearly potential is shown for the renewables. The comparison clearly shows that renewable sources are not all equivalent by far. The solar resource is orders of magnitude larger than all the others combined. Wind energy could probably supply all of the planet's energy requirements if pushed to a considerable portion of its exploitable potential. However, none of the others (most of which are first and second order by-products of the solar resource) could, alone, meet the demand. On the other hand, exploiting only a very small fraction of the earth's solar potential could meet the demand with considerable room for growth. In November 2015 these data have been updated, however

the global picture is basically unchanged [1]. Therefore, the desired economically and environmentally sustainable energy mix of the future should be essentially solar-based.

1.3 Solar water splitting

1.3.1 Artificial photosynthesis

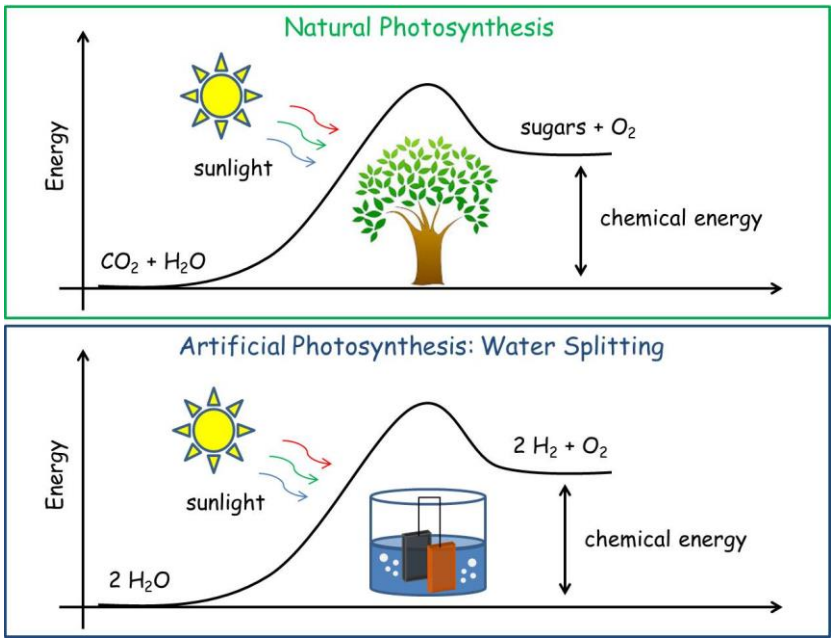

Figure 1.5: Natural (top) and artificial photosynthesis (bottom).

Solar energy is a decentralized and inexhaustible natural resource, providing more energy in 1 hour to the earth than all of the energy consumed by humans in an entire year [16]. However, because of daily and seasonal variability, if solar energy is to be a major primary energy source, then it must be converted and stored to be used on demand. The conversion of solar energy into useful energy forms can generally be divided into thermal and photonic processes. In solar thermal processes, solar energy is first converted to heat, which can either be used directly, stored in a thermal medium (e.g. water or dry rocks) or converted to mechanical and/or electrical energy by an appropriate machine (e.g. a steam turbine for the generation of electricity). In solar photonic processes, the solar photons are absorbed directly into an absorber, without complete conversion to heat. The absorber may convert part of the photon energy in an endergonic chemical reaction, as in photosynthesis [17]. At the heart of the photosynthetic process is the splitting of water by sunlight into oxygen and hydrogen equivalents. The oxygen is released into the atmosphere where it is available for living

organisms to breathe and for burning fuels to drive our technologies. The hydrogen equivalents are used to reduce CO_2 to sugars and other organic molecules of various types. Recombination of the reduced fuel with released oxygen would then regenerate the original species, closing the cycle in a carbon-neutral fashion. The success of photosynthesis as an energy-generating and -storage system stems from the fact that the raw materials and power needed for the synthesis of biomass are available in almost unlimited amounts: sunlight, water and CO_2. The scientific challenge is to construct an 'artificial leaf' able to efficiently capture and convert solar energy and then store it in the form of chemical bonds of a reduced fuel, replicating the natural process (*figure 1.5*). With the development of catalysts able to reproduce the key steps of photosynthesis, water and sunlight would ultimately be the only needed sources for clean energy production.

The need and possibility to achieve artificial photosynthesis was anticipated by the Italian chemist Giacomo Ciamician about one century ago [18]: "*Where vegetation is rich, photochemistry may be left to the plants and by rational cultivation, as I have already explained, solar radiation may be used for industrial purposes. In the desert regions, unadapted to any kind of cultivation, photochemistry will artificially put their solar energy to practical uses. On the arid lands there will spring up industrial colonies without smoke and without smokestacks; forests of glass tubes will extend over the plants and glass buildings will rise everywhere; inside of these will take place the photochemical processes that hitherto have been the guarded secret of the plants, but that will have been mastered by human industry which will know how to make them bear even more abundant fruit than nature, for nature is not in a hurry and mankind is. And if in a distant future the supply of coal becomes completely exhausted, civilization will not be checked by that, for life and civilization will continue as long as the sun shines! If our black and nervous civilization, based on coal, shall be followed by a quieter civilization based on the utilization of solar energy, that will not be harmful to progress and to human happiness"*.

The "Holy Grail" of solar energy conversion and storage is the photoelectrolysis of water using semiconductors as both the light absorber and energy converter, to store solar energy in the simplest chemical bond: H_2 [19]. This method of sustainable hydrogen production is a key objective in the development of alternative energy systems of the future [20]. It is also predicted to be one of the more, if not the most, efficient ways of obtaining hydrogen from water [21].

1.3.2 Hydrogen fuel

Hydrogen is the most abundant element in the universe, however, naturally occurring molecular hydrogen is rare on Earth because hydrogen readily forms compounds with most elements and is present in the water molecule and in most organic compounds. Since hydrogen has to be produced from these compounds it is an energy carrier (similar to electricity) and not an energy resource.

Hydrogen gas is a clean and non-toxic renewable fuel. When it burns, it releases only water vapour to the environment:

$$H_2 + O_2 \longrightarrow H_2O + \text{energy}$$

Moreover, hydrogen contains much larger chemical energy per mass (142 MJ) than any other hydrocarbon fuel. For example, it has nearly three times the energy content of gasoline (48.6 MJ/Kg).

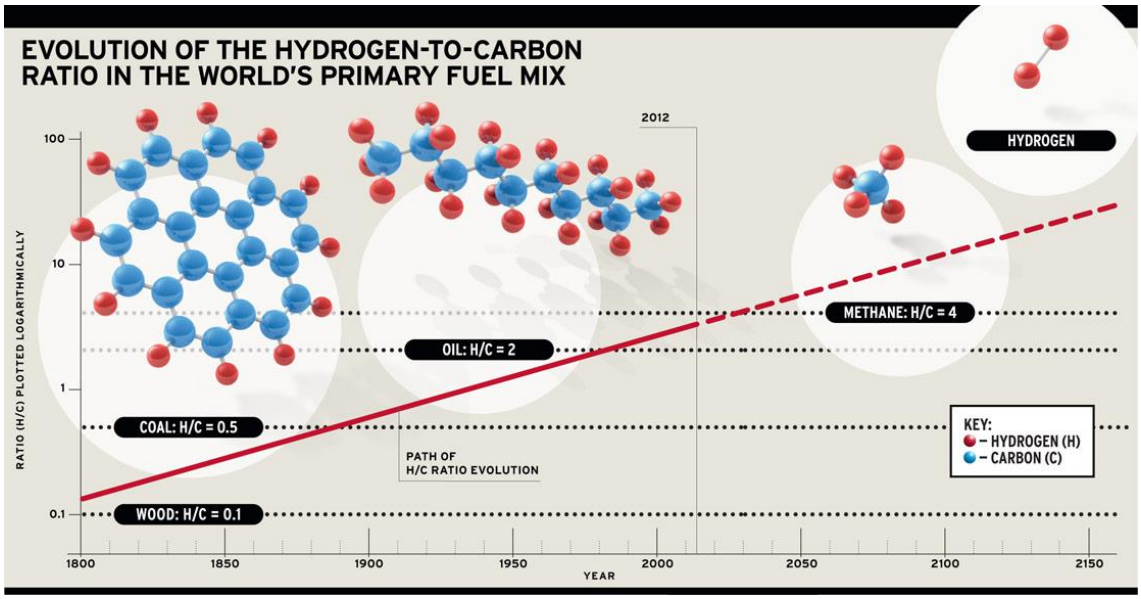

Figure 1.6: Evolution of the hydrogen-to-carbon ratio in the world's primary fuel mix.

The shift to hydrogen is not a break with the past. On the contrary, it is the ultimate stage of the decarbonisation trend that has accompanied the evolution of energy sources for mankind over the centuries (*figure 1.6*). With time, there have been an evolution from solid to liquid to gaseous fuel (wood, coal, petroleum, propane, methane). The fuel molecules have become smaller, leaner in carbon, and richer in hydrogen. The last major move was to methane, which

is a much cleaner burn than gasoline. The future step is expected to be hydrogen, which has the potential to solve both the environmental and energetic problems faced by humankinds [22].

H_2 can be burned to run an internal combustion engine or recombined with oxygen in a fuel cell to run electric motors. Cars, trains, ships, airplanes and rockets can already run on hydrogen, in various forms. NASA used hydrogen to launch Space Shuttles into space [23] Many companies are working to develop technologies that might efficiently exploit the potential of hydrogen energy for use in motor vehicles. However, before wide-scale use of hydrogen fuel can be accomplished, key technological challenges need to be resolved. In particular, clean and cost-effective production and storage of hydrogen are the two main obstacles to the hydrogen economy.

Hydrogen storage

The storage problem of hydrogen is related to its very low energy content by volume. Therefore, hydrogen must be made more energy dense to be useful for transportation. Most research into hydrogen storage is focused on storing hydrogen in a safe, reliable, compact and cost-effective way. Currently, hydrogen can be stored in three different ways [24]:

- as compressed gas in high pressure tanks (up to 700 bar); this method is beneficial for fuel purposes, because in this form it can be stored in a smaller space while retaining its energy effectiveness.
- as liquid in cryogenic tanks (T = 20 K, at pressures of 6-350 bar). This method is gravimetrically and volumetrically more efficient than the previous one. However, more research is needed to overcome problems dealing with the uptake and release of hydrogen, high hydrogen liquefaction rate that causes large energy loss, hydrogen boil-off and tank cost.
- in materials able to absorb and release hydrogen under diverse conditions of pressure and temperature (metal hydrides, liquid organic hydrogen carriers, carbon materials, zeolites…).

Hydrogen production

Hydrogen is not a primary source of energy, because it is not found in its usable form on earth; rather it is an energy carrier much like electricity, because energy is required to extract it from substances like natural gas, water, coal, or any other hydrocarbon. At present, hydrogen is mainly produced from fossil fuels such as natural gas by steam reforming:

$$CH_4 + H_2O \longrightarrow CO + 3H_2$$

$$CO + H_2O \longrightarrow CO_2 + H_2$$

Other processes for making H_2 from fossil fuel sources include the water gas shift reactions. In all these processes, however, fossil fuels are consumed and CO_2 is emitted, in the same way as a car engine would do.

In recent years, driven by the growing concern about climate change, efforts have been made in developing new methods to generate H_2 from renewable and sustainable resources. There are different ways for solar hydrogen production [25]:

1. electrolysis of water using a solar cell, a hydroelectric power generation, etc…
2. reforming of biomass;
3. photocatalytic or photoelectrochemical water splitting (artificial photosynthesis).

Photoelectrochemical water splitting into hydrogen and oxygen using semiconductor catalysts is an effective method for converting solar energy or sunlight into clean and renewable hydrogen fuel.

1.4 References

1. Murphy, P., *Solar Update*, in *Solar Heating and Cooling Programme*. 2015, International Energy Agency: USA.
2. Lewis, N.S. and D.G. Nocera, *Powering the planet: Chemical challenges in solar energy utilization.* Proceedings of the National Academy of Sciences, 2006. **103**(43): p. 15729-15735.
3. *World Energy Assessment Report: Energy and the Challenge of Sustainability*, in *United Nations Development Program*. 2003: United Nations, New York.
4. Pachauri, R.K. and L.A. Meyer, *Climate Change 2014: Synthesis Report. Contribution of Working Groups I, II and III to the Fifth Assessment Report of the Intergovernmental Panel on Climate Change*. 2015, Geneva (Switzerland): IPCC. 151.
5. Hartmann, D.L., et al., *Observations: Atmosphere and Surface.*, in *Climate Change 2013: The Physical Science Basis*. 2013, Cambridge University Press: Cambridge (UK) and New York (USA).
6. Rhein, M., et al., *Observations: Ocean.*, in *Climate Change 2013: The Physical Science Basis*, S.G.U. Howard Freeland (Canada), Yukihiro Nojiri (Japan), Editor. 2013, Cambridge University Press: Cambridge (UK) and New York (USA).
7. Stocker, T.F., et al., *Climate Change 2013: The Physical Science Basis Summary for Policymakers*. 2013: Intergovernmental Panel on Climate Change.
8. Butler, J.H. and S.A. Montzka, *THE NOAA ANNUAL GREENHOUSE GAS INDEX (AGGI)*. 2015: Broadway.
9. Luthi, D., et al., *High-resolution carbon dioxide concentration record 650,000-800,000 years before present.* Nature, 2008. **453**(7193): p. 379-382.
10. *Advancing the Science of Climate Change*, N.R. Council, Editor. 2010, The National Academies Press: Washington, DC, USA.
11. Lazarus, M. and S. Kartha, *Linking Technology Development with Emissions Commitments: Exploring Metrics for Effort and Outcome*. 2009, Stockholm Environment Institute: USA.
12. *Report of the International Scientific Steering Committee*. in *International Symposium on the Stabilisation of greenhouse gas concentrations*. 2005. Hadley Centre, Met Office, Exeter, UK.

13. Rockstrom, J., et al., *A safe operating space for humanity.* Nature, 2009. **461**(7263): p. 472-475.
14. *Wikipedia: Paris Agreement*. [13-01-2016]; Available from: https://en.wikipedia.org/wiki/Paris_Agreement.
15. Murphy, P., *Solar Update*, in *Solar Heating and Cooling Programme*. 2009, International Energy Agency: USA.
16. Barber, J. and P.D. Tran, *From natural to artificial photosynthesis.* Journal of The Royal Society Interface, 2013. **10**(81).
17. Bolton, J.R., *Solar photoproduction of hydrogen: A review.* Solar Energy, 1996. **57**(1): p. 37-50.
18. Ciamician, G., *THE PHOTOCHEMISTRY OF THE FUTURE.* Science, 1912. **36**(926): p. 385-394.
19. Bard, A.J. and M.A. Fox, *Artificial Photosynthesis: Solar Splitting of Water to Hydrogen and Oxygen.* Accounts of Chemical Research, 1995. **28**(3): p. 141-145.
20. Carraro, M., et al., *Artificial photosynthesis challenges: water oxidation at nanostructured interfaces*, in *Photocatalysis*. 2011, Springer. p. 121-150.
21. Bockris, J.O.M., et al., *On the splitting of water.* International Journal of Hydrogen Energy, 1985. **10**(3): p. 179-201.
22. Rajeshwar, K., et al., *Solar Hydrogen Generation*. 2008. 1.
23. *Wikipedia: Hydrogen vehicle*. [28/11/2015]; Available from: https://en.wikipedia.org/wiki/Hydrogen_vehicle.
24. Niaz, S., T. Manzoor, and A.H. Pandith, *Hydrogen storage: Materials, methods and perspectives.* Renewable and Sustainable Energy Reviews, 2015. **50**: p. 457-469.
25. Kudo, A. and Y. Miseki, *Heterogeneous photocatalyst materials for water splitting.* Chemical Society Reviews, 2009. **38**(1): p. 253-278.

Chapter 2

Photo-electrochemical water splitting

Photocatalytic water splitting in a photo-electrochemical (PEC) cell was first demonstrated by Fujishima and Honda in 1972, using TiO_2 as the photo-catalyst [1]. A PEC cell utilizes light energy (photons) to perform a chemical reaction, in this case the splitting of water into hydrogen (H_2) and oxygen (O_2) gases. It consists of an anode and a cathode immersed in an electrolyte and connected by an external circuit. At least one of the two electrodes is a light absorbing semiconductor and the other electrode is typically a metal. If the photo-sensible electrode is the anode, we have a cell as the one schematized in *figure 2.1-A*. *Figure 2.1-B* shows a photo-electrochemical cell based on a photocathode. If both electrodes are made up of light absorbing materials, the cell is called tandem cell.

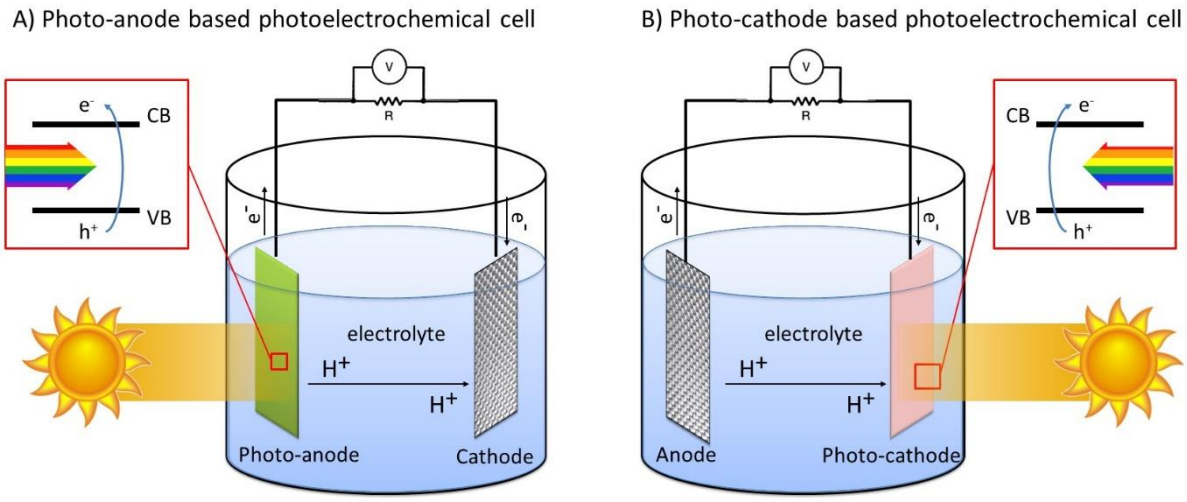

Figure 2.1: A) Illustration of a photo-electrochemical cell that consists of a semiconducting photo-anode and a metal cathode. B) Illustration of a photo-electrochemical cell that consists of a semiconducting photo-cathode and a metal anode.

When the photo-electrode is shined by photons with energy greater than its band gap, some electrons get enough energy to transfer from the valence band (VB) to the conduction band (CB) creating electron-hole pairs (*figure 2.1*). The photo-generated charges can either recombine or be split by the electric field in the space-charge region between the semiconductor and the electrolyte, undergoing an interfacial electron transfer process. The electric field reflects the band bending of the conduction and valence band edges at the semiconductor surface and is necessary to supply the free carriers to the appropriate electrode. At anode's surface the photo-generated holes split water molecules into oxygen and protons (oxygen evolution reaction):

$$2H_2O_{(liq)} + 4h^+ \rightarrow O_{2_{(gas)}} + 4H^+ \qquad \text{(low pH)}$$

Hydrogen ions migrate to the cathode through the electrolyte, while electrons are transferred to the cathode through the external circuit. At cathode's surface electrons reduce protons, generating gaseous hydrogen (hydrogen evolution reaction):

$$4H^+ + 4e^- \rightarrow 2H_{2_{(gas)}} \qquad \text{(low pH)}$$

In the case of alkaline electrolyte the two half reactions can be written as:

$$4OH^- + 4h^+ \rightarrow 2H_2O + O_{2_{(gas)}} \qquad \text{(high pH)}$$

$$4H_2O + 4e^- \rightarrow 2H_{2_{(gas)}} + 4OH^- \qquad \text{(high pH)}$$

The redox potentials for water oxidation and reduction are pH dependent:

$$E^0_{red} = 0.000\ V - 0.059\ V \cdot pH \qquad \text{(vs. NHE)}$$

$$E^0_{ox} = 1.229\ V\ - 0.059\ V \cdot pH \qquad \text{(vs. NHE)}$$

In any case, the overall water splitting reaction may be expressed as:

$$2h\nu + H_2O_{(liq)} \rightarrow \frac{1}{2}O_{2_{(gas)}} + H_{2_{(gas)}} \qquad \Delta E^0 = 1.229\ V$$

where ΔE^0 is the standard potential of the electrochemical cell and does not depend on the pH.

In a photo-electrochemical cell, hydrogen evolution and oxygen evolution reactions are spatially separated because they evolve at different electrodes. This is useful to limit the quick back reaction of oxygen and hydrogen to form water.

2.1 Photo-electrode requirements

For water splitting reaction to take place, several requirements must be met. The primary component of a photo-electrochemical cell is the photo-electrode where critical processes such as light harvesting, generation of electric charge carriers, minority carrier migration towards its interface with the electrolyte, as well as majority carrier transportation towards the external

circuit for water cleavage take place. The ability of the photo-electrode to carry out these processes largely determines the efficiency of the cell [2].

2.1.1 Band gap

Thermodynamically, water splitting into H_2 and O_2 is an uphill reaction, accompanied by a large positive change in the Gibbs free energy, given by:

$$\Delta G^0 = -nF\Delta E^0 = +237.2 \frac{kJ}{mol\ H_2}$$

where:

F is the Faraday's constant ($F = 96485\ C/mol$),

n indicates the number of transferred electrons ($n = 2$)

ΔE^0 is the standard potential of the electrochemical cell ($\Delta E^0 = 1.229\ V$).

A minimum energy of 1.229 eV per electron should be supplied by the photo-catalyst to split water. The basic parameter deciding the light harvesting ability of an absorber is its band gap, E_g, because only photons with energy greater than the band gap value are absorbed. The excess energy, which is the difference in the energy of the absorbed photon and the band gap energy ($E - E_g$), is lost as heat during the relaxation of the absorber to the level of E_g. Band gap value should be high enough to provide the minimum required energy to drive the reaction, but as small as possible to harvest a major portion of the solar spectrum. In order to quantify the optimal minimum band gap value, the inherent losses (E_{loss}) associated with solar energy conversion process have to be taken into account. These losses involve fundamental losses imposed by thermodynamics as well as losses due to the non-idealities in the conversion process (kinetic losses) [3]. The former loss is a consequence of the second law of thermodynamics. Indeed, band gap energy (E_g) corresponds to the internal energy change, which is related to the Gibbs energy change by the following equation:

$$\Delta G = \Delta U + P\Delta V - T\Delta S$$

where U, P, V, T and S represent the internal energy, pressure, volume, temperature and entropy, respectively. Photon absorption by the semiconductor leads to the creation of excited states in a sea of ground states and this increases the entropy of the ensemble. This entropy change due to the mixing of the excited states with the ground states, is denoted by ΔS_{mix}. The mixing of excited states with the ground states causes also a volume change (ΔV_{mix}), but this is null for an ideal chemical system ($\Delta V_{mix} = 0$). Consequently, in ideal conditions, band gap energy should be greater than the available work (Gibbs energy change per electron) by at least

$E_{loss} = T\Delta S_{mix}$, which takes a minimum value of 0.3-0.5 eV. In real cases, E_{loss} reaches a higher value (about 0.8 eV) because of the kinetic losses and the contributions due to non-idealities (overpotentials at the anode and at the cathode, resistive drop at the electrolyte, recombination of electron-hole pairs…). For this reason, to get maximum photon to chemical conversion efficiency, generally, a band gap of 2.0 – 2.25 eV is required for materials used as photoelectrodes in a PEC cell [2].

2.1.2 Band edges positions

Band edges positions are another thermodynamic requirement. Indeed, to drive the oxidation reaction, holes should be able to move from the photo-electrode to the solution. Consequently the top level of the valence band has to be more positive than the oxidation potential of O_2/H_2O. In the same way, reduction reaction occurs only if electrons can flow from the semiconductor to the solution, and this requires the bottom level of the conduction band to be more negative than the reduction potential of H^+/H_2 (see *figure 2.2*).

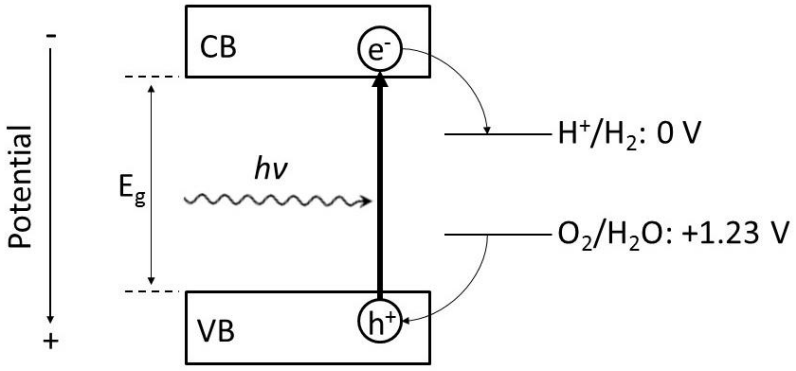

Figure 2.2: Required band edge positions for driving the overall water splitting reaction. CB: conduction band, VB: valence band, hν: incident photon, E_g: band gap value.

Moreover, each electrode requires an extra potential, called *overpotential*, to drive the reaction on its surface (kinetic requirement). Overpotentials are especially important for the placement of band edges: a valence band whose potential is not sufficiently positive for water oxidation, or a conduction band whose potential is not sufficiently negative for proton reduction, can lead to slow or negligible water splitting [4].

Figure 2.3 shows the band structures and the band gap values of some semiconductors. Some materials, such as TiO_2, are able to drive the overall water splitting reaction because their band edges straddle the potentials of water redox couple. However these materials have a wide band gap (E_g > 3.0 eV) and so are able to harvest only a small portion of the solar spectrum

(less than 4%). On the other hand, narrow band gap materials, such as Fe_2O_3, match well with the absorption of visible light, but their band edges configuration is not appropriate for driving both water oxidation and reduction reactions. Consequently, these materials can be used only in tandem cells to drive either water oxidation or water reduction reaction.

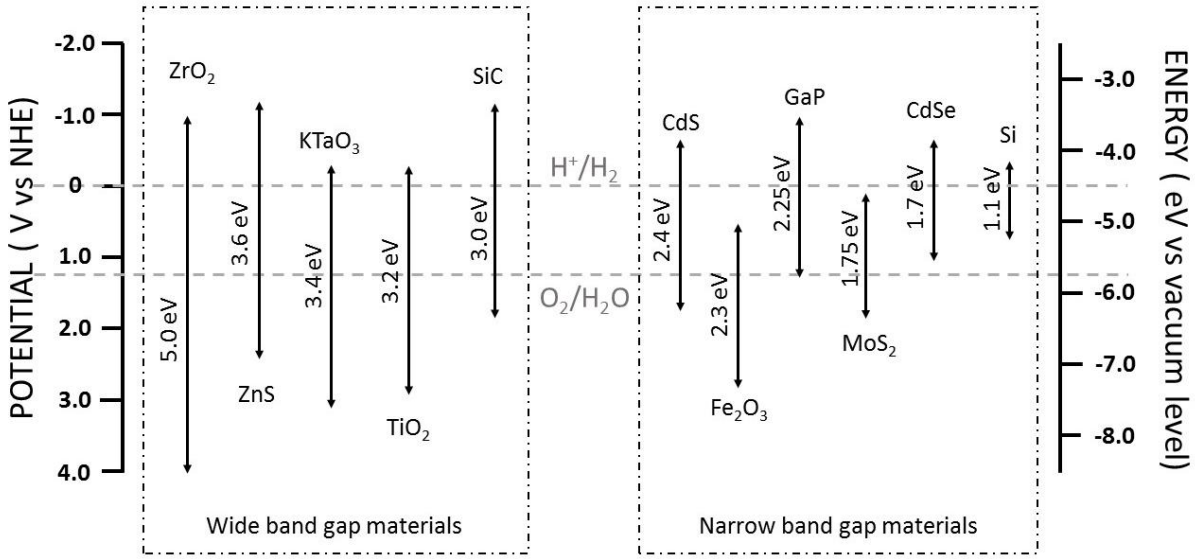

Figure 2.3: Band gap values (in eV) and band edge positions for selected semiconductors at pH 1. Grey dashed lines represent the redox potentials of water. The energy scale is indicated in electron volts using either the normal hydrogen electrode (NHE) or the vacuum level as a reference. Only few materials have a band structure suitable for driving the overall water splitting reaction [5].

2.1.3 Photo-voltage and charge carriers separation

When short circuited under dark conditions (no illumination), the Fermi levels of the semiconductor photo-electrode and counter electrode equalize with the redox potential of the electrolyte. As a result, valence band and conduction band are bent up to ($E_f - E_{redox}$), where E_f is the Fermi level of the semiconductor and E_{redox} is the potential of the redox couples in the solution. This band bending directs photogenerated free minority charge carriers (holes in the case of n-type and electrons for p-type semiconductors) to move into the solution (*figures 2.4 and 2.5*). For this reason n-type semiconductors are generally used as photo-anodes and p-type as photo-cathodes.

In principle, the maximum *internal energy* that can be extracted from photo-generated electron-hole pairs is given by the barrier height, called also flat band potential. However, for thermodynamic reasons, the *free energy* that can be actually obtained from the

semiconductor/liquid contact is smaller (due to entropy change) and depends on the kinetics of the charge carriers in the photo-stationary state that is produced when the interface is lit up. In the solid-state physics formalism, the free energy generated by the semiconductor is given by the difference between the hole and electron quasi-Fermi levels[1] under illumination, that is, by the free energy difference between the majority carriers and the photo-excited minority carriers (*figures 2.4 and 2.5*).

This difference is the photo-voltage and at zero current is termed the open-circuit voltage (V_{oc}). The magnitude of the photo-voltage that is generated by a semiconductor/liquid junction determines the photo-electrochemical reactions that can be driven by that system without an external bias. Even if the band-edges of the semiconductor straddle the water oxidation and reduction levels, water splitting is not possible unless the photo-voltage exceeds 1.229 V [4]. Commonly, open circuit voltage does not exceed 0.9 V, therefore, an external electrical or chemical bias is required to drive the water splitting reaction.

According to Lewis [6], the photo-voltage is affected by the kinetic processes that govern the respective electron and hole concentrations at the interface under quasi-equilibrium conditions, and can be broken down into five different categories. The photogenerated charge carriers can:

1. recombine in the bulk of the semiconductor,
2. recombine in the depletion region,
3. tunnel through the electric potential barrier near the surface,
4. thermally surmount the interfacial potential barrier (thermionic emission),
5. recombine at defects (trap states) at the semiconductor/liquid interface.

A key challenge in the development of water splitting devices is to fabricate semiconductor photo-electrodes for water oxidation and/or reduction that have bulk and surface properties (crystal structure, morphology, crystallinity, conductivity, surface area…) such that the generated photo-voltage reaches the fundamental bulk-recombination limit.

[1] The quasi-Fermi level is a description of the electrochemical potential of one carrier type at a time (i.e., either electrons or holes) under non-equilibrium (e.g., illuminated) conditions, using Fermi-Dirac statistics to describe separately the populations of electron and of holes. The prefix *quasi-* refers to the fact that thermalization of the excited carriers is a fast process, leaving the collection of holes (and electrons) each in quasi-thermal equilibrium under steady-state illumination. True equilibrium can be reached only in the dark, through slower conduction-band to valence-band recombination processes, at which point a single Fermi level describes the statistical distribution of all carriers.

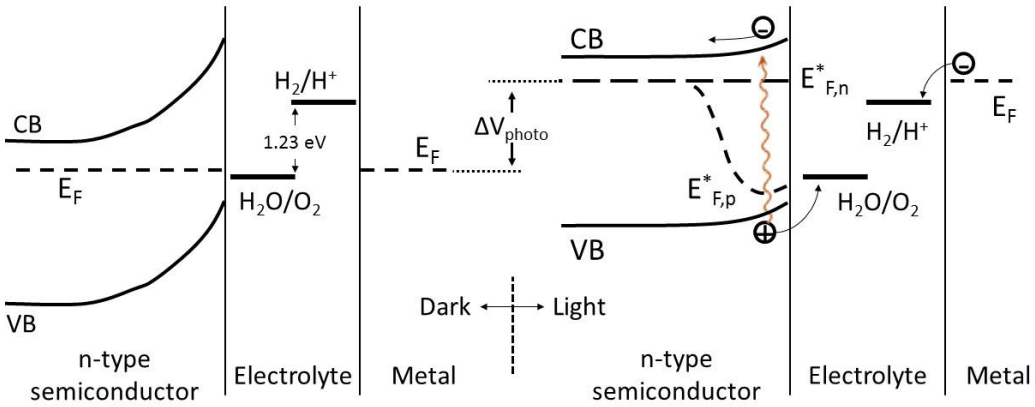

Figure 2.4: Band diagram for a PEC cell based on an n-type semiconducting photo-anode that is electrically connected to a metal counter electrode; in equilibrium in the dark (left) and under illumination (right). Illumination raises the Fermi level and decreases the band bending. Near the semiconductor/electrolyte interface, the Fermi level splits into quasi-Fermi levels for the electrons and holes.

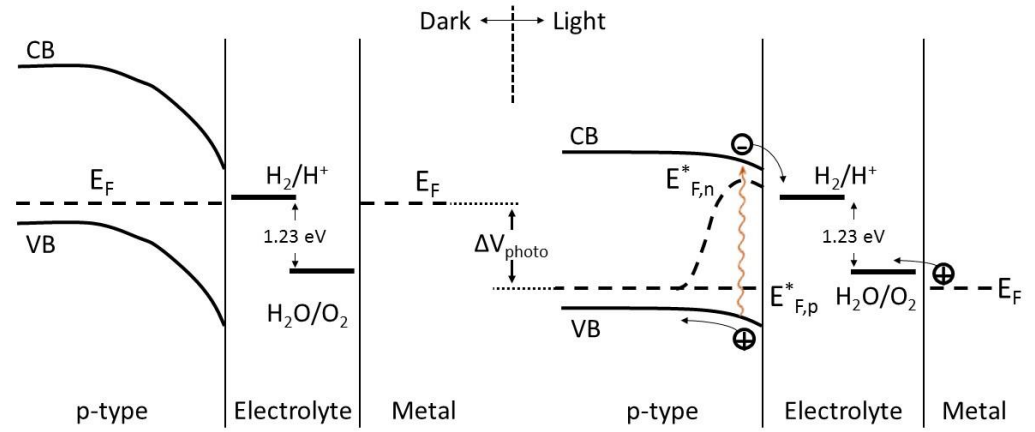

Figure 2.5: Band diagram for a PEC cell based on a p-type semiconducting photo-cathode that is electrically connected to a metal counter electrode; in equilibrium in the dark (left) and under illumination (right). Illumination lowers the Fermi level and decreases the band bending. Near the semiconductor/electrolyte interface, the Fermi level splits into quasi-Fermi levels for the electrons and holes.

2.1.4 Stability in aqueous media

CdS, see *figure 2.3*, has an appropriate band gap value (2.4 eV) and band edge positions suitable for driving the overall water splitting reaction. However, it is not studied for this application, because it is not stable. Indeed, under oxidizing conditions, S^{2-} in CdS rather than

H_2O is oxidized by photo-generated holes accompanied with elution of Cd^{2+} according to the following equation [7]:

$$CdS + 2h^+ \rightarrow Cd^{2+} + S$$

As a consequence, the electrode degrades during operation, compromising cell performance.

Therefore, semiconductor photo-electrodes must exhibit excellent oxidative/reductive stability in contact with aqueous electrolyte solution. For thermodynamic stability, semiconductor's reductive and oxidative decomposition potentials must be more negative than the semiconductor's conduction band-edge for water reduction or more positive than the semiconductor valence band-edge potential for water oxidation, respectively. Very few semiconductor materials exhibit the necessary requirements for electrode stability in aqueous electrolyte solutions simultaneously for both water oxidation and reduction [4]. Due to the requirement of stability under oxidizing conditions, most of the photoanode materials that have been investigated are metal oxides or metal oxide anions (oxometalates), in pure, mixed, or doped forms.

2.2 PEC cell efficiency

If the photoelectrode fulfils all the thermodynamic and kinetic requirements mentioned above, water splitting reaction takes place. In this case, the performance of different PEC cells can be compared by looking at their solar to hydrogen conversion efficiency (η_{STH}) defined as [8]:

$$\eta_{STH} = \frac{j_{photo}(V_{redox} - V_{bias})}{P_{light}}$$

where:

j_{photo} is the photocurrent density [mA/cm^2],

V_{redox} is the redox potential for water splitting (1.23 V at room temperature),

V_{bias} is the external bias,

P_{light} is the incident light power density [mW/cm^2].

This definition assumes that all the photogenerated electrons and holes are used for driving the water splitting reaction.

This equation gives the solar to hydrogen conversion efficiency of the entire PEC cell including all of its components: working and counter electrodes, electrolyte, wires, and so forth. Each and every one of them contributes to the overall loss because of recombination, polarization, diffusion, internal resistance, overpotential, or other losses. The cell efficiency, as defined here, accounts for all these losses together. Therefore solar-to-hydrogen conversion efficiency is an important benchmarking parameter of a photoelectrochemical cell. However, researchers are generally interested in optimizing a specific component of the cell instead of constructing a complete PEC cell. In these cases, solar to hydrogen efficiency is not very useful because it does not allow to decouple the contributions of the different components of the cell. For example, we study the properties of the photoelectrodes and try to relate their structural, morphological, optical and electrical properties to the electrocatalytic activity, both in dark and light conditions. To do this, we use a standard cell, in two- or three-electrode configuration, where the counter electrode is a platinum mesh and the materials we want to study are used as photoelectrodes. Instead of calculating the solar to hydrogen conversion efficiency of these cells, we report the photoelectrochemical performance of the photoelectrode both in dark and light conditions. In this way, it is possible to relate the modification made to the material (doping, nanostructuring) to the changes in (photo)-electrochemical performance.

Solar hydrogen will become economically competitive with fossil fuels at solar to hydrogen conversion efficiencies of 15% and beyond [9]. The highest solar to hydrogen conversion efficiency measured so far for an unassisted PEC cell system is 14% and was achieved by May and coworkers [9] using a tandem structure absorber (a GaInP n–p top cell and a GaInAs n–i–p bottom cell) coupled with Rh electrocatalyst for hydrogen evolution and RuO_2 catalyst for oxygen evolution. An open problem of this system is long term stability. At the beginning, the samples only survived a few seconds before their power output collapsed. After about one year of optimization the stability was raised up to 40 hours, which is still not enough for application purpose. Moreover, this system could never be scaled up to the terrestrial level because it involves mainly rare materials, as we will see in the next section.

2.3 Scalable and eco-friendly materials

In addition to fulfil the aforementioned requirements for high efficiency and long-term stability, the materials employed for solar hydrogen production have to be earth abundant, cheap and environment friendly. Actually, for renewable and sustainable energy conversion technologies to play a relevant role at the terrestrial scale, they must be able to scale to the

terawatt level of deployment. Oftentimes, the scalability of a material is related only to its average crustal abundance, however, according to Vesborg et al. [10], this can be potentially misleading. Indeed, the accessibility of the material and the facility of its mining and production are important as well. There are elements with high average crustal concentration, but without the tendency to concentrate into ores with sufficiently high concentration to allow economical mining. Conversely, there are elements that can be mined economically despite very low average crustal abundance because they have a tendency to form ore bodies with a concentration much higher than the average crustal average. From this point of view, an ore body where a given element is highly concentrated with respect to its average crustal concentration represents an exergy resource because the entropic work of concentration has been done by nature. Treating concentrated resource ores as available exergy is a powerful concept that allows comparison between ores of different elements and even fossil fuels (also an exergy resource) on an equal footing.

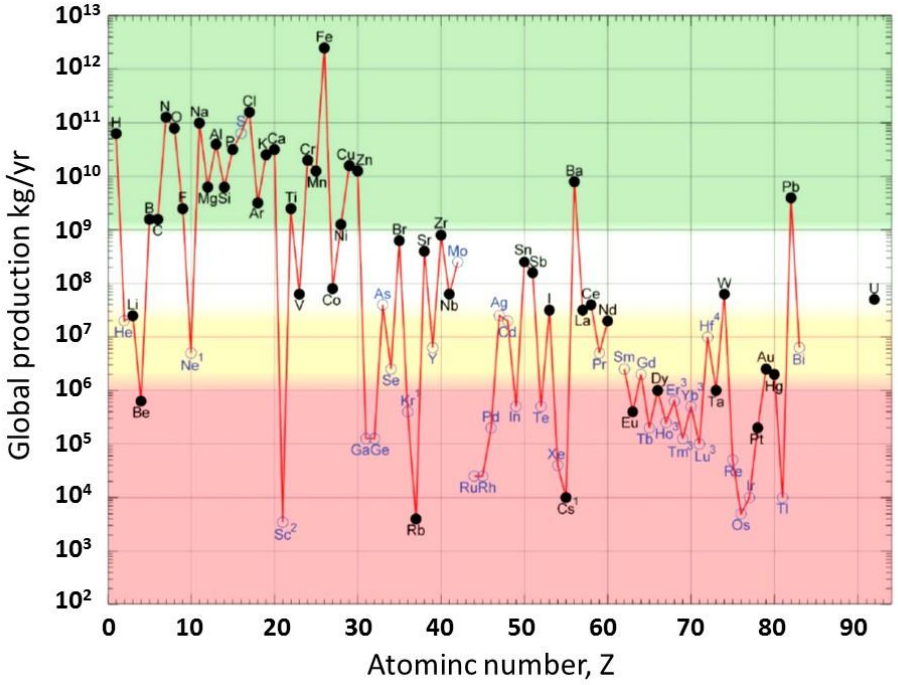

Figure 2.6: Global primary production of the elements in 2010. Solid symbols and black font are used for elements which are main economic products of their respective ores while open symbols and blue font are used for the elements which are mostly by-products of other elements [10].

Vesborg and Jaramillo [10] compared the availability of almost all the elements of the periodic table by taking into account two main parameters:

1. The nature of production that is important to distinguish between elements which are mostly the primary economic product of their extraction (main products) and those

which are mostly by-products of other elements. Indeed, the supply of by-products tends to be very inelastic to increases in demand (and price) once the available material in the tailing stream of the primary product are exhausted. Conversely, the supply of main products follows demand with very small changes in price.

2. Current global production rate, which represents the confirmed here-and-now availability of every element.

Figure 2.6 shows the logarithmic plot of estimated global annual production of each element in 2010 as a function of its atomic number. The data markers of by-products are open circles coloured blue and those for main products are black coloured dots. Elements are classified into four groups: high volume (green), low-medium volume (light green), very low volume (yellow) and extremely low volume level (red). Only the material with high and low-medium amount of annual production should be considered as constituents of water splitting devices. Indeed, through an order-of-magnitude analysis it can be shown that to produce one terawatt average (TW_{avg}) of renewable power requires enormous amounts of materials. For example for thin-film photovoltaics or photoelectrodes for solar water splitting they estimated 350 kt of absorber material for each TW_{avg}. Therefore the absorber must be made from one of the top-30 elements.

To understand better the importance of these technological constraints, we can take as a case study the cell used by May [9] to achieve the record efficiency value. Most of the materials used in that cell belong to the red group: elements with extremely low annual global production. Arban [11], performed a raw calculation to estimate the average amount of each element present in the cell necessary to generate 1 TW of electricity. Taking as reference the global annual production values reported by Vesborg [10], it comes out that it would be necessary more than 6000 years to produce the required In and more than 15000 years for Ga. So, even if the long term stability problem were solved, this cell could never be scaled up to the terawatt level.

A last requirement is the use of bio-compatible material. Only it this way the produced hydrogen can be properly considered an environment friendly fuel. Four are the main requirements for materials being employed as photo-electrodes for photoelectrochemical water splitting: efficiency, long-term stability, biocompatibility and scalability. Since there is no material occurring in nature that satisfies all of them together, huge efforts are being invested in research for the development of photoelectrodes with suitable properties. The starting point should be environment friendly and scalable materials. In this thesis two different materials were studied: TiO_2 and Fe_2O_3.

2.4 Titanium dioxide (TiO_2)

Titanium dioxide, also known as titanium (IV) oxide or titania, is the naturally occurring oxide of titanium, chemical formula TiO_2. It is a widespread, cheap and bio-compatible material. Because of its brightness and very high refractive index, titanium dioxide is the most widely used white pigment in paints, food colouring, cosmetics, toothpastes, polymers, and other instances in which white colouration is desired [12]. Since the famous and pioneering work of Fujishima and Honda on the possibility of using TiO_2 based photoanode for solar water splitting into hydrogen and oxygen [1], many photo-chemical applications of this oxide have been realized primarily due to the advantageous combination of its scalability, non-toxicity and excellent stability against photo-corrosion. Titania photo-catalyst is applied in a range of important technological areas [13]:

- Environment: air purification and water treatment;
- Built environment: self-cleaning coatings and non-spotting glass;
- Biomedicine: self-sterilising coatings;
- Energy: solar water splitting for hydrogen generation and dye-sensitised solar cells.

Titanium dioxide is mined as a main product from two different ores: 91% from ilmenite ($FeTiO_3$), the most widespread form of titanium dioxide-bearing ore around the world, and 9% from Rutile (TiO_2), which contains around 98% titanium dioxide in the ore. The global production of TiO_2 exceeds 1 Mt/yr which means that up-to-date availability is enough for application in energy related technology [10].

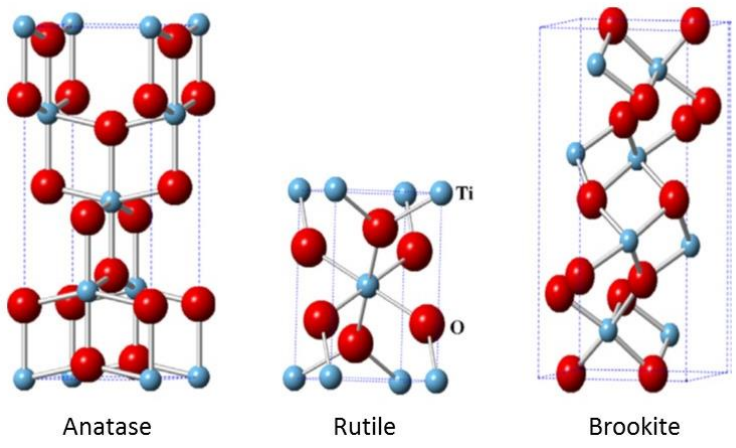

Figure 2.7: Crystal structure of Anatase, Rutile and Brookite (Source [14]).

Titanium dioxide occurs in nature in three main polymorphs Rutile (tetragonal), Anatase (tetragonal) and Brookite (orthorhombic), whose crystal structures are reported in *figure 2.7*.

The most common form is rutile, which is also the equilibrium phase at all temperatures; the metastable anatase and brookite phases convert irreversibly to rutile upon thermal treatment. Other five high pressure phases of TiO_2 have been reported:

- TiO_2 II or srilankite, an orthorhombic polymorph of the lead oxide structure;
- Cubic fluorite-type polymorph;
- Pyrite-type polymorph;
- Monoclinic baddeleyite-type polymorph;
- Cotunnite-type polymorph.

However, only Rutile and Anatase phases are important for TiO_2 applications. Both polymorphs have tetragonal crystal structure, but Rutile contains six atoms per unit cell whereas Anatase twelve. In both these structures, the basic building block consists of a titanium atom surrounded by six oxygen atoms in a more or less distorted octahedral configuration (*figure 2.7*). The stacking of the octahedral results in threefold coordinated oxygen atoms.

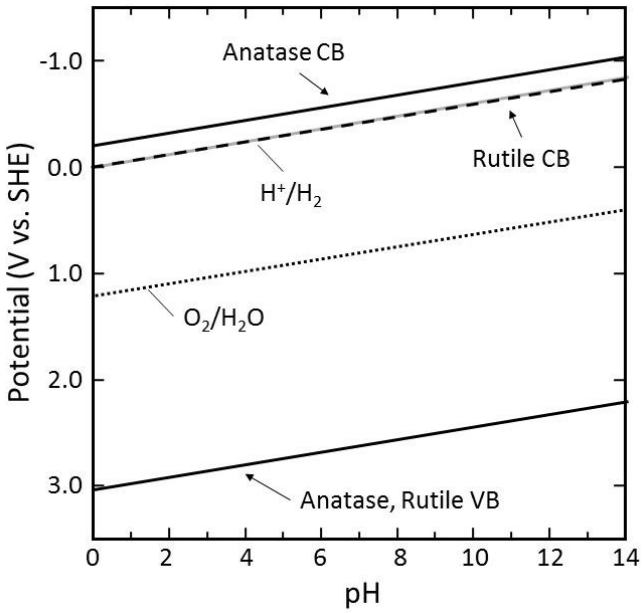

Figure 2.8: Energy bands on TiO_2 as a function of pH. Note that the rutile CB (black dashed) line is superimposed on the reversible hydrogen potential H^+/H_2 (grey line) at all pH (source [15]).

The band edges of TiO_2 are well matched with the redox level of water, meaning that it could drive the overall water splitting reaction (*figure 2.8*). The valence-band energies for both rutile and Anatase lie at approximately the same potential, which is more than sufficiently positive to oxidize water, by approximately 1.8 V, at all pH values. The conduction band energy of Rutile is essentially coincident with the reversible hydrogen potential at all pH values, whereas that for Anatase is more negative by 0.20V [15]. For this reason, reduction reaction occurs more

easily on Anatase than on rutile. However, the wide band gap of TiO_2 (3.0 eV for rutile and 3.2 eV for Anatase) hinders the efficiency of solar light absorption. Pure TiO_2 is able to absorb only the UV portion of the solar spectrum, which is only about 4%. Despite the larger experimental band gap of Anatase (3.2 eV), compared with rutile (3.0 eV), the photocatalytic performance of Anatase is widely reported to be superior to that of rutile. This is attributed to a higher density of localised states and consequent surface-adsorbed hydroxyl radicals and slower charge carrier recombination in Anatase relative to rutile [13]. Titanium dioxide usually exists as an n-type semiconductor due to the presence of oxygen vacancies [16], therefore it is applied as photoanode material.

In addition to the wide band gap, the second main drawback of TiO_2 is the fast recombination of charge carriers (~ 1 μs). The photo-excited electrons return to the valence band radiatively or non-radiatively during the recombination processes. These events can occur either in the bulk or on the surface and are normally induced by defects, impurities and other crystal bulk/surface imperfections. For example, the photocatalytic activity of amorphous TiO_2 is reported to be negligible compared to that of crystalline TiO_2, because the crystalline structure minimizes the photo excited electron hole recombination [14].

Advantages	Disadvantages
• High photo-chemical stability. • Bio-compatible and nontoxic material. • High stability against photo-corrosion. • Abundant and cheap (scalable). • Band edges straddling water redox potentials.	• Wide band gap (3.2 eV) limits solar light harvesting. • Rapid recombination of photo-generated charge carriers (~ 1 μs).

Table 2.1: The advantages and disadvantages of TiO_2 as photo-catalyst for water splitting process.

Table 2.1 summarizes the advantages and disadvantages of TiO_2. Various strategies including crystal phase tailoring and textural modification, electronic structure engineering, heterojunction formation, surface sensitization and doping with ions have been developed in an attempt to modify the photocatalytic process involving light harvesting and excitation, as well as bulk diffusion, surface trapping and interfacial transfer of photo-produced electrons and holes in TiO_2.

2.5 Iron oxide (Fe_2O_3)

Iron oxides are common compounds, which are widespread in nature. They are present in almost all earth systems: atmosphere, pedosphere, biosphere and lithosphere. Moreover, iron oxides are nontoxic and environment friendly. As a consequence, iron oxides are presently used in many industrial processes and are studied for application in many research fields. Among iron oxides, hematite (α-Fe_2O_3) is the most stable phase. It is also the most abundant mineral on Earth and constitutes the primary ore of iron. Thus, from the scalability point of view, hematite is the top material for energy-related technologies applications.

The first studies on photo-electrochemical water oxidation with Fe_2O_3 date back to experiments by Allen Bard in 1976 [17], Karl Frese in 1978 [18], and Andrew Hamnett in 1983 [19]. Hematite (α-Fe_2O_3) is a very promising material for photo-electrochemical water splitting due to its widespread availability, extraordinary chemical stability in oxidative environment and sufficiently broad visible light absorption [18]. It is an n-type semiconductor with a band gap of 2.1 eV, which allows the absorption of a large portion of the terrestrial solar spectrum. Unlike TiO_2, hematite in not able to drive the overall water splitting reaction because its conduction band edge is more positive (~0.2 eV) than the water reduction potential. Nevertheless, since its valence band edge is substantially lower than the water oxidation potential, hematite is a promising photo-anode material and can be employed in a tandem cell configuration for unassisted solar hydrogen production.

However, hematite has not yet reached its theoretical potential in terms of photovoltage or photocurrent, because of a combination of shortcomings (*table 2.2*). First of all, it suffers from long penetration depth of visible light ($\alpha^{-1} = 118$ nm at $\lambda = 550$ nm) due to its indirect band gap transition [20, 21]. As a consequence, the majority of photo-generated carriers are produced very far (~100 nm) from the semiconductor/liquid interface. On the other hand, the very short excited-state lifetime (~10^{-12} s) [22], along with the poor minority charge carrier mobility (0.2 $cm^2\,V^{-1}\,s^{-1}$), leads to a hole diffusion length of only 2 – 4 nm [23]. Therefore, most of the photo-generated charge carriers recombine before reaching material's surface. The trade-off between optical absorption and collection of charge carriers constitutes a big limit to the efficiency of hematite photoanodes. Moreover, it is well established that the performance of crystalline hematite is limited by slow water oxidation kinetics [17, 19]. In contrast to TiO_2, the water oxidation rate on Fe_2O_3 is also found to depend on temperature [24].

Advantages	Disadvantages
• Bio-compatible and nontoxic material • Abundant and cheap (scalable). • Band edges configuration suitable for water oxidation reaction. • Good band gap value.	• Long penetration depth of visible light ($\alpha^{-1} = 118$ nm at $\lambda = 550$ nm). • Very short hole diffusion length (2 – 4 nm). • Slow water oxidation kinetics of crystalline hematite.

Table 2.2: The advantages and disadvantages of Fe_2O_3 as photo-catalyst for water splitting process.

Considerable effort has been devoted to improving the actual efficiency of hematite-based photoanodes. A variety of rational modification strategies are suggested in literature, including nanostructuring, doping and band structures engineering. Nanostructuring improves hole transport to the surface, because it increases the surface area and decouples light absorption and charge collection processes. Indeed, in a nanostructured film, the distance travelled by the charge carriers to reach the semiconductor/electrolyte interface is no more related to film thickness. This allows improving the charge collection efficiency without reducing film thickness, i.e. without hindering the light absorption efficiency. On the other hand, metal ion doping is used to enhance the transport of electrons, which need to travel to the back-contacts of hematite film. Moreover, coupling hematite to another semiconductor with appropriate band structure has been considered to be effective for improving the photogenerated charge separation by means of intercomponent charge transfer. Finally, the slow kinetics of hole transfer to the solution can be improved by modifying hematite surface with specific cocatalysts (e.g. oxygen evolution catalysts, OEC) to facilitate the four-electron process of water oxidation, which generally catalyses hole transfer and results in suppressed surface charge recombination (see chapters 7 and 8).

2.6 References

1. Fujishima, A. and K. Honda, *Electrochemical photolysis of water at a semiconductor electrode.* Nature, 1972. **238**(5358): p. 37-8.
2. Varghese, O.K. and C.A. Grimes, *Appropriate strategies for determining the photoconversion efficiency of water photoelectrolysis cells: A review with examples using titania nanotube array photoanodes.* Solar Energy Materials and Solar Cells, 2008. **92**(4): p. 374-384.
3. Bolton, J.R. and D.O. Hall, *Photochemical conversion and storage of solar energy*. Annual Review of Energy, 1979. **4**(1): p. 353-401.
4. Walter, M.G., et al., *Solar water splitting cells.* Chemical reviews, 2010. **110**(11): p. 6446-6473.
5. Luca Chiarello, G. and E. Selli, *Photocatalytic hydrogen production.* Recent Patents on Engineering, 2010. **4**(3): p. 155-169.
6. Lewis, N.S., *Mechanistic studies of light-induced charge separation at semiconductor/liquid interfaces.* Accounts of Chemical Research, 1990. **23**(6): p. 176-183.
7. Pleskov, Y.V. and Y.Y. Gurevich, *Semiconductor photoelectrochemistry.* 1986.
8. Van De Krol, R. and M. Grätzel, *Photoelectrochemical Hydrogen Production*. 2012. 75.
9. May, M.M., et al., *Efficient direct solar-to-hydrogen conversion by in situ interface transformation of a tandem structure.* Nat Commun, 2015. **6**.
10. Vesborg, P.C. and T.F. Jaramillo, *Addressing the terawatt challenge: scalability in the supply of chemical elements for renewable energy.* RSC Advances, 2012. **2**(21): p. 7933-7947.
11. Giacomo, A., *On the effect of Sn-doping in hematite anodes: a systematic investigation.*, in *Department of Physics*. 2015, University of Trento: Trento.
12. Fisher, J. and T.A. Egerton, *Titanium compounds, inorganic.* Kirk-Othmer Encyclopedia of Chemical Technology, 2001.
13. Hanaor, D.A.H. and C.C. Sorrell, *Review of the anatase to rutile phase transformation.* Journal of Materials Science, 2011. **46**(4): p. 855-874.
14. Etacheri, V., et al., *Visible-light activation of TiO_2 photocatalysts: Advances in theory and experiments.* Journal of Photochemistry and Photobiology C: Photochemistry Reviews, 2015. **25**: p. 1-29.

15. Fujishima, A., X. Zhang, and D.A. Tryk, *TiO_2 photocatalysis and related surface phenomena.* Surface Science Reports, 2008. **63**(12): p. 515-582.
16. Beranek, R., *(Photo) electrochemical Methods for the Determination of the Band Edge Positions of TiO_2-Based Nanomaterials.* Advances in Physical Chemistry, 2012. **2011**.
17. Hardee, K.L. and A.J. Bard, *Semiconductor electrodes V. The application of chemically vapor deposited iron oxide films to photosensitized electrolysis.* Journal of the Electrochemical Society, 1976. **123**(7): p. 1024-1026.
18. Kennedy, J.H. and K.W. Frese, *Photooxidation of Water at α-Fe_2O_3 Electrodes.* Journal of the Electrochemical Society, 1978. **125**(5): p. 709-714.
19. Dare-Edwards, M.P., et al., *Electrochemistry and photoelectrochemistry of iron (III) oxide.* Journal of the Chemical Society, Faraday Transactions 1: Physical Chemistry in Condensed Phases, 1983. **79**(9): p. 2027-2041.
20. Bolton, J.R., S.J. Strickler, and J.S. Connolly, *Limiting and realizable efficiencies of solar photolysis of water.* Nature, 1985. **316**: p. 495.
21. Cesar, I., et al., *Influence of feature size, film thickness, and silicon doping on the performance of nanostructured hematite photoanodes for solar water splitting.* The Journal of Physical Chemistry C, 2008. **113**(2): p. 772-782.
22. Khaselev, O. and J.A. Turner, *A monolithic photovoltaic-photoelectrochemical device for hydrogen production via water splitting.* Science, 1998. **280**(5362): p. 425-427.
23. Sivula, K., et al., *Photoelectrochemical water splitting with mesoporous hematite prepared by a solution-based colloidal approach.* Journal of the American Chemical Society, 2010. **132**(21): p. 7436-7444.
24. Cowan, A.J., et al., *Activation energies for the rate-limiting step in water photooxidation by nanostructured α-Fe_2O_3 and TiO_2.* Journal of the American Chemical Society, 2011. **133**(26): p. 10134-10140.

Chapter 3

Multilayer films of Indium Tin Oxide/TiO_2 codoped with Vanadium and Nitrogen for efficient photocatalytic water splitting[1]

Wide band gap and fast recombination of charge carriers are the two main drawbacks of TiO_2 photocatalyst. In this chapter we study the combination of two strategies to enhance the visible light absorption of TiO_2 and limit the recombination of charge carriers. The first strategy consists of codoping TiO_2 with a cation (V) and an anion (N), which cause an effective narrowing of the band gap by creating isolated energy levels near the conduction and valence bands, respectively. The second strategy involves the use of indium tin oxide/V-N-codoped TiO_2 multilayer structure to limit the recombination of charge carriers by taking advantage of the space charge layer generated at the interface between the two materials. The synergistic effects created by band narrowing and enhanced charge separation generate higher photocurrent for water splitting under visible light, which definitely exceeds that obtained by pure TiO_2.

3.1 Introduction

Doping with foreign atoms or ions is one of the most promising strategies to modify the optical and photo-catalytic properties of TiO_2 [1, 2]. Indeed, the incorporation of dopant species in TiO_2 may affect the electronic band edges or introduce impurity states in the band gap, thus allowing visible light absorption. For example, transition metal cations such as V, Cr, Mo, and

[1] This chapter is based on the results published in: Z. El Koura, N. Patel, R. Edla, A. Miotello; *Int. J. Nanotechnol.*, Vol. 11 Nos. 9/10/11 (2014) 1017-1027

Fe are reported to create energy levels below the conduction band edge [3-8]. Instead, non-metal anions such as N, S, F and C generate energy levels above the valence band edge [9-12]. Moreover, doping affects also the mobility and the recombination rate of charge carriers [2, 5], because the impurity levels act as trapping sites for electrons and holes. In particular, at low concentration, dopant species improve the separation of charge carriers, whereas at high concentration they act as recombination centres. In the case of TiO_2 mono-doped with a cation or an anion, an effective extension of the spectral response is obtained only after doping at high concentration. The concomitant increase of charge carriers recombination in these conditions, explains why TiO_2 mono-doping has never resulted in a satisfactory photocatalytic activity under visible light irradiation.

In the last years, many studies focused on TiO_2 codoped with a transition metal and a non-metal ion as a new promising second-generation photocatalyst. The idea is that the presence of both dopant types should improve the visible light absorption also at low concentrations, because of the simultaneous presence of impurity energy levels below the conduction band and above the valence band. Moreover, it has been reported that the cooperation of the two dopants in passivated donor-acceptor codoping also promotes the separation of charge carriers [13]. In a recent review paper, Zhang et al. [14] showed that N-TiO_2 modified with metal ions, or metal oxides, or non-metals, usually exhibits more favorable visible-light absorption and photocatalytic activity as compared to N-doped TiO_2. Cong and coworkers [15] studied Fe and N codoped TiO_2 photocatalysts, which exhibited enhanced visible-light photocatalytic activity for rhodamine B photodegradation as compared to pure TiO_2. In this work we study the properties of V and N codoped TiO_2. Indeed, though V-doped TiO_2 and N-doped TiO_2 have already shown an enhanced visible photocatalytic activities, few reports have been published on V and N codoped TiO_2 photocatalysts and among these, as for our knowledge, no one on RF magnetron sputtered films.

The recombination of charge carriers can be further limited by separating the photoelectrons and holes as soon as they are generated. This fast separation can be achieved by coupling TiO_2 with a semiconductor with appropriate bands configuration. For instance, coupling TiO_2 with indium tin oxide (ITO) favors the injection of photo-electrons from the former to the latter, because the conduction band edge of ITO is at a lower energy value (~ -4.5 eV) than that of TiO_2 (~ -4.0 eV). Moreover, the high conductivity of ITO ensures a good electrical contact with the cathode. The beneficial effect of ITO/TiO_2 interface on the

photocatalytic activity was demonstrated by Dholam et al., who also used the multilayer strategy to fully exploit the effect of the interface [4, 7].

In the present work, indium tin oxide (ITO)/V-N-codoped TiO_2 multilayer thin films were synthesized by RF-magnetron sputtering. The enhanced photocurrent of V-N-codoped TiO_2 is discussed in terms of synergetic effects produced by enhanced visible light absorption and better charge separation.

3.2 Experimental

RF-magnetron reactive sputtering was used to synthesize pure, N-doped, V-doped, and V-N-codoped TiO_2 thin films. Pure TiO_2 disc (purity 99.99%), and ITO target (purity 99.99%) were used as sputtering targets while Ar (purity 99.99%) as working gas. Before deposition, a base pressure of $<2x10^{-7}$ mbar was attained and contaminations on the target surfaces were removed by pre-sputtering for 20 min. The sample-target distance was kept constant at 5.5 cm and the working gas pressure was maintained at $8x10^{-3}$ mbar throughout the deposition. V-doped TiO_2 films were synthesized by partially covering the TiO_2 target surface with small vanadium metal pieces (purity 99.9%) while N-doping was achieved by introducing nitrogen in the deposition chamber with flow rate of 30 sccm. Both these strategies were used together to synthesize V-N-codoped TiO_2 on glass and Si (100) substrates. In all samples, an ITO layer, of about 50 nm, was deposited at the beginning on the substrate with RF power of 100 W before the deposition of the pure or doped TiO_2 film (RF power = 150 W) to form single ITO/TiO_2 bilayer. Multilayer films, formed by more than one bilayer (3-, 4-, 5-, and 6-bilayers), were deposited in order to study the efficiency of the multilayer structure in reducing recombination rate of holes and electrons. The thickness of each ITO layer was kept constant independently from the number of bilayers whereas the thickness of V-N-codoped TiO_2 was decreased as the number of bilayers increased. In this way the total amount of codoped TiO_2 (about 750 nm) was kept constant in all the samples allowing the comparison between the results obtained with different structures. The surface of all the films that will be in contact with the electrolyte was always covered with pure TiO_2 of ~ 200 nm to protect the metal ions from leaching out in the electrolyte.

Surface morphology and cross section of the TiO_2 samples were characterized by using Scanning Electron Microscopy (SEM-FEG, JSM-7001F, JEOL). Energy-Dispersive X-ray Spectroscopy analysis (EDXS, INCA PentaFET-x3) was used to determine the composition of

the samples. The structural characterization of the V-N-codoped TiO_2 films was carried out on the glass slides by micro-Raman spectroscopy using HORIBA JobinYvon Lab RAM Aramis Raman spectrometer with diode pumped solid state laser at 634 nm. X-ray Photoelectron Spectroscopy (XPS) was performed to establish the surface electronic states of the photocatalysts and the concentration of N. XPS spectra were acquired by using a KratosAXISUltra^{DLD} instrument equipped with a monochromatic Al K_α (1486.7 eV) X-ray source (acceleration voltage: 15.1 kV, emission current: 10 mA) and a hemispherical sector analyzer. No charge neutralization system was required during the measurements, but an ex-post charge correction was carried out to perform the complete data analysis. Optical measurements in the UV and visible range were performed using a VARIAN Cary 5000 UV-Vis-NIR spectrophotometer. The wavelength range between 250 nm and 750 nm was used to obtain the absorbance spectra of samples deposited on glass slides.

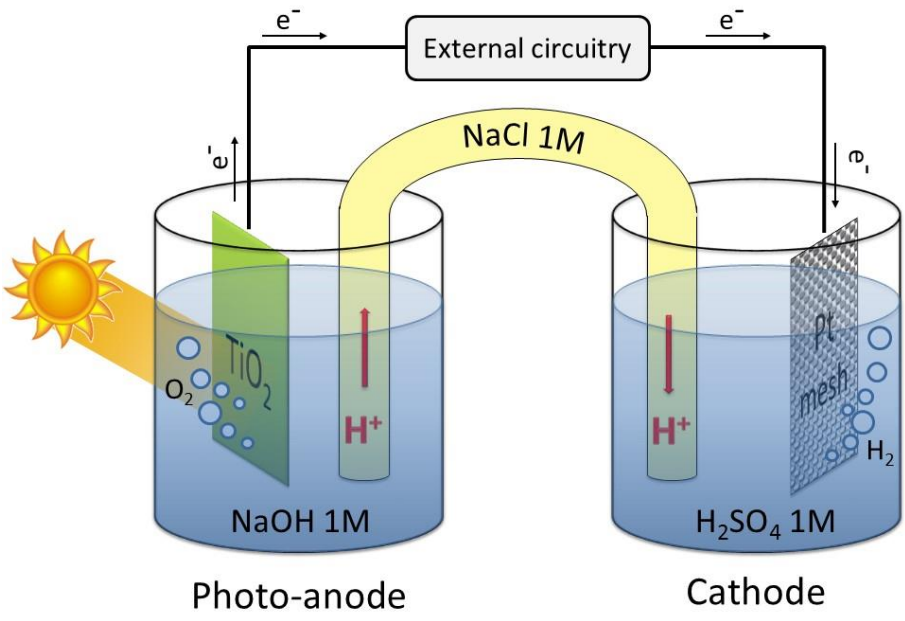

Figure 3.1: Scheme of the photo-electrochemical cell used to perform photocatalytic activity measurements.

Photocatalytic activity of V-N-codoped TiO_2 films was tested by measuring the photocurrent generated under visible light irradiation (250 W tungsten halogen lamp). The samples were used as photo-anodes in a photo-electrochemical cell (PEC) constituted by two chambers containing different aqueous electrolytes connected through a salt bridge (NaCl 1M). The photo-anode was immersed in a NaOH 1M solution and the Pt mesh cathode in an H_2SO_4 1M solution (*figure 3.1*). The difference in pH generates a chemical bias, which is necessary to

achieve the minimum value of voltage needed for water splitting. Reactor is made up of borosilicate glass, thus no UV filter was used and reactant water solution acts as filter for IR radiation. An area of 11.25 cm^2 of the photo-anode was immersed in the solution and exposed to visible light, to measure both open-circuit photo-voltage and closed-circuit photocurrent. During photocurrent measurement, small part of all glass slides with ITO/TiO_2 films is sliced from one side to expose ITO layers along the cross-section. All the ITO layers are electrically connected by applying silver paste along the cross-section. Thus once the photo-electrons are transferred to ITO from TiO_2 they travel towards electrical contact (silver) which is connected to Pt electrode where these photoelectrons are utilized to produce H_2 gas.

3.3 Results and discussion

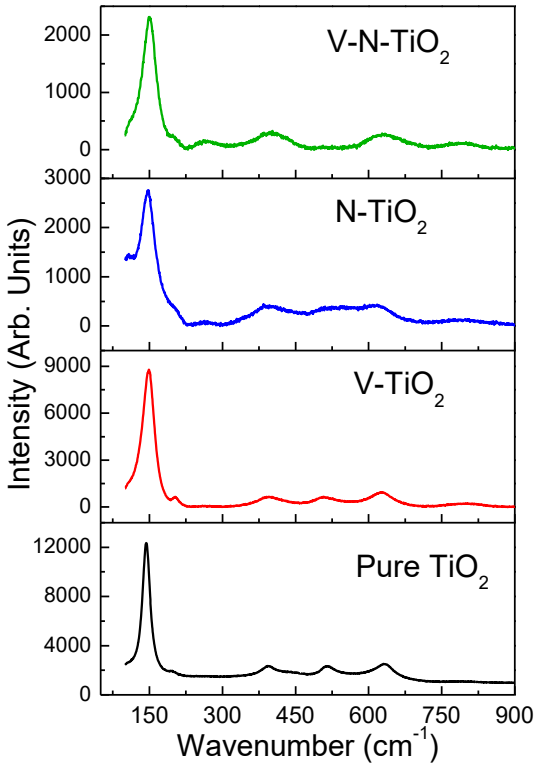

Figure 3.2: Raman spectra of pure, V-doped, N-doped and V-N-codoped TiO_2 films.

Raman spectra of pure, V-doped, N-doped, and V-N-codoped TiO_2 are presented in *figure 3.2*. Five peaks are observed in all the samples, which match well with Raman active modes, at 144 cm^{-1} (E_g), 197 cm^{-1} (E_g), 399 cm^{-1} (B_{1g}), 513 cm^{-1} (A_{1g}), and 639 cm^{-1} (E_g), of anatase phase as reported by Ohsaka [16]. This shows that the anatase crystal structure of TiO_2 is well maintained even after anion (N^-) and cation (V^{5+}/V^{4+}) doping. Comparing the four Raman spectra, a broadening of the peaks after doping and codoping is observed. In addition, the peak

at 144 cm^{-1}(E_g) also shifts towards higher wavenumber values. These features can be ascribed to smaller crystallite sizes, which affect the force constants and vibrational amplitudes of the nearest neighbor bonds [17]. Moreover, the shift of Raman peaks can also be induced by the incorporation of the dopants in the TiO_2 matrix, which causes a distortion of the lattice and forms new bonds which are not present in pure TiO_2 film. The formation of this kind of bonds is further confirmed by XPS analysis (*figure 3.3*).

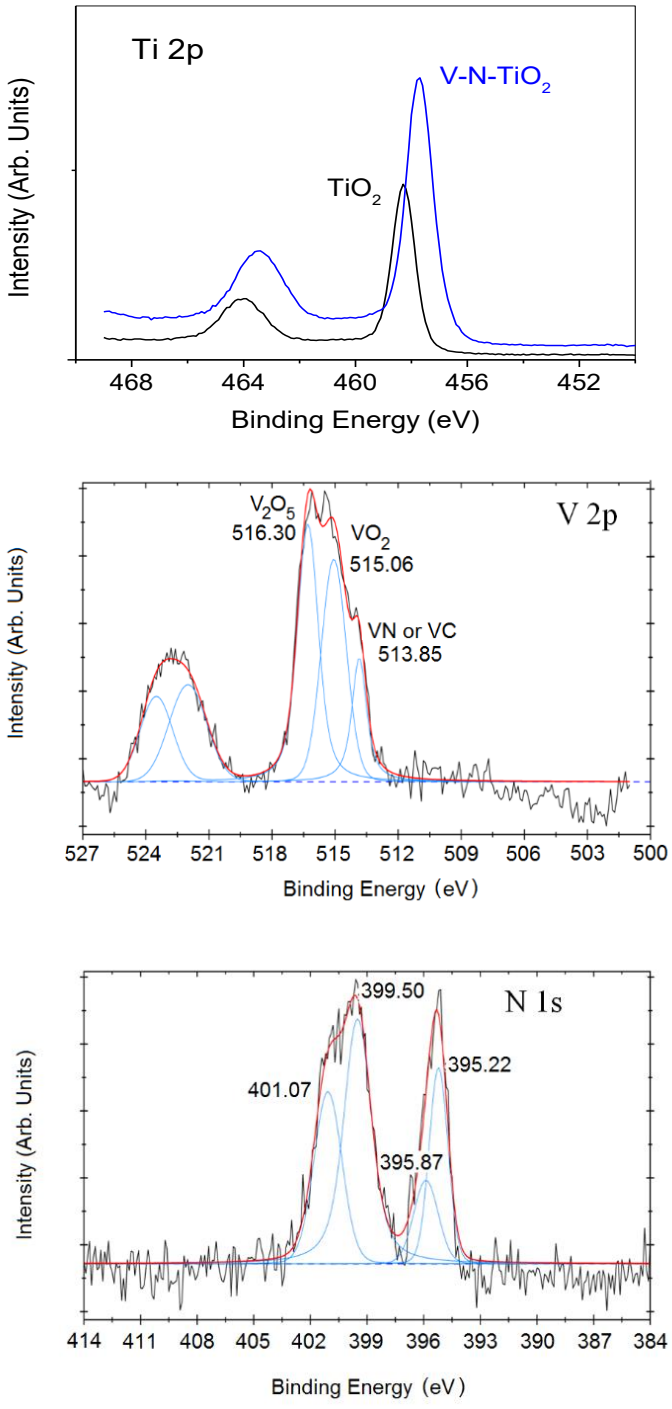

Figure 3.3: XPS spectra of Ti 2p, V 2p and N 1s levels of V-N-codoped TiO_2 film.

XPS was utilized to examine the chemical states of both the dopants incorporated into TiO_2 (*figure 3.3*). In Ti 2p core level, two peaks centered at 458.4 eV and 464.1 eV, assigned to Ti $2p_{3/2}$ and Ti $2p_{1/2}$, corresponding to +4 valence state of Ti are observed for pure TiO_2. The positions of these peaks in codoped TiO_2 are shifted by 0.7 eV towards lower binding energy (BE) values thus indicating that V and N ions are incorporated into TiO_2 lattice and influence the local chemical state of Ti^{4+} ions. Small amount (12 %) of Ti^{3+} species at 457.4 eV is also observed after deconvolution of Ti $2p_{3/2}$ peak for V-N-codoped TiO_2. This indicates oxygen vacancies created by the N doping. The positions of doublet in V 2p core levels of V-N codoped TiO_2 film indicate the co-presence of both V_2O_5 (at 516.3 eV corresponding to the V^{5+} state) and VO_2 (515.1 eV corresponding to the V^{4+} state). Due to similar radii, V^{4+} ions are expected to be incorporated in the TiO_2 lattice by substitutionally replacing Ti^{4+} ions and forming Ti-O-V bond [18] while V_2O_5 lies on the surface of the TiO_2 matrix. Moreover, the presence of VN and/or VC compounds is also observed, as indicated by the V $2p_{3/2}$ shoulder at lower BE (between 514 and 513 eV) [19-22]. The N 1s core levels show two main broad peaks at different binding energy ranges. This indicates the presence of variable electron densities around the N and hence the formation of different bonds between N, Ti, and O in the matrix. The peak at lower BE range (394 - 397.5 eV) is related to substitutional N in form of Ti–N–Ti linkages and/or NV species. The second peak is deconvoluted into two peaks centered at 399.5 and 401.1 eV, where the former is attributed to N substitutionally replacing oxygen to form O-Ti-N linkage and the latter is assigned to interstitial occupation of N and oxidized N species (NO) to form Ti-O-N and Ti-O-N-O linkage, respectively. This result indicates that N occupies both substitutional and interstitial sites in TiO_2 lattice thus inducing visible light sensitivity as proposed by Di Valentin et al. [23]. TiO_2 was codoped with V and N, 4 at.% and 2 at.%, respectively, as confirmed by XPS and EDXS analysis.

The optical properties of pure, doped, and co-doped TiO_2 were studied by measuring the absorption spectra ranging from UV (325 nm) to visible (550 nm) wavelengths and are presented in *figure 3.4*. Doping TiO_2 with V or N causes a slight shift of the absorption towards longer wavelengths. The absorption is further enhanced by co-doping with both V and N. This observation confirms that N and V ions are successfully doped into the TiO_2 crystal lattice. Using Tauc plot (*figure 3.5*), i.e. $(\alpha h\nu)^{1/2}$ versus $(h\nu)$, the band gap energies are deduced by extrapolating the linear region of the plot to intersect the photon energy axis. The calculated band gap for TiO_2 (3.2 eV) is the same reported in literature for anatase phase. N-doped TiO_2 shows a slight decrement of the band gap value (3.1 eV), given by the formation of localized N

2p states just above the valence band maximum of TiO_2 due to substitutional and interstitial N species [24, 25]. A charge-transfer from the d orbital of V^{4+} to the conduction band of TiO_2 causes a red shift of the absorption of V-doped TiO_2 (2.8 eV), which is higher than that of N-doped. In this case V^{4+} ions are incorporated into the TiO_2 lattice, which forms isolated impurity energy levels below the bottom of the TiO_2 conduction band (CB) [26]. The highest narrowing of band gap is obtained with V-N-codoped sample (2.5 eV). This result is as expected from theoretical calculations performed by Ma et al. [27]. Using first-principles calculations in the framework of density functional theory, they showed that a strong covalent bond between V and N in the codoped TiO_2 causes a slight variation in the position of the isolated energy levels as compared to those created by V and N in single element doped TiO_2. V 3d states lower the energy levels of the N 2p states to bring them closer to the VB. This enhances the mixing of N 2p and O 2p states in the VB and produces a favorable condition for holes trapping that results in a better separation of photo-generated charges. On the contrary, the position of V 3d states is shifted to low energy regions and thus diminishes any possible overlapping between V 3d and Ti 3d due to the bonding interaction between V 3d and N 2p orbitals. The above results indicate that V-N-codoped TiO_2 shows the maximum lowering of the band-gap value due to the formation of impurity energy levels in TiO_2.

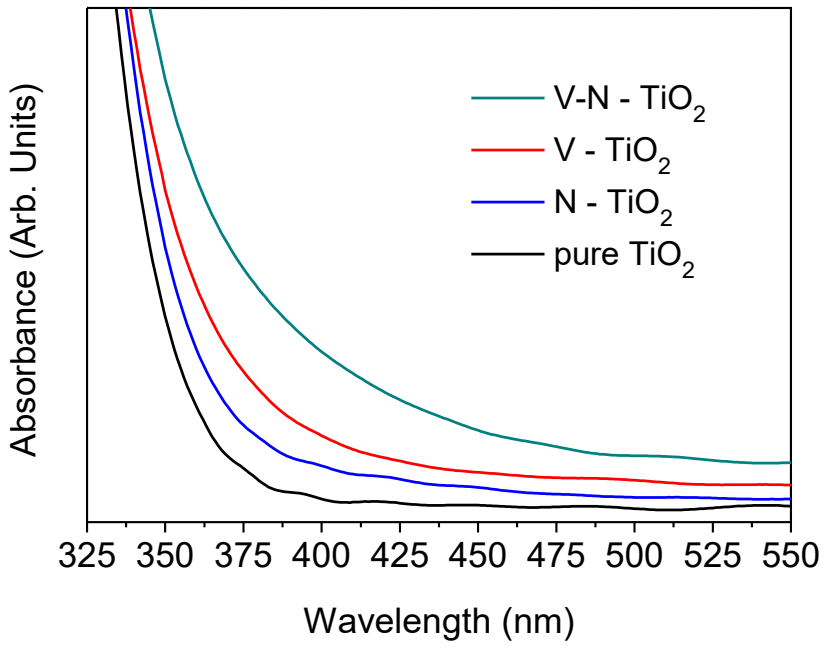

Figure 3.4: UV-Vis absorption spectra of pure, V-doped, N-doped and V-N-codoped TiO_2 films.

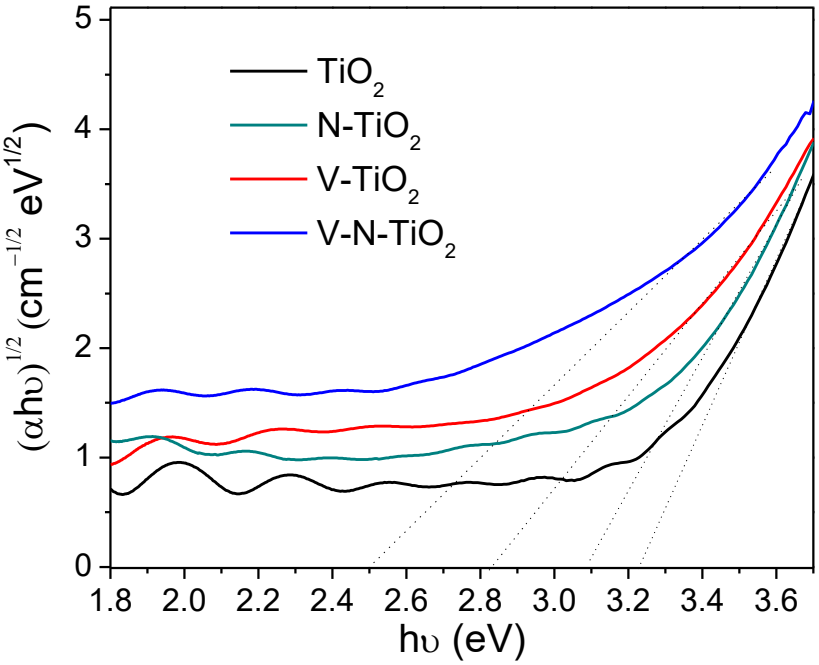

Figure 3.5: Tauc plot of pure, V-doped, N-doped and V-N-codoped TiO_2 films.

The photocatalytic activity of the samples was tested by measuring the photocurrent generated in the photo-electrochemical cell. The measured photo-voltage of all the samples (> 1.4 V) was always greater than that required to split water molecules (1.23 eV). Firstly, we checked the photo-catalytic activity of single ITO/V-N-codoped TiO_2 bi-layer films. ITO layer is used because it not only gives a back electrical contact for the electrons, but also generates a space charge layer near the interface of TiO_2 to allow a fast separation of the photo-generated charge carriers (*figure 3.6)*. The conduction band edge of ITO (~ -4.5 eV) is at an energy value lower than that of TiO_2 (~ -4.0 eV) and this favors the injection of electrons from the latter into the former. Once the photoelectron from TiO_2 is injected in ITO, it has a very low probability of back transfer and, as a result, electrons and holes are definitely separated.

For pure TiO_2, the photocurrent is 290 μA, which increases after vanadium doping (360 μA) but decreases after N-doping (90 μA). The photocurrent value further enhances for V-N-codoped sample (480 μA). This incremental trend is due to the inclusion of dopant ions in the lattice of TiO_2, which, by forming impurity levels inside its band-gap, is able to absorb higher amount of visible light. In addition, V and N species present in low concentration also act as electron and hole trapping sites, respectively, for better charge separation. The lower value of the band gap in V-N-codoped TiO_2 suggests that this film should be able to absorb significantly

higher amount of photons in visible light range than the other samples, but this is not reflected in the photocurrent values where the increase is only by small amount.

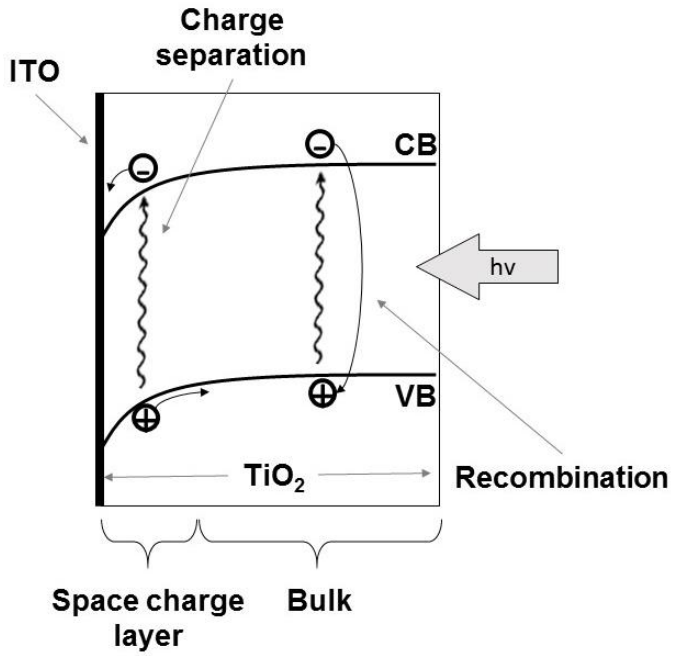

Figure 3.6: Schematic representation of ITO/TiO_2 single bilayer film. Charge carriers generated near the interface are separated by the electric field of the space charge layer. Charge carriers generated in the bulk of the film, far from the interface, undergo recombination.

Single bi-layer films are formed by a layer of about 50 nm of ITO at the bottom with a thick (about 750 nm) V-N-codoped TiO_2 layer on it. This means that most of the photo-electrons are generated far from the ITO/TiO_2 interface and don't feel the driving force provided by the electric field generated in the space charge layer at the interface (*figure 3.6*). Thus, most of the photoelectrons have to travel some distance within the TiO_2 itself before entering the space-charge region and this increases the probability of electron-hole recombination especially in doped TiO_2 where dopant can also act as recombination sites. To efficiently suppress the recombination of charge carriers, the strategy of multilayer films was adopted, in which the thickness of each TiO_2 layer is decreased by introducing ITO layers, as described in the experimental part. This approach creates several space charge layers in form of ITO/V-N-codoped TiO_2 interfaces.

Cross-section SEM images of the multilayer film with 4-bilayers of ITO/co-doped TiO_2 are shown in *figure 3.7*. The columnar structure of the film is clearly visible in the left image, given by secondary electrons signal. Right image is given by backscattered electrons signal and

allows compositional analysis. Here, the white layer of ITO can be easily distinguished from the dark layer of co-doped TiO_2 and for this reason both the periodicity and continuity of the layers are clearly visible. This image was used also for thickness measurements. ITO is a transparent conducting oxide with a direct band gap in the range of 3.9 - 4.2 eV, which is significantly higher than the absorption edge of co-doped TiO_2 layer; thus, ITO deposited on the top of TiO_2 layer does not affect the amount of photons reaching the TiO_2 layer. This feature was experimentally confirmed by measuring the absorption spectra of multilayer films: the spectra showed similar red shift in the band edge as that observed with single layer.

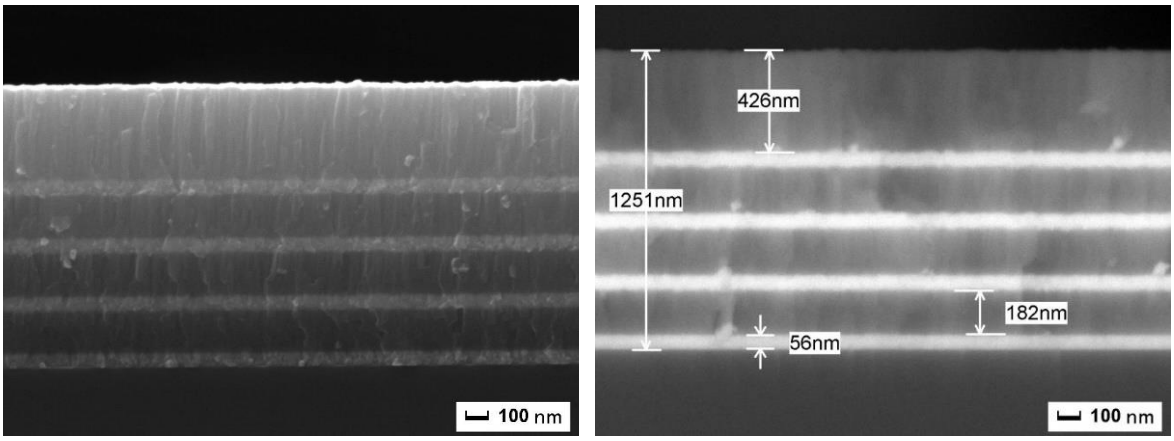

Figure 3.7: Cross-section SEM image of ITO/V-N-codoped TiO_2 multilayer film structure (secondary electrons image on the left and backscattered electrons image on the right)

All the multilayer films were able to produce photo-voltage greater than that required to split the water irrespective of number of bilayers. The photocurrent increases significantly from 480 μA (for single-bilayer film) to 880 μA by depositing 3-bilayers film (*figure 3.8*). In this film, the previous V-N-codoped TiO_2 layer having thickness of 750 nm was divided into three layers of 250 nm by introducing two more ITO layers. The photocurrent increases with the number of bilayers and reaches a nearly constant value (1 mA) for the highest number of bilayers (4, 5, and 6) (*figure 3.8*).

The film giving the best photocurrent value (1 mA) is the one with 4-bilayers. This film contains seven ITO/TiO_2 interfaces where space charge layer is formed. Moreover, the decreased thickness of the V-N-codoped TiO_2 layers assures that the photo-generated electrons have to travel a short distance into TiO_2 (the unshielded region) before being injected into the ITO layer where recombination is definitely hindered.

Another relevant point to be considered is that in single bilayer film the photo-electrons, generated in the V-N-codoped TiO_2 layer, have to move only along one direction to reach the ITO layer placed at the one end of the layered structure. On the contrary, in multilayer film each

V-N-codoped TiO_2 layer is sandwiched between two ITO layers and so the photo-electrons can move along either of two directions to avoid recombination. All these reasons favor the increment of the photo-current in the 4-bilayers film. A saturation effect is clearly expected on physical basis, but what is important here is that the photocurrent value depends not only on thickness but also on the number of bilayers, i.e., on the ability of the multilayer structure to efficiently avoid charges recombination.

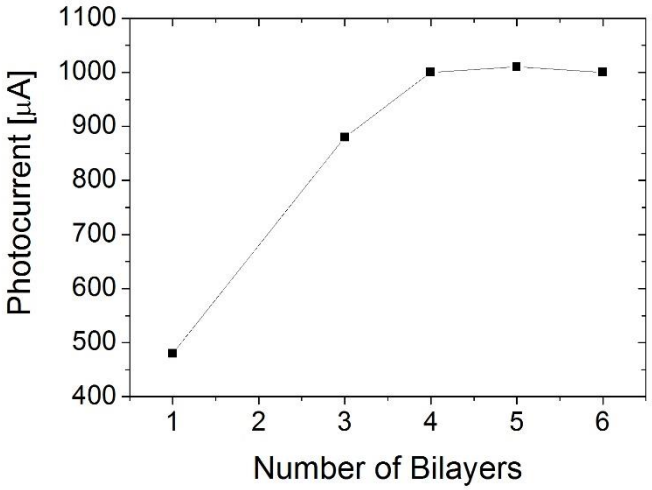

Figure 3.8: Photocurrent of ITO/V-N-codoped TiO_2 multilayer film as a function of number of bilayers.

3.4 Conclusions

Formation of isolated energy levels near the conduction and valence bands, by incorporation of V and N in TiO_2 lattice, causes an effective narrowing of the band gap to 2.5 eV. The dopants, at low concentration, act as traps for photo-excited holes or electrons thus enhancing the separation of electron-hole pair that is also favored by the charge separation operated at the interface between V-N-codoped TiO_2 and ITO because of the relative positions of the bottom conduction band of the two layers. In multilayer structure, the generated photoelectrons, travelling into TiO_2 film of limited thickness, rapidly enter the space charge interface of the ITO/TiO_2 films from where they are instantaneously injected into the ITO layer and then removed towards the cathode. The synergistic effects created by band narrowing and enhanced charge separation by using multilayer structure and codoping strategy in TiO_2 generate higher photocurrent for water splitting under visible light that definitely exceeds that obtained by doping TiO_2 with a single, V or N, element.

3.5 References

1. Fujishima, A., X. Zhang, and D.A. Tryk, *TiO_2 photocatalysis and related surface phenomena.* Surface Science Reports, 2008. **63**(12): p. 515-582.
2. Ni, M., et al., *A review and recent developments in photocatalytic water-splitting using TiO_2 for hydrogen production.* Renewable and Sustainable Energy Reviews, 2007. **11**(3): p. 401-425.
3. Litter, M.I. and J.A. Navío, *Photocatalytic properties of iron-doped titania semiconductors.* Journal of Photochemistry and Photobiology A: Chemistry, 1996. **98**(3): p. 171-181.
4. Dholam, R., et al., *Efficient indium tin oxide/Cr-doped-TiO_2 multilayer thin films for H_2 production by photocatalytic water-splitting.* International Journal of Hydrogen Energy, 2010. **35**(18): p. 9581-9590.
5. Choi, W., A. Termin, and M.R. Hoffmann, *The role of metal ion dopants in quantum-sized TiO_2: Correlation between photoreactivity and charge carrier recombination dynamics.* Journal of Physical Chemistry, 1994. **98**(51): p. 13669-13679.
6. Zhu, J., et al., *Hydrothermal doping method for preparation of Cr^{3+}-TiO_2 photocatalysts with concentration gradient distribution of Cr^{3+}.* Applied Catalysis B: Environmental, 2006. **62**(3-4): p. 329-335.
7. Dholam, R., N. Patel, and A. Miotello, *Efficient H_2 production by water-splitting using indium-tin-oxide/V-doped TiO_2 multilayer thin film photocatalyst.* International Journal of Hydrogen Energy, 2011. **36**(11): p. 6519-6528.
8. Dholam, R., et al., *Hydrogen production by photocatalytic water-splitting using Cr- or Fe-doped TiO_2 composite thin films photocatalyst.* International Journal of Hydrogen Energy, 2009. **34**(13): p. 5337-5346.
9. Ananpattarachai, J., P. Kajitvichyanukul, and S. Seraphin, *Visible light absorption ability and photocatalytic oxidation activity of various interstitial N-doped TiO_2 prepared from different nitrogen dopants.* Journal of Hazardous Materials, 2009. **168**(1): p. 253-261.
10. Cong, Y., et al., *Synthesis and characterization of nitrogen-doped TiO_2 nanophotocatalyst with high visible light activity.* Journal of Physical Chemistry C, 2007. **111**(19): p. 6976-6982.
11. Dozzi, M.V. and E. Selli, *Doping TiO_2 with p-block elements: Effects on photocatalytic activity.* Journal of Photochemistry and Photobiology C: Photochemistry Reviews, 2013. **14**: p. 13-28.
12. Park, H., et al., *Surface modification of TiO_2 photocatalyst for environmental applications.* Journal of Photochemistry and Photobiology C: Photochemistry Reviews, 2013. **15**: p. 1-20.
13. Gai, Y., et al., *Design of narrow-gap TiO_2: a passivated codoping approach for enhanced photoelectrochemical activity.* Physical review letters, 2009. **102**(3): p. 036402.

14. Zhang, J., et al., *Development of modified N doped TiO_2 photocatalyst with metals, nonmetals and metal oxides.* Energy and Environmental Science, 2010. **3**(6): p. 715-726.
15. Cong, Y., et al., *Preparation, photocatalytic activity, and mechanism of nano-TiO_2 co-doped with nitrogen and iron (III).* The Journal of Physical Chemistry C, 2007. **111**(28): p. 10618-10623.
16. Ohsaka, T., *Temperature dependence of the Raman spectrum in Anatase TiO_2.* Journal of the Physical Society of Japan, 1980. **48**(5): p. 1661-1668.
17. Choi, H.C., Y.M. Jung, and S.B. Kim, *Size effects in the Raman spectra of TiO_2 nanoparticles.* Vibrational Spectroscopy, 2005. **37**(1): p. 33-38.
18. Wu, J.C.S. and C.H. Chen, *A visible-light response vanadium-doped titania nanocatalyst by sol-gel method.* Journal of Photochemistry and Photobiology A: Chemistry, 2004. **163**(3): p. 509-515.
19. Shopova-Gospodinova, D., et al., *Synthesis of V-doped TiO_2 films by chemical bath deposition and the effect of post-annealing on their properties.* Thin Solid Films, 2012. **520**(18): p. 5928-5935.
20. Moulder, J.F., et al., *Handbook of X-ray Photoelectron Spectroscopy*. 1992, Eden Prairie, MN, USA: Perkin-Elmer Corp.
21. Nguyen, T.B., M.J. Hwang, and K.S. Ryu, *High adsorption capacity of V-doped TiO_2 for decolorization of methylene blue.* Applied Surface Science, 2012. **258**(19): p. 7299-7305.
22. Benoit, R., *LaSurface Web Site*. 2001, Centre National de la Recherche Scientifique (CNRS) in conjunction with Thermo Fisher Scientific: France.
23. Di Valentin, C., et al., *Characterization of paramagnetic species in N-doped TiO_2 powders by EPR spectroscopy and DFT calculations.* Journal of Physical Chemistry B, 2005. **109**(23): p. 11414-11419.
24. Liu, J., et al., *Enhanced photoactivity of V-N codoped TiO_2 derived from a two-step hydrothermal procedure for the degradation of PCP-Na under visible light irradiation.* Journal of Physical Chemistry C, 2011. **115**(11): p. 4507-4515.
25. Huang, D.G., et al., *Synthesis of samarium- and nitrogen-co-doped TiO_2 by modified hydrothermal method and its photocatalytic performance for the degradation of 4-chlorophenol.* Journal of Physics and Chemistry of Solids, 2009. **70**(5): p. 853-859.
26. Zhou, W., et al., *Preparation and properties of vanadium-doped TiO_2 photocatalysts.* Journal of Physics D: Applied Physics, 2010. **43**(3).
27. Ma, X., et al., *Synergistic effect of V/N-codoped anatase TiO_2 photocatalysts.* Solid State Communications, 2010. **150**(13-14): p. 689-692.

Chapter 4

Synthesis of mesoporous ITO/TiO_2 electrodes[1]

In the previous chapter, we have seen the crucial role of ITO/TiO_2 interface in promoting the separation of electron-hole pairs. In this chapter, we focused on the fabrication by a single RF-magnetron sputtering deposition process of ITO/TiO_2 mesoporous electrodes. The enhanced electrochemical properties are explained in terms of increased surface area and improved charge transfer properties.

4.1 Introduction

Elevated surface area and good charge transfer are two of the main requirements for applications in the solar energy conversion devices such as sensitized solar cells and photo-electrochemical cells for hydrogen production [1, 2]. Compared to compact films, mesoporous TiO_2 layers offer higher active surfaces, resulting advantageous for photocatalytic applications [3, 4]. Compact and porous layers of TiO_2 can be deposited on sputter-deposited ITO by means of several deposition techniques such as spin-coating, doctor-blade or screen-printing of costly nano-TiO_2 pastes, followed by high temperature sintering process [5, 6]. In this work, we focus on the fabrication of mesoporous ITO/TiO_2 electrodes by a single RF-magnetron sputtering deposition process. The mesoporous morphology was obtained by tuning the sputtering deposition parameters. Scanning electron microscopy provided a deeper insight into the electrode building, which resulted composed by a compact ITO layer, tapered with columnar ITO nanocrystals, completely covered with jagged anatase TiO_2 cauliflower-like structures. The

[1] This chapter is based on the results published in: E. Binetti, Z. El Koura, N. Bazzanella, G. Carotenuto, and A. Miotello; Materials Letters 139 (2015) 355–358.

compact ITO layer ensures the electron transport in the film, while rod-shaped ITO crystals offer an elevated active surface area for the charge transfer at the interface. In addition, the formation of porous TiO_2 layer led to an enhancement of its active surface for catalytic/electrochemical processes. Such mesoporous electrodes exhibited enhanced electrochemical performances, compared to those of compact thin-film heterojunctions, due to the increased surface area and the enhanced charge transfer at the ITO/TiO_2 interface.

4.2 Experimental section

4.2.1 RF sputtering deposition of ITO/TiO_2 electrodes

ITO/TiO_2 electrodes were deposited by RF-magnetron sputtering on glass and silicon (100) slides. The deposition chamber was evacuated up to a pressure lower than $3x10^{-7}$ mbar, and then an Ar flux (purity 99.99%) was put in to reach the deposition pressure of $8x10^{-3}$ mbar. The sputtering targets were ITO (purity 99.99%) and TiO_2 (purity 99.99%), and the sputtering RF powers were 100 and 150 W, for the first and second target respectively. To remove the surface contaminations, both targets were cleaned by 20 minutes of pre-sputtering before each deposition process. The target-substrate distance was kept constant at 6.0 cm, and the substrate holder was kept swinging to improve the film homogeneity. Substrate temperature (T_S) was maintained at 350 ± 10 °C using an electric heater and a thermocouple installed inside the holder, in contact with a copper plate on which substrates were fixed. Compact ITO/TiO_2 samples were obtained by 16 minutes of deposition of ITO, corresponding to ~400 nm in thickness, followed by 60 minutes of deposition of TiO_2 (~500 nm in thickness). In order to achieve mesoporous structure (MP), ITO target was pre-sputtered at higher pressure (>2.0 10^{-2} mbar), and a short-deposition (~10 seconds) was carried out on substrates at room temperature, accordingly with the Thorton's Structure-Zone Model for sputtering [7]. MP-electrodes were obtained by 16 minutes of ITO deposition, followed by 45 and 90 minutes of TiO_2 deposition: corresponding samples are named as MP-45 and MP-90.

4.2.2 Characterization techniques

Scanning electron microscopy (SEM) was used to analyze mesoporous ITO/TiO_2 films morphology in top view and cross section. Measurements were performed using a JEOL JSM-7001F FEG-SEM at 20 keV electron beam energy. SEM images allow pointing out complex ITO/TiO_2 structure, thanks to back-scattered (BS) electron ability to distinguish different

atomic number materials also some hundreds of nanometers below the surface. Raman spectroscopy was carried out with a Labram Aramis Jobin-Yvon Horiba μ-Raman system equipped with a He-Ne laser source (632.8 nm); the instrument was calibrated using the Raman mode at 520.4 cm^{-1} of Si. Electrochemical measurements were carried out with a Gamry potentiostat/galvanostat/ZRA Interface 1000 using a three-electrodes cell (*figure 4.1*) composed by a Standard Calomel Electrode (SCE, +0.241 V Vs NHE) as reference, Pt-mesh as counter-electrode and 1.0M KOH solution as electrolyte. Linear sweep voltammetries were carried out with a scan rate of 10 mV/s, and the measured currents were normalized by the electrode surface.

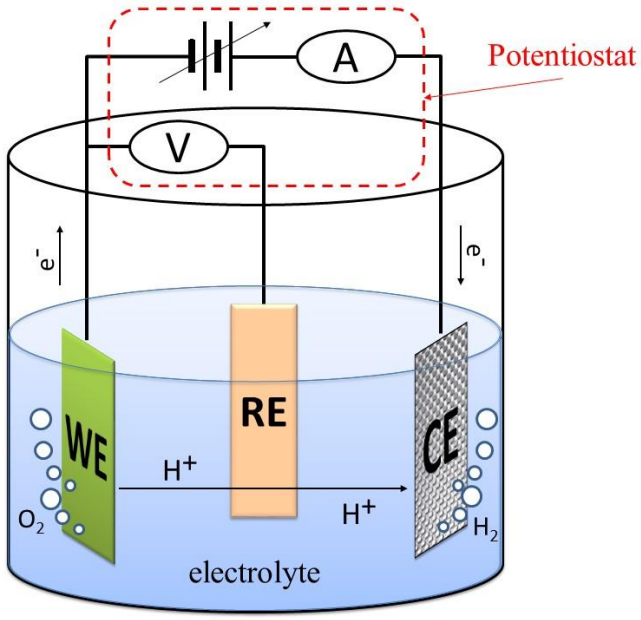

Figure 4.1: Scheme of the cell used for electrochemical measurements. WE is the working electrode, where oxygen evolution reaction takes place. RE is the reference electrode, namely the standard calomel electrode (SCE). CE is the counter electrode (in our case a platinum mesh), where hydrogen evolution reaction takes place.

4.3 Results and discussion

The morphological analysis has been performed in order to investigate the film structure both on the surface and along the cross-section. *Figure 4.2-A* reports the surface morphology of porous ITO/TiO_2 films. It appears composed by the top ends of a dense array of columnar crystals, hundreds of nm in diameter, with jugged surfaces. It also shows the presence of pores among the jugged structures, whose size ranges from few tens to several hundreds of nm. *Figure*

4.2-B shows the cross-section SEM image, composed by the overlapping of signals coming out from back-scattered electrons (BS - red) and secondary electrons (SE - green). *Figure 4.2-C* reports a high-magnification SE-SEM image of a single ITO/TIO_2 hetero-structure. Cross-section SEM analysis reveals that the samples are composed by a compact ITO layer, about 250 nm thick, on which columnar ITO nanocrystals are grown. The successive TiO_2 deposition occurred on such ITO morphology, causing the formation of jagged TiO_2 cauliflower-like structures, whose diameter increases with the height, spaced by pores. The size of both cauliflower-like structures and of the pores among them has been estimated by an accurate SEM analysis (*figures 4.3* and *4.4*). The pores formed among the ITO/TiO_2 structure have diameters lower than 100 nm, and are extended over the full sample width. Nevertheless, ITO seems to be completely covered by TiO_2, thus limiting the occurrence of recombination processes.

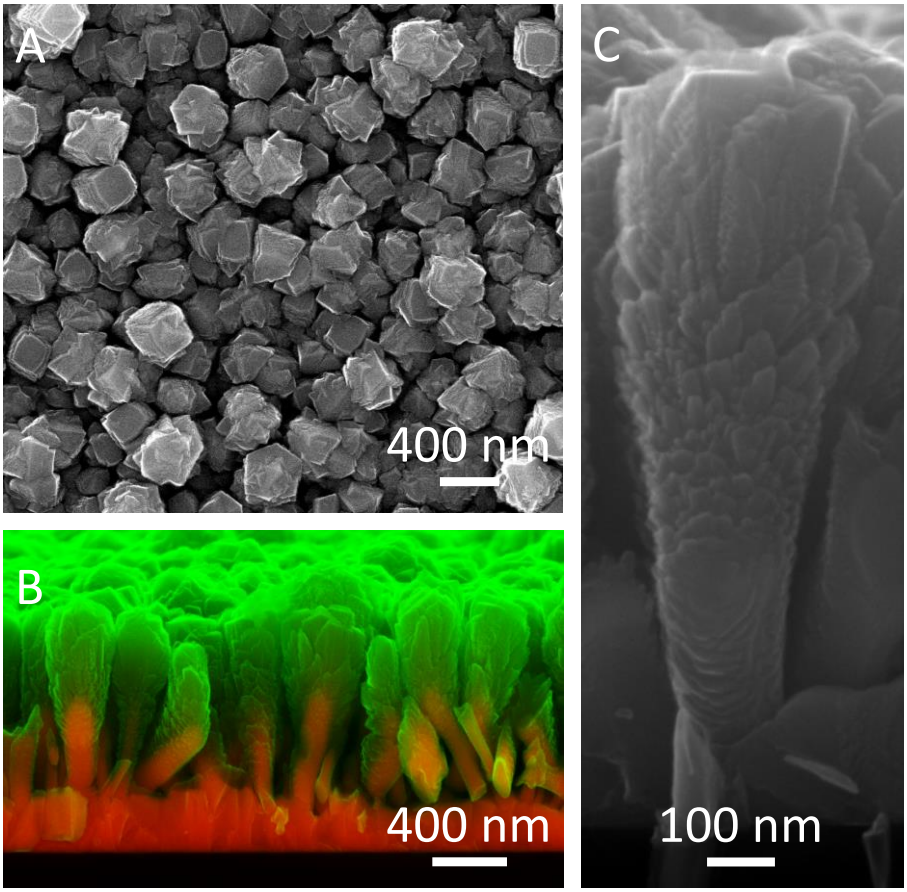

Figure 4.2: Top view (A) and cross-section (B - C) SEM analysis of MP-90. The image in panel (B) is composed by the overlapping of the two images obtained by collecting back-scattered electrons (red) and secondary electrons (green).

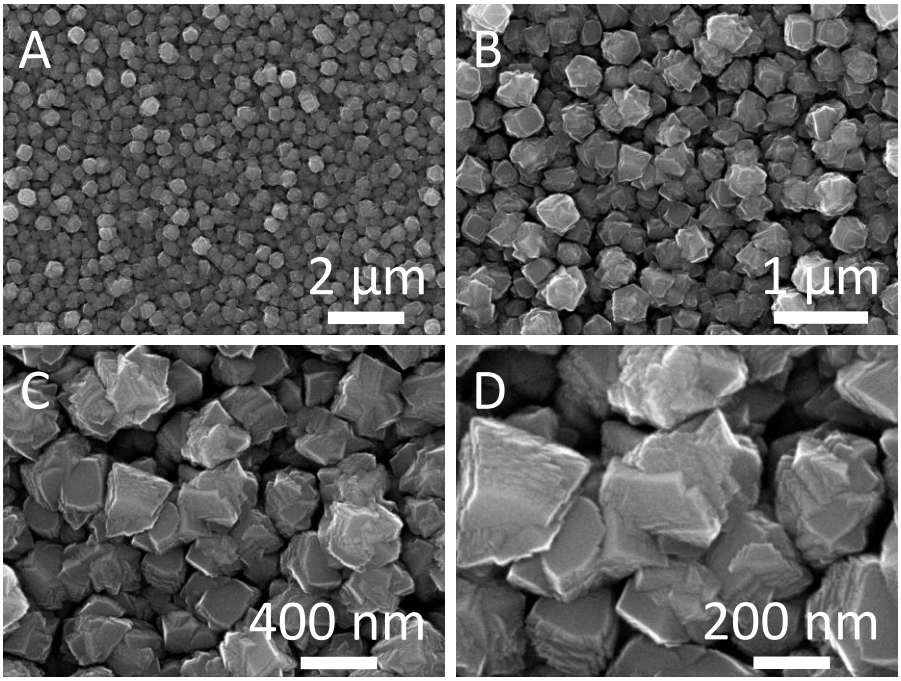

Figure 4.3: SEM images of MP-90.

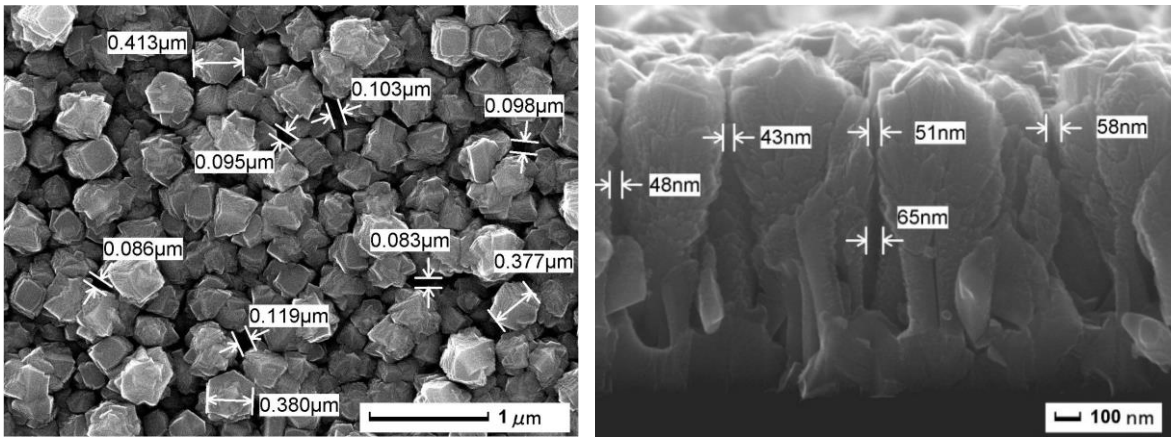

Figure 4.4: Top-view and cross-section SEM analysis of cauliflower-like structure and pores in MP-90.

Raman analysis has been performed to achieve information on the TiO_2 crystalline phase. *Figure 4.5* reports the normalized Raman spectra of ITO/TiO_2 both compact and mesoporous films. The spectra line-shape is compatible with the anatase crystalline phase, characterized by six allowed modes at 144 cm^{-1} (E_g), 197 cm^{-1} (E_g), 399 cm^{-1} (B_{1g}), 513 cm^{-1} (A_{1g}), and 639 cm^{-1} (E_g) [8]. It is worth to notice that A_{1g} peak at 513 cm^{-1} and B_{1g} peak 519 cm^{-1} (B_{1g}) are not resolved. The main peak position and the corresponding full width mid height (FWMH) are

reported in *table 4.1*. A slight shift at higher energy of E_g peak at 144 cm^{-1}, concomitantly to a peak enlargement, was detected passing from compact ITO/TiO_2 to mesoporous structures, as well as a clear A_{1g} peak weakening. Both the phenomena can be ascribed to a size-reduction of TiO_2 crystallites composing the film [9]. Indeed, both the blue-shift, the enlarging of E_g peak, and the weakening of A_{1g} peak are more evident in MP-45 than in MP-90, since it is made of smaller TiO_2 structures. Nevertheless, it would also be possible that the A_{1g} Raman mode is limited in such cauliflower-like arrangements. Anatase crystalline phase is also confirmed by XRD patterns (*figure 4.*6).

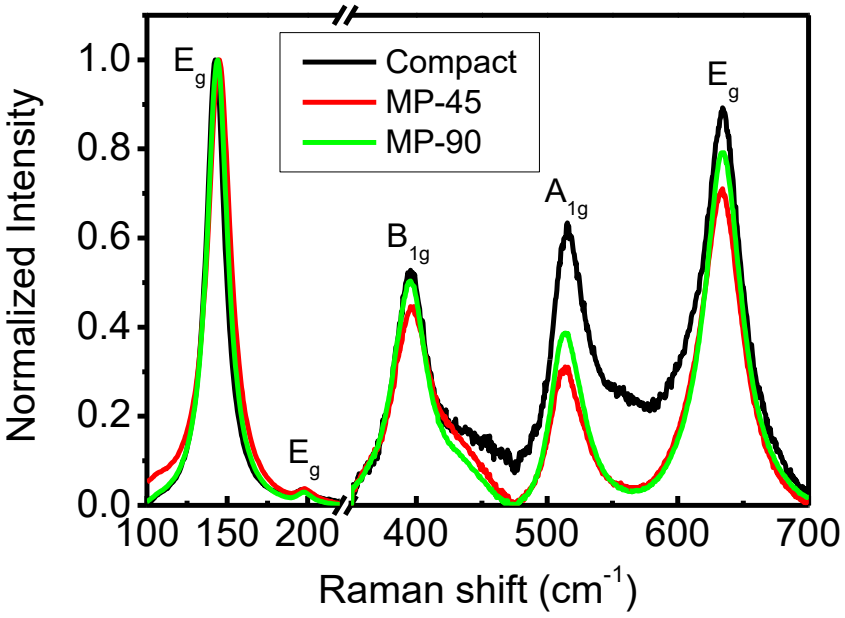

Figure 4.5: Normalized Raman spectra of ITO/TiO_2 samples: compact, MP-45, and MP-90. After the break the intensity is multiplied by 10.

	E_g(cm^{-1})	B_{1g}(cm^{-1})	A_{1g}(cm^{-1})	E_g(cm^{-1})
Compact	142.5 (14.4)	395.5 (33.1)	514.4 (36.6)	634.2 (38.7)
MP-45	145.0 (17.5)	395.5 (37.2)	513.8 (29.7)	634.2 (37.6)
MP-90	144.0 (15.4)	395.5 (31.8)	514.9 (28.1)	635.3 (33.4)

Table 4.1: Position and FWMH (in parentheses) of the main Raman peaks.

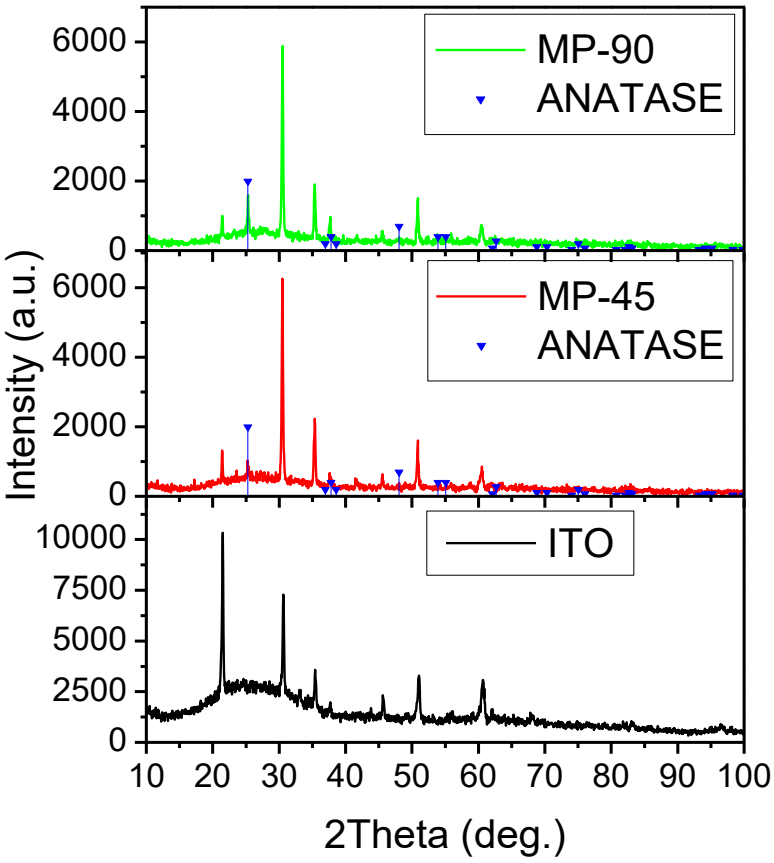

Figure 4.6: XRD patterns of ITO, MP-45 and MP-90.

Electrochemical performances were valued by observing the oxygen evolution reaction (OER) in LSV experiments, carried out with a scan rate of 10 mV/s [10, 11]. *Figure 4.7* reports the LSV curves of the mesoporous samples, compared to ITO/TiO_2 compact films. As expected, mesoporous electrodes showed enhanced electrochemical performances. Indeed, the current density at 1.23 V (Vs. NHE) reached respectively 0.41 and 0.38 mA/cm^2 in the case of MP-45 and MP-90, while compact ITO/TiO_2 electrodes yield only 0.11 mA/cm^2. The enhanced electrochemical performances can be ascribed both to the elevated interface between the ITO and TiO_2, but also to the improved surface offered by the TiO_2 to the electrolyte. However, since no improvements have been obtained by increasing the TiO_2 thickness, passing from MP-45 to MP-90, the enhanced performance can be mainly ascribed to the elevated ITO/TiO_2 interface.

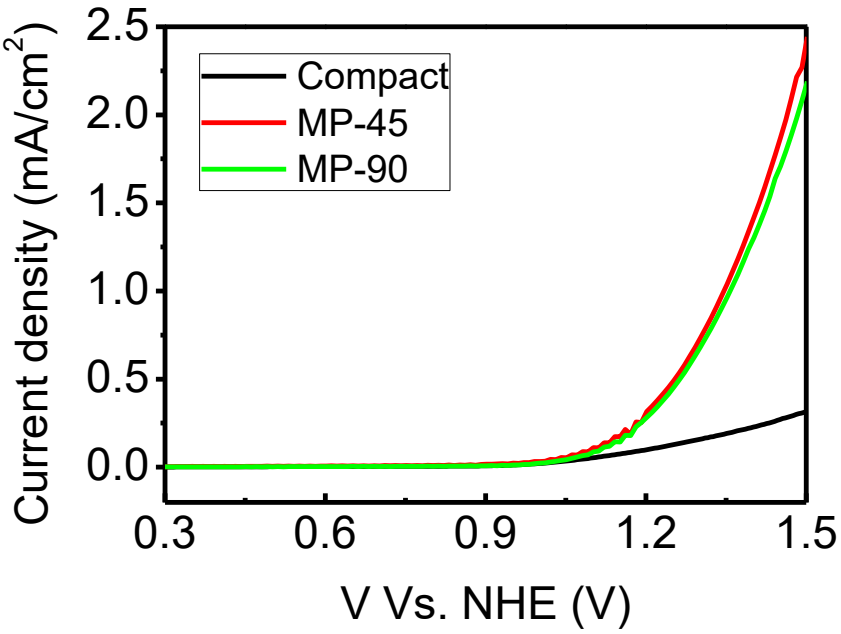

Figure 4.7: LSV of ITO/TiO_2 compact, MP-45 and MP-90.

4.4 Conclusions

Mesoporous ITO/TiO_2 electrodes were successfully prepared by a single RF-sputtering process, without any further processing. The electrodes resulted composed by a compact ITO layer, tapered with rod-like ITO nanocrystals on which cauliflower-like TiO_2 structure in anatase crystalline phase were grown. Electrochemical characterization revealed that electrodes resulted optimal in charge transfer since they offer an elevated interface between the ITO and the TiO_2, making them appealing for electrochemical applications.

4.5 References

1. Wolcott, A., et al., *Photoelectrochemical water splitting using dense and aligned TiO_2 nanorod arrays.* Small, 2009. **5**(1): p. 104-111.
2. Grätzel, M., *Recent advances in sensitized mesoscopic solar cells.* Accounts of Chemical Research, 2009. **42**(11): p. 1788-1798.
3. Tamiolakis, I., et al., *One-pot synthesis of highly crystalline mesoporous TiO_2 nanoparticle assemblies with enhanced photocatalytic activity.* Chemical Communications, 2012. **48**(53): p. 6687-6689.
4. Zheng, X., et al., *Mesoporous TiO_2 single crystals: Facile shape-, size-, and phase-controlled growth and efficient photocatalytic performance.* ACS Applied Materials and Interfaces, 2013. **5**(21): p. 11249-11257.
5. Kumar, A.S., et al., *Preparation, characterization and photoelectrochemical properties of hydrophilic Sn doped TiO_2 nanostructures.* Materials Letters, 2014. **123**: p. 149-152.
6. Li, W., et al., *A perspective on mesoporous TiO_2 materials.* Chemistry of Materials, 2014. **26**(1): p. 287-298.
7. Thornton, J.A., *Influence of apparatus geometry and deposition conditions on the structure and topography of thick sputtered coatings.* J Vac Sci Technol, 1974. **11**(4): p. 666-670.
8. Ohsaka, T., *Temperature dependence of the Raman spectrum in Anatase TiO_2.* Journal of the Physical Society of Japan, 1980. **48**(5): p. 1661-1668.
9. Choi, H.C., Y.M. Jung, and S.B. Kim, *Characterization of raman spectra of size-selected TiO_2 nanoparticles by two-dimensional correlation spectroscopy.* Bulletin of the Korean Chemical Society, 2004. **25**(3): p. 426-428.
10. Orlandi, M., et al., *Pulsed-Laser Deposition of Nanostructured Iron Oxide Catalysts for Efficient Water Oxidation.* ACS Applied Materials & Interfaces, 2014. **6**(9): p. 6186-6190.
11. Paracchino, A., et al., *Highly active oxide photocathode for photoelectrochemical water reduction.* Nature Materials, 2011. **10**(6): p. 456-461.

Chapter 5

Rapid hydrogenation of amorphous TiO_2 to produce efficient H-doped anatase for photocatalytic water splitting[1]

Hydrogen doping was reported to enhance the photocatalytic activity of TiO_2. However, it is still under debate whether hydrogen doping causes a red shift in the absorption of TiO_2 or limits the recombination of charge carriers. In this chapter, we present a simple and rapid hydrogenation method to produce H-doped Anatase TiO_2 films. The characterization of the samples allows explaining the enhanced photo-electrochemical performance in terms of suppression of the fast recombination of photo-generated charge carriers.

5.1 Introduction

Recently some authors reported on doping TiO_2 with hydrogen, which lead to the formation of oxygen vacancies, Ti^{3+} species, and hydroxyl groups [1]. However, it is still under debate which specie causes the enhancement of the photocatalytic activity. Indeed, the formation of Ti^{3+} ions leads to the generation of energy levels between 0.27 and 0.87 eV below the conduction band of TiO_2, improving the donor density [2]. On the other hand, hydrogen atoms can be easily incorporated into TiO_2 lattice, passivating dangling bonds and stabilizing disordered structures [1, 3]. In this case, the enhanced photocatalytic activity of H-doped TiO_2 can be ascribed to the suppression of the fast recombination of photoexcited carriers in the mid-gap states [4-6].

[1] This chapter is based on the results published in: E. Binetti, Z. El Koura, N. Patel, A. Dashora, and A. Miotello; Applied Catalysis A: General 500 (2015) 69–73

The main methodologies for the preparation of H-doped TiO_2 are based on chemical or electrochemical modifications of TiO_2. It is well know that TiO_2 is a stable and chemically inert material, thus its modification requires enforced conditions. Several authors reported the reduction of distinct TiO_2 morphologies, i.e. powder or nanowires, by annealing in high-pressure H_2 atmosphere at temperatures higher than 350°C for several hours [7, 8]. However, electrochemical techniques, unequivocally versatile, cheap and scalable, seem to be widely suitable for the TiO_2 reduction [9].

Here we demonstrate that amorphous TiO_2, generally easy to prepare but not efficient for several applications [10], can be converted into hydrogen-doped anatase TiO_2 by a mild annealing in hydrogen atmosphere. ITO/TiO_2 thin films were deposited on glass slides by RF-magnetron sputtering and heat treated in different ranges of temperature (250 - 350°C), atmosphere (air, 1.0 - 5.0 bar of H_2) and time (10 minutes – 72 hours), in order to find out the optimal conditions to achieve H-doped anatase. As a result, H-doped anatase phase was achieved from amorphous TiO_2 thin-films treated under mild annealing conditions (300 °C in 1.0 bar of H_2 pressure for 10 minutes). Contrariwise, lower temperature annealing did not produce any effect on the samples even for very long treatments (72 hours), while annealing at higher temperatures resulted in rutile-rich thin-films even at the shortest duration (10 minutes). By contrast, anatase thin-films resulted insensitive to the same annealing conditions. XPS analysis of H-doped anatase revealed that H atoms are bonded to O and that Ti^{4+} is not reduced to Ti^{3+}, proving that the effect of H doping is the passivation of dangling bonds in disordered/amorphous thin-films and not the formation of oxygen vacancies. This was furtherly confirmed by UV-vis absorption spectra, which did not evidence any significant variation in light absorption induced by H-doping. Finally, H-doped and pure anatase TiO_2 films were tested as photoanodes in a photoelectrochemical cell. H:TiO_2 showed enhanced photocatalytic activity as compared to pure TiO_2, which can be accounted to the ability of H atoms to stabilize the dangling bonds in amorphous disordered TiO_2, reducing the density of electron-hole recombination centers.

5.2 Experimental

5.2.1 Deposition

ITO/TiO_2 electrodes were deposited by RF-magnetron sputtering on glass and silicon (100) substrates. The deposition chamber was evacuated up to a base pressure lower than $3x10^{-7}$ mbar, then an Ar flux (purity 99.99%) was introduced to reach the deposition pressure of $8x10^{-3}$ mbar.

Pure ITO (purity 99.99%) and TiO_2 (purity 99.9%) targets were sputtered with RF power of 100 and 150 W, respectively. To remove the surface contaminations, both targets were cleaned by 20 minutes of pre-sputtering before each deposition process. The target-substrate distance was kept constant at 6.0 cm, and the substrate holder was oscillating in the plasma to improve the film homogeneity. An electric heater and a thermocouple were installed inside the holder and in contact with a copper plate on which 8 rectangular substrates (1.0 x 2.5 cm) were fixed in two parallel lines along the oscillation direction of the holder. ITO films were deposited by maintaining the substrate temperature at 350 ± 10°C, while amorphous TiO_2 films were deposited below 90°C. Anatase TiO_2 thin-films were obtained at a substrate temperature of 350 ± 10°C. The thickness of the films, determined by cross-section SEM analysis, was 350 nm for ITO and 630 nm for TiO_2.

5.2.2 Annealing

The electrodes were annealed in a sealed cylindrical chamber inserted in a tubular furnace. For the annealing in H_2 atmosphere the chamber containing the sample was evacuated up to $1x10^{-3}$ mbar and loaded with hydrogen (99.9%) before the heat treatment. Annealing processes were carried out in different ranges of temperature (250 - 350°C), pressure (1.0 – 5.0 bar) and time (10 minutes – 72 hours).

5.2.3 Characterization

Raman spectra were acquired using a Labram Aramis Jobin Yvon Horiba microRaman system equipped with a 100X objective and He-Ne laser source (632.8 nm). The structural characterization of the deposited samples was carried out by glancing angle X-ray diffraction (XRD) (Rigaku), using Cu Kα radiation (λ = 1.5414 Å). The incident angle was fixed at 1.5 degrees while the 2θ angle was scanned from 10 to 70 degrees. UV-Vis absorption properties were studied using a Varian Cary 5000 spectrophotometer. X-ray photoelectron spectroscopy (XPS) was performed using a Kratos AXIS Ultra^{DLD} instrument equipped with a monochromatic Al Kα (1486.6eV) X-Ray source and a hemispherical analyzer. Electrical charge compensation was required to perform XPS analysis.

Electrochemical and photoelectrochemical measurements were carried out with a Gamry potentiostat/galvanostat/ZRA Interface 1000 using a three-electrodes cell (*figure 5.1*) composed by a Standard Calomel Electrode (SCE, +0.241 V Vs RHE) as reference, Pt-mesh as counter-electrode and 1.0 M KOH solution as electrolyte. The electrochemical cell was inserted

in a ground-connected Faraday-box. Photoelectrochemical measurements were performed using a 250 W OsramXenophot lamp. The emission spectrum of the lamp is peaked in the red, with a very small percentage of UV-contribution. Before proceeding with the photo-electrochemical measurements, the top part of the electrodes was cut and scratched in order to establish the electrical contact with the ITO film. The exposed surface was measured for each electrode, and experimental error was estimated within 30 $\mu A/cm^2$ by considering the oscillation of the current in dark at 0 V Vs. RHE.

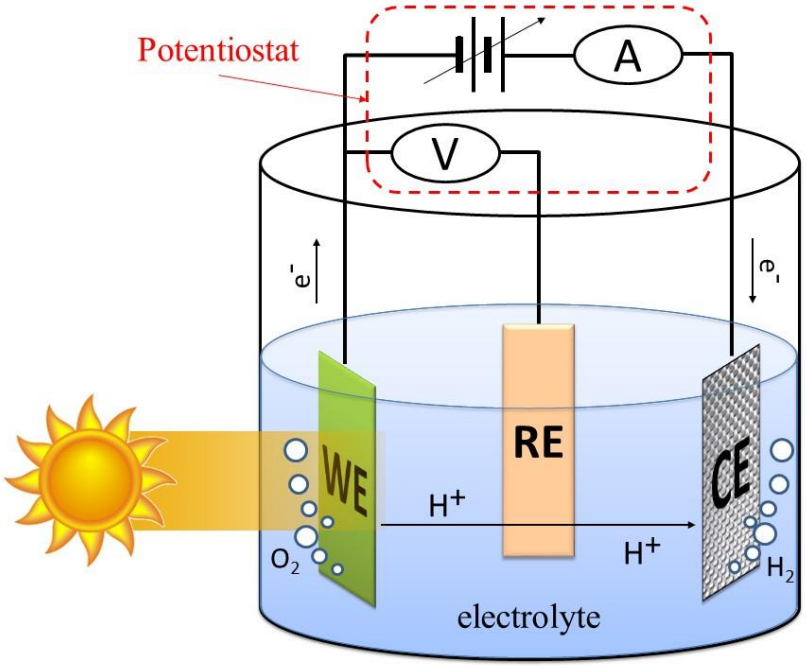

Figure 5.1: Scheme of the cell used for photo-electrochemical measurements.

5.3 Results and discussion

H-doped TiO_2 electrodes were prepared by annealing TiO_2 thin-films in hydrogen atmosphere. Several conditions were tested by varying the temperature (250 - 350°C), the duration (10 minutes – 72 hours) and the atmosphere (air, 1.0 - 5.0 bar of H_2) in order to find out the lowest temperature at which H-doped anatase TiO_2 is obtained. The effect of annealing on the crystalline phase was studied by µ-Raman spectroscopy. Indeed, anatase has five allowed Raman modes (144 cm^{-1} (E_g), 197 cm^{-1} (E_g), 399 cm^{-1} (B_{1g}), 513 cm^{-1} (A_{1g}) and 639 cm^{-1} (E_g)), whereas rutile possesses only three peaks (145 cm^{-1} (A_{1g}), 447 cm^{-1} (E_g) and 612 cm^{-1} (B_{1g})), including two clearly distinguishable modes which make the crystalline phase identification straightforward [11, 12]. As starting electrodes both amorphous and anatase TiO_2 thin-films were used. Annealing at 250°C has no effect on the crystallographic phase of both

amorphous and anatase films, even at high H_2 pressure (5.0 bar) and for long time (up to 72 hours).

Figure 5.2 reports the Raman spectra of amorphous electrodes after a heat treatment of 10 minutes in different conditions of temperature and atmosphere. Annealing at 300°C induces the crystallization of TiO_2 in anatase phase, both in air (*figure 5.2-a*) and in hydrogen (*figure 5.2-b/c*), although a weak rutile formation is evident when annealing in hydrogen atmosphere.

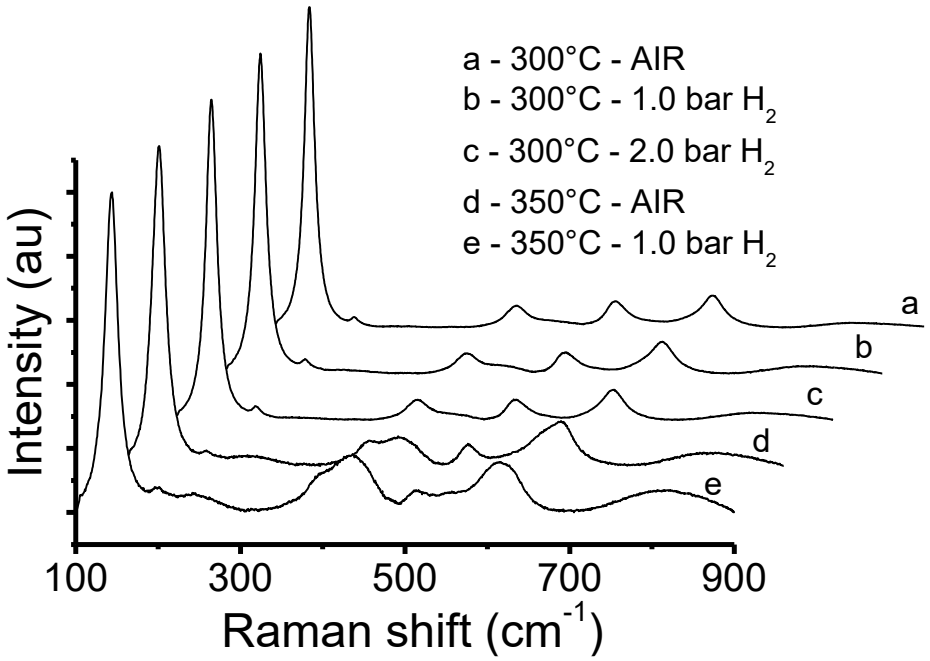

Figure 5.2: Normalized Raman spectra of ITO / amorphous TiO_2 films after annealing for 10 minutes at (a) 300°C in air, (b) 300°C in 1.0 bar H_2, (c) 300°C in 2.0 bar H_2, (d) 350°C in air and (e) 350°c in 1.0 bar H_2.

Longer treatments increase the amount of rutile in the thin films (*figure 5.3*) and the same effect is obtained by increasing the annealing temperature at 350°C, even for short time (*figure 5.2-d/e*). Anatase films, deposited at 350°C, resulted expectedly insensitive to annealing at temperatures lower than the deposition one, requiring higher pressure/temperature conditions for the hydrogenation. Anyway, annealing at 350°C in H_2 pressure higher than 1.0 bar leads to a substantial crystalline phase alteration from anatase to rutile-rich mixtures. Such a reconstruction, from anatase to the more stable rutile, generally occurs at higher temperatures (>350°C) and is dependent on the duration of the treatment [13]. In addition, rutile phase is detected even at a lower temperature (300°C) when hydrogen pressure is increased to 2.0 bar. This trend is in good agreement with pressure-temperature studies of the different polymorphs

of titania performed by Osborn, which reveal an inverse proportionality between pressure and temperature at which the phase transition takes place [14].

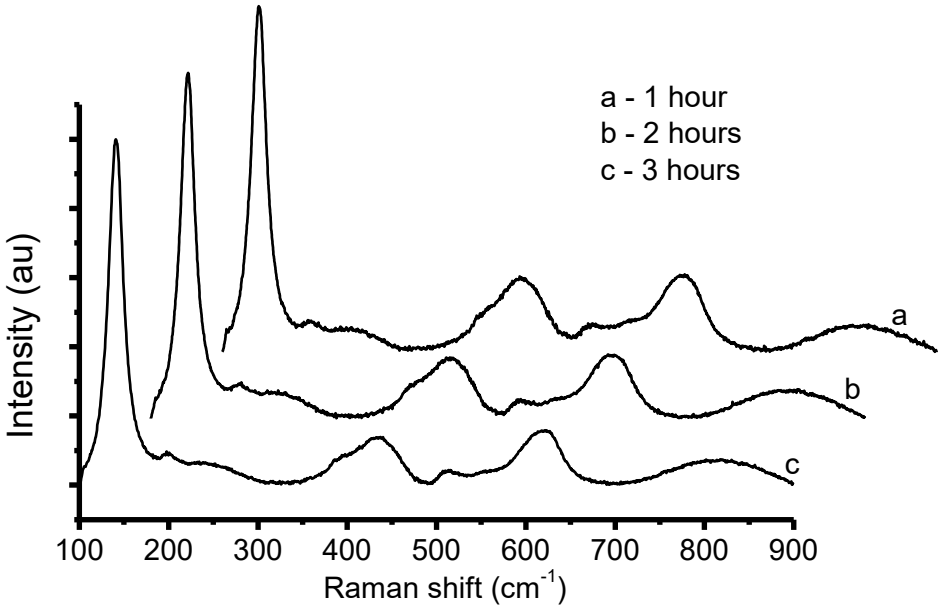

Figure 5.3: Normalized Raman spectra of ITO / amorphous TiO_2 films after annealing at 300°C in 1.0 bar H_2 for 1 hour (a), 2 hours (b) and 3 hours (c).

Annealing atmosphere	**Annealing temperature**		
	250 °C	300 °C	350 °C
AIR	Amorphous	Anatase	anatase + rutile
1.0 bar H_2	Amorphous	H-anatase	H-anatase + rutile
2.0 bar H_2	Amorphous	H-anatase + rutile	H-anatase + rutile

Table 5.1: Summary of the annealing effects on amorphous TiO_2.

Annealing atmosphere	**Annealing temperature**		
	250 °C	300 °C	350 °C
AIR	Anatase	Anatase	anatase + rutile
1.0 bar H_2	Anatase	Anatase	H-anatase + rutile
2.0 bar H_2	Anatase	anatase + rutile	H-anatase + rutile

Table 5.2: Summary of the annealing effects on anatase TiO_2.

The crystalline phase modifications induced by the annealing in different conditions are summarized in *table 5.1* for amorphous and in *table 5.2* for anatase TiO_2. Anatase thin-films, possessing elevated stability, cannot be hydrogenated in mild conditions, and extreme conditions lead to rutile formation. Contrariwise, amorphous TiO_2 can be transformed into

anatase even by a mild annealing at 300°C, and the presence of highly reactive hydrogen atmosphere induces the formation of H:TiO_2.

Taking into consideration the results of Raman characterization and being interested in anatase TiO_2, because it is the most active polymorph for photocatalysis [15], the subsequent discussion is focused only on anatase TiO_2 and H:TiO_2, aimed to investigate the effect of H-doping in anatase TiO_2. Henceforth, TiO_2 indicates the samples deposited at 350 °C and H:TiO_2 stands for H-doped anatase achieved by annealing amorphous TiO_2 at 300°C in 1.0 bar of H_2 for 10 minutes.

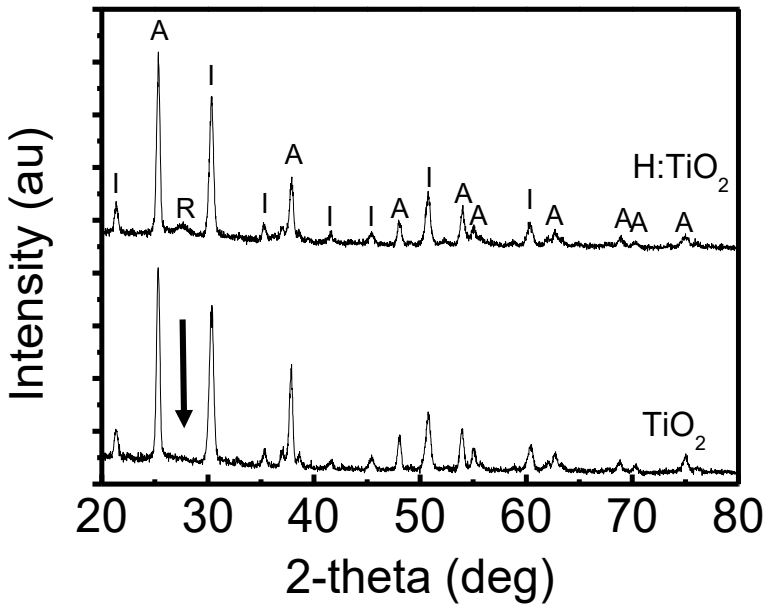

Figure 5.4: XRD patterns of TiO_2 and H:TiO_2 ("I" indicates ITO, "A" indicates Anatase and "R" Rutile).

Figure 5.4 reports the comparison of XRD patterns acquired on TiO_2 and H:TiO_2 annealed at 300°C for 10 minutes in air and in 1.0 bar of H_2, respectively. The XRD patterns show peaks of ITO (labelled "I") and TiO_2 (labeled "A" for anatase and "R" for rutile crystalline phase). The results show that annealing in air produces merely anatase phase, whereas for samples annealed in presence of hydrogen the main peak of rutile (110) is weakly distinguishable at 2-theta = 27.46°, confirming the formation of a small amount of rutile phase. XRD analysis confirms both the crystallization of TiO_2 in anatase in mild annealing conditions (300°C for 10 minutes) and the formation of a small percentage of rutile in presence of H_2 atmosphere, as evidenced in the Raman spectra.

In order to have a deeper insight on the effect of H incorporation in the TiO_2 lattice, XPS analysis was carried out on both TiO_2 and H:TiO_2. High-resolution Ti2p and O1s XPS spectra of TiO_2 and H:TiO_2 are reported in *figure 5.5*.

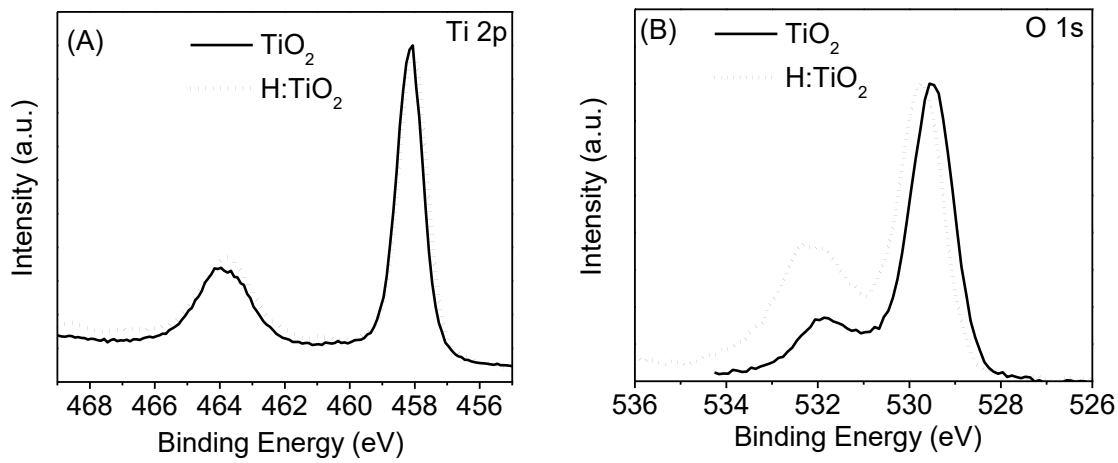

Figure 5.5: Normalized high-resolution Ti 2p (A) and O 1s (B) XPS spectra of TiO_2 (black-solid line) and H:TiO_2 (gray-dotted line).

The peaks at binding energy (BE) 458.4 eV and 464.2 eV, assigned to $Ti2p_{3/2}$ and $Ti2p_{1/2}$ of Ti^{4+} species, are clearly observed for both TiO_2 and H:TiO_2 (*figure 5.5-A*). Such peaks are consistent with typical values for TiO_2 [16, 17], and no shift in these peaks was detected after H-doping. No signal assigned to Ti^{3+} species is observed suggesting that H is not reducing Ti^{4+} to Ti^{3+} species. The two peaks detected in O1s high-resolution XPS spectra can be ascribed to the bonds of oxygen with Ti and H, respectively at lower and higher BE [2, 18]. The peak at lower BE (529.9 eV) is assigned to Ti-O which is shifted at higher BE in H:TiO_2, as compared to TiO_2 (529.7 eV). In addition, the peak at higher BE (531.8 eV) is more intense in H:TiO_2, and presents an additional shoulder at BE 532.3 eV. Such peaks are compatible with the formation of Ti-OH, which are usually located at higher BE [2], confirming that H is effectively doped into the lattice.

Spectroscopic characterization was performed in order to elucidate the different light absorption induced by the annealing in hydrogen atmosphere. *Figure 5.6* reports the absorption spectra of ITO/TiO_2 and ITO/H:TiO_2 thin-films. Both the spectra present a strong absorption in the UV region, followed by a transparent window covering the visible spectral region. The absorption in the UV region can be ascribed to the band-edge absorption of the anatase (E_g = 3.2 eV), which hides the ITO absorption [19]. The magnified image (inset of *figure 5.6*) shows that the absorption band-edge of H:TiO_2 is slightly shifted towards lower energy. Such shift can be considered negligible in terms of optical properties, even if it can be compatible with a slight band gap reduction induced by the presence of hydrogen atoms in the lattice. These results are in good agreement with density functional theory (DFT) calculations reported in literature [20], showing that H incorporation in TiO_2 matrix results in a very small band gap narrowing.

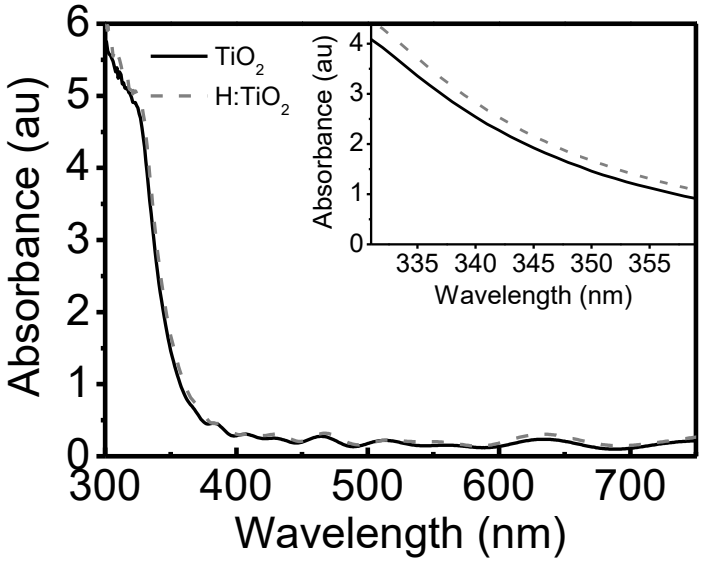

Figure 5.6: Absorption spectra of TiO_2 (solid-black line) and H:TiO_2 (dashed-gray line) thin films. In the inset is reported the magnification of the absorption spectra.

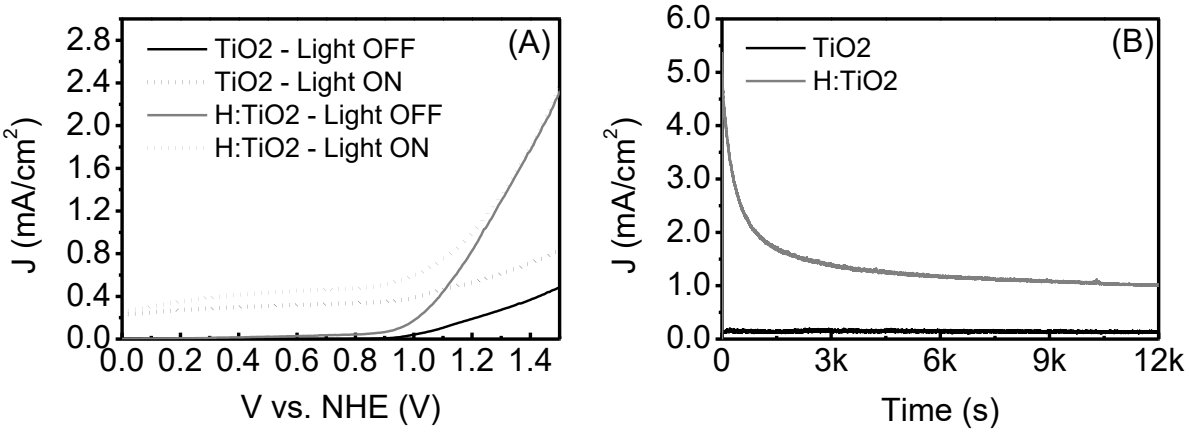

Figure 5.7: (A) Linear-Sweep Voltammetry and (B) Chrono-Amperometry at 1.23 Vs RHE of TiO_2 (black) and H:TiO_2 (gray), in dark (solid lines) and under illumination (dotted lines).

The photocatalytic activity of the samples was investigated by monitoring the oxygen evolution reaction (OER) in photoelectrochemical experiments. *Figure 5.7-A* reports the linear sweep voltammetry (LSV) of TiO_2 (black) and H:TiO_2 (gray), in dark (solid lines) and under illumination (dotted lines). The large overpotential of TiO_2 for OER, limiting the performance of TiO_2 in PEC, diminished from 1.02 V to 0.85 V for H:TiO_2, where the overpotentials are compared in a specific current density of 50 μA/cm^2. As a consequence, the current density measured for H:TiO_2 is 0.99 mA/cm^2 at 1.23 V, about 10 times higher than 0.10 mA/cm^2 measured for TiO_2. In addition, the photocurrent density measured at 0.70 V resulted improved in the case of H:TiO_2 (0.23 mA/cm^2), about 45% higher than that of TiO_2 (0.17 mA/cm^2). The

stability of the samples has been tested at 1.23 V vs. RHE under illumination over 3 hours (*figure 5.7-B*). The current density of H:TiO_2 at the beginning is extremely high, but it stabilizes at 0.99 mA/cm^2, while the photocurrent density of TiO_2 electrodes remains stable at 0.10 mA/cm^2. The enhanced catalytic activity exhibited in H:TiO_2 can be correlated to the ability of H atoms to passivate dangling bonds, reducing the density of trap-states which facilitate the electron-hole recombination [4-6].

5.4 Conclusion

The use of TiO_2 as photocatalyst for solar hydrogen generation is mainly limited by its intrinsic low light absorption and fast recombination of photogenerated carriers. Here, a successful method was developed for converting amorphous TiO_2, generally easy to synthesize, into H-doped anatase TiO_2 by a mild annealing in hydrogen atmosphere. Amorphous TiO_2 electrodes were deposited on ITO thin-film by RF-magnetron sputtering and tested in several annealing conditions of temperature, time and atmosphere. H:TiO_2 electrodes were obtained by a rapid annealing at 300°C in 1.0 bar of H_2 atmosphere and resulted mainly in anatase crystalline phase. XPS analysis revealed that H atoms lead to the formation of hydroxyl groups, passivating dangling bonds, which are predominant in disordered-amorphous TiO_2. As a result, H-doped TiO_2 electrodes presented an enhanced photocatalytic activity with respect to anatase TiO_2 thin-films obtained by annealing in air, showing a current density of 0.99 mA/cm^2 at 1.23 V vs. RHE. Since H-doping did not improve the light absorption, as revealed by UV-vis absorption measurements, the enhanced photo-catalytic activity was ascribed to the dangling bonds passivation made by H atoms, which reduces the density of recombination centers. The reported approach can be extended to the preparation of efficient H-doped anatase TiO_2 electrodes starting from any amorphous TiO_2, with expected enhanced activity in PEC.

5.5 References

1. Liu, L. and X. Chen, *Titanium Dioxide Nanomaterials: Self-Structural Modifications.* Chemical Reviews, 2014. **114**(19): p. 9890-9918.
2. Wang, G., et al., *Hydrogen-Treated TiO_2 Nanowire Arrays for Photoelectrochemical Water Splitting.* Nano Letters, 2011. **11**(7): p. 3026-3033.
3. Sun, C., et al., *Hydrogen Incorporation and Storage in Well-Defined Nanocrystals of Anatase Titanium Dioxide.* Journal of Physical Chemistry C, 2011. **115**(51): p. 25590-25594.
4. Liu, L., et al., *Hydrogenation and Disorder in Engineered Black TiO_2.* Physical Review Letters, 2013. **111**(6).
5. Chen, X., et al., *Increasing Solar Absorption for Photocatalysis with Black Hydrogenated Titanium Dioxide Nanocrystals.* Science, 2011. **331**(6018): p. 746-750.
6. Pesci, F.M., et al., *Efficient Suppression of Electron Hole Recombination in Oxygen-Deficient Hydrogen-Treated TiO_2 Nanowires for Photoelectrochemical Water Splitting.* Journal of Physical Chemistry C, 2013. **117**(48): p. 25837-25844.
7. Wang, Z., et al., *H-Doped Black Titania with Very High Solar Absorption and Excellent Photocatalysis Enhanced by Localized Surface Plasmon Resonance.* Advanced Functional Materials, 2013. **23**(43): p. 5444-5450.
8. Yu, X., B. Kim, and Y.K. Kim, *Highly Enhanced Photoactivity of Anatase TiO_2 Nanocrystals by Controlled Hydrogenation-Induced Surface Defects.* ACS Catalysis, 2013. **3**(11): p. 2479-2486.
9. Zhang, Z., et al., *Electrochemical reduction induced self-doping of Ti^{3+} for efficient water splitting performance on TiO_2 based photoelectrodes.* Physical Chemistry Chemical Physics, 2013. **15**(37): p. 15637-15644.
10. Rahman, M., J.M.D. MacElroy, and D.P. Dowling, *Influence of the Physical, Structural and Chemical Properties on the Photoresponse Property of Magnetron Sputtered TiO_2 for the Application of Water Splitting.* Journal of Nanoscience and Nanotechnology, 2011. **11**(10): p. 8642-8651.
11. Ohsaka, T., *Temperature dependence of the Raman spectrum in Anatase TiO_2.* Journal of the Physical Society of Japan, 1980. **48**(5): p. 1661-1668.

12. Binetti, E., et al., *Synthesis of mesoporous ITO/TiO_2 electrodes for optoelectronics.* Materials Letters, 2015. **139**: p. 355-358.
13. Hanaor, D.A.H. and C.C. Sorrell, *Review of the anatase to rutile phase transformation.* Journal of Materials Science, 2011. **46**(4): p. 855-874.
14. OSBORN, E.F., *Subsolidus Reactions in Oxide Systems in the Presence of Water at High Pressures.* Journal of the American Ceramic Society, 1953. **36**(5): p. 5.
15. Froeschl, T., et al., *High surface area crystalline titanium dioxide: potential and limits in electrochemical energy storage and catalysis.* Chemical Society Reviews, 2012. **41**(15): p. 5313-5360.
16. Tomaszek, R., et al., *Microstructural characterization of plasma sprayed TiO_2 functional coating with gradient of crystal grain size.* Surface & Coatings Technology, 2006. **201**(1-2): p. 45-56.
17. Wang, J., et al., *N-doped TiO_2/C nanocomposites and N-doped TiO_2 synthesised at different thermal treatment temperatures with the same hydrothermal precursor.* Dalton Transactions, 2014. **43**(36): p. 13783-13791.
18. Llobet, E., et al., *Carbon nanotube-TiO_2 hybrid films for detecting traces of O_2.* Nanotechnology, 2008. **19**(37).
19. Binetti, E., et al., *Interaction of TiO_2 Nanocrystals with Imidazolium-Based Ionic Liquids.* Journal of Physical Chemistry C, 2013. **117**(25): p. 12923-12929.
20. Binetti, E., et al., *Rapid hydrogenation of amorphous TiO_2 to produce efficient H-doped anatase for photocatalytic water splitting.* Applied Catalysis A: General, 2015. **500**: p. 69-73.

Chapter 6

On the effect of Cu and N codoping on RF-sputtered TiO_2 photo-catalyst films[1]

In chapter 3 we studied V and N codoped TiO_2, which is an n-p compensated codoping. This chapter deals with non-compensated n-p codoping of TiO_2, which was reported to have a greater effect on the optical properties and photo-catalytic activity of TiO_2.

6.1 Introduction

Zhu et al. [1], described a new concept of non-compensated *n–p* co-doping of TiO_2 generating an intermediate band (IB) in the mid gap of the matrix. This method increases both the thermodynamic stability and the kinetics of charge carriers. Cr and N co-doping was presented as a model for non-compensated *n-p* co-doping, showing enhanced visible light absorption and charge separation. However, localized *d*-states of Cr below the CBM make this material a bad candidate for hydrogen reduction in the water splitting process, since the conduction band level becomes higher than the water reduction potential. Therefore, Dashora et al. [2] looked for a new dopant element pair, which does not form impurity states near the CBM and, at the same time, generates a band in the middle of TiO_2 band gap. First principles calculations on the electronic and optical properties of Cu and N co-doped TiO_2 revealed the presence of an isolated intermediate band deeply located in the band gap due to strong hybridization between Cu *3d* and N *2p* orbitals. This intermediate band has the property to

[1] Z. El Koura, M. Cazzanelli, N. Bazzanella, N. Patel, R. Fernandes, G. E. Arnaoutakis, A. Gakamsky, A. Dick, A. Quaranta, and A. Miotello. *Manuscript in preparation*.

enhance the visible light absorption of TiO_2. At the same time, Cu and N co-doping only causes a small shift of the conduction band, preserving the ability of TiO_2 to drive the water reduction reaction.

The enhancement of the photocatalytic activity of TiO_2 sol-gel thin films by Cu and N co-doping was confirmed by experiments on degradation of organic pollutants [3-5]. However, these experiments did not give information on the involved mechanism and, as for our knowledge, nothing was reported on the effect of co-doping on the photo-electrochemical water-splitting reactions. Moreover, an effort to correlate the optical features (like absorption, photoluminescence and photoluminescence lifetimes) of this important photocatalytic material, with its crystalline structure and with the interaction of the photo-generated carriers with the defects and the modified TiO_2 band-structure is still lacking.

In this work we study the structural, morphological and optical properties of sputtered TiO_2 thin films doped with Cu and/or N at different concentrations. The samples were then tested as photoelectrodes in photoelectrochemical water splitting experiments. We observed an enhancement of the reduction reaction and a concomitant weakening of the oxidation reaction suggesting a possible explanation.

6.2 Experimental

Pure, Copper and Nitrogen mono- and co-doped TiO_2 samples were deposited by radio frequency (RF) magnetron sputtering starting from a ceramic TiO_2 target (purity 99.99%). The working gas was Argon (purity 99.9%) and 150 W of RF-power was employed. Copper doping was obtained by placing metal copper pieces (purity 99.99%) over the TiO_2 target, and nitrogen doping by inletting a controlled flux of nitrogen gas into the deposition chamber. Co-doping was obtained by combining the two strategies. Before the deposition, a base pressure of 10^{-7} mbar was achieved, then Argon gas was introduced into the deposition chamber by a mass-flow controller such that a constant pressure of 8×10^{-3} mbar of Argon was maintained. The target-substrate distance was fixed at 6.0 cm, and the substrate holder was kept oscillating in the plasma to improve the homogeneity of the deposited films. The substrate temperature was raised up to 350 °C before the deposition and maintained constant (± 2 °C) throughout the deposition process. Before each deposition, the targets were pre-sputtered for 20 minutes to remove all possible contaminants from their surface. Samples with different dopants concentrations were obtained by fixing a number of Cu pieces (0, 2, 3, 4, and 5) on the target

and by varying the nitrogen flux to 0, 10, 20, and 30 sccm (the Argon flux was 20 sccm for all the depositions). 20 thick samples (ca. 800 nm) with different N and/or Cu concentrations were deposited on silicon (100) and quartz, to study the morphological, structural and optical properties of the films. The samples were designated as XYY, where X reports the number of copper pieces used during the deposition, while YY reports the flux (in sccm) of nitrogen in the chamber. For example the sample 310 was deposited by placing 3 pieces of copper on the TiO_2 target and fluxing 10 sccm of nitrogen during the whole deposition process. Thin films (ca. 300 nm) were deposited on soda-lime glass coated with indium tin oxide (ITO) to perform photocatalytic measurements. In this case, ITO (ca. 100 nm) was sputtered, before depositing TiO_2, using a ceramic ITO target (purity 99.99%), an Argon gas pressure of 8×10^{-3} mbar and 100 W RF power. All the other parameters were the same as for TiO_2 deposition.

Structural characterization of the samples was carried out by Raman spectroscopy, using a LabRam Aramis Jobin-Yvon Horiba microRaman system equipped with a 100X objective and He-Ne laser source (632.8 nm). Scanning Electron Microscopy (SEM) was used to analyse the morphology and the thickness of the films. The surface of the films was analysed by a JEOL JSM-7001F field effect gun (FEG-SEM) apparatus at 20 keV beam energy. SEM apparatus is equipped with an Energy Dispersive X-ray Spectroscopy detector (EDXS, Oxford INCA PentaFETx3), that was used to estimate the concentration of copper. X-ray Photoelectron Spectroscopy (XPS) was performed to examine the surface composition and chemical states of the samples using a "PHI 5000 VersaProbe II" instrument equipped with a mono-chromatic Al Kα (1486.6 eV) X-ray source and a hemispherical analyser. Appropriate electrical charge compensation was employed to perform the analysis. The binding energy was referenced to the C1s peak at 284.8 eV.

Absorption spectra were measured with a Cary5000 spectrophotometer having a resolution of 0.4 nm and an integration time of 0.1 sec per point. Specular Reflectance was measured with a Jasco V-570 spectrophotometer at near normal (≈8°) incidence with a spectral resolution of 1 nm. Photoluminescence (PL) measurements were performed using the third-harmonic output (355 nm) of a Nd:YAG laser operating at a repetition rate of 3 KHz and having a pulse duration nominally equal to 5 ns. The spectrum was recorded with a thermoelectrically-cooled Ocean Optics FL-Q65000 fiber-pigtailed Spectrometer. Integration time was chosen equal to 5 sec per spectrum. The scattered laser light was filtered with a Semrock edge filter mod. BLP01-364R-25. Time-resolved emission measurements were performed with a spectrometer (Edinburgh Instruments, FLS980) equipped with two monochromators and a photomultiplier tube (PMT)

detector (Hamamatsu, R928P). The samples were excited at 355 nm by the 3rd harmonic of a Q-switched Nd:YAG pulsed laser (Continuum, Minilite) coupled with the fluorescence spectrometer. To minimise scattered excitation light, the samples were tilted at 45° in respect to the excitation, while a 395 nm long wave-pass filter was additionally used in the emission arm. The time-resolved emission spectra were obtained in the instrument's F980 software by data slicing the emission maps at 6 bins between 32-42 μs. Time decay curves were extracted by selecting a fixed wavelength from the PL maps.

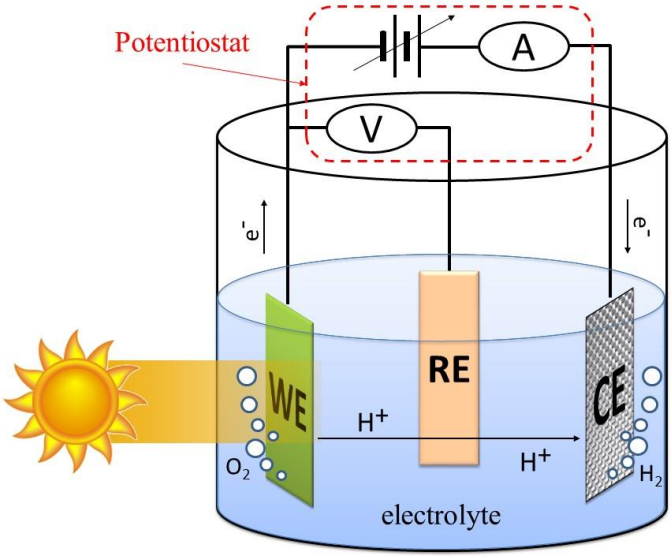

Figure 6.1: Scheme of the photo-electrochemical cell used in this work.

Electrochemical and photoelectrochemical measurements were carried out with a Gamry potentiostat/galvanostat/ZRA Interface 1000 using a three-electrodes cell (*figure 6.1*) composed by a Standard Calomel Electrode (SCE, +0.241 V vs RHE) as reference, Pt-mesh as counter-electrode and TiO_2 samples as working electrodes. The electrochemical cell was inserted in a ground-connected Faraday-box. A 250 W Osram Xenon lamp was used as light source and KOH 1 M as electrolyte (pH = 14). At this pH value, hydrogen evolution is expected at -0.826 V vs. RHE and oxygen evolution at 0.404 V vs. RHE. Before proceeding with photo-electrochemical measurements, the top part of the electrodes was cut and coated with silver paint in order to ensure a good electrical contact with ITO. The exposed surface was set to 1.0 cm^2. For each sample, a first linear sweep voltammetry (LSV) was followed by a cyclic voltammetry (CV) to clean catalyst's surface from possible residual contaminants. Then the measurements were performed by taking two LSVs: the first under dark conditions and the

second under illumination. All the LSV and CV curves were performed at a scan rate of 100 mV/s, step size of 10 mV and equilibration time of 5 s.

6.3 Results and Discussion

6.3.1 Raman characterization

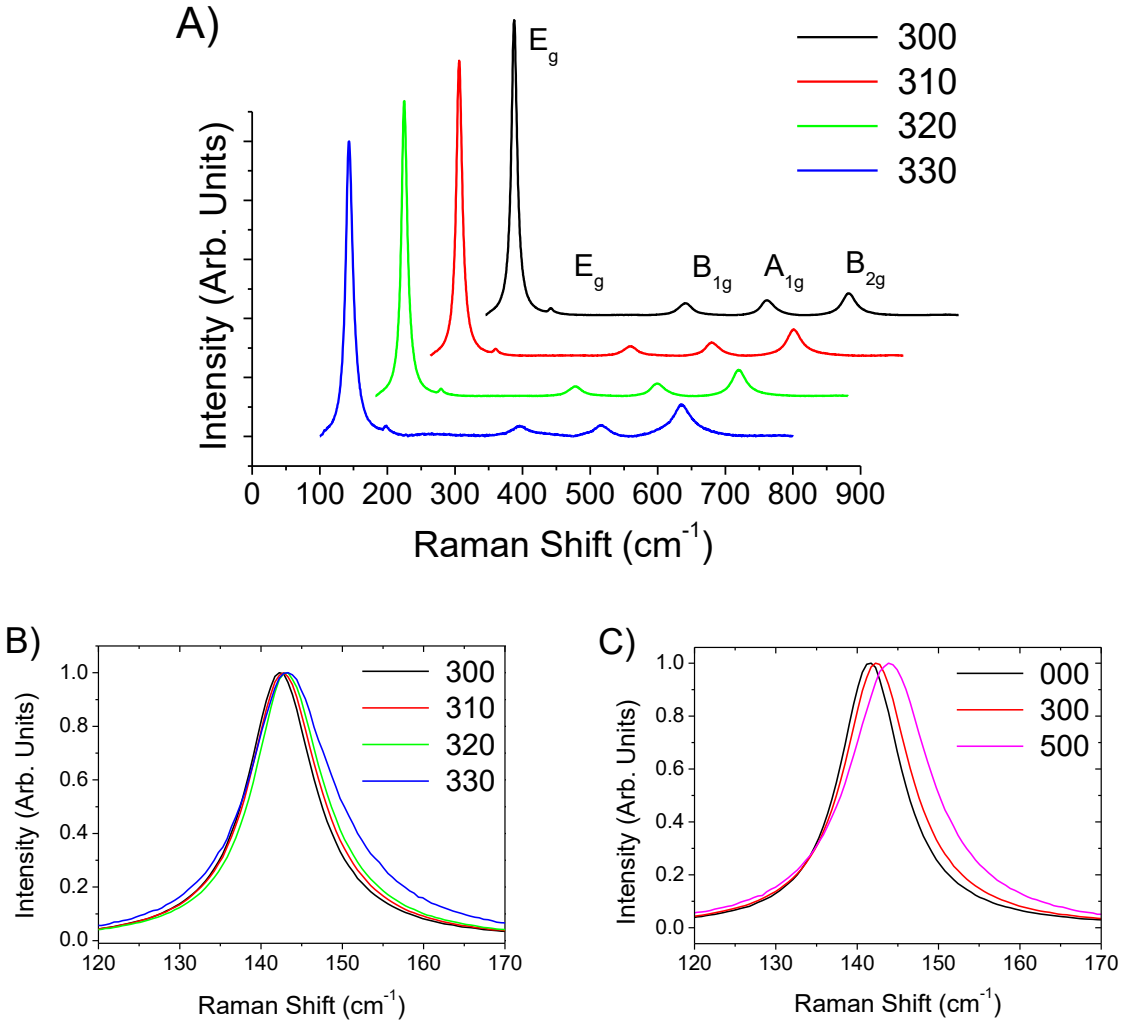

Figure 6.2: A) Normalized Raman spectra of TiO_2 films doped with Cu and N using 3 copper pieces and different nitrogen fluxes (0, 10, 20 and 30 sccm). B) Magnification showing the shift of the main peak of Anatase TiO_2 (E_g at 144 cm^{-1}) towards higher wavenumbers due to Cu and N co-doping. C) Effect of Cu doping on the position of the main peak of Anatase TiO_2.

Raman spectra of all the samples, shown in *figure 6.2-A*, present five characteristic peaks, at 144 cm^{-1}, 197 cm^{-1}, 399 cm^{-1}, 513 cm^{-1} and 639 cm^{-1}, which are the fingerprint of Anatase TiO_2 and are attributed to the E_g, E_g, B_{1g}, A_{1g}, and B_{2g} modes, respectively [6]. This indicates that thin films grow with the Anatase phase even in doped samples. Moreover, the presence of sharp peaks indicates a good crystalline quality. *Figures 6.2-B and -C* show the normalized Anatase

main peak for samples with different concentration of N and Cu, respectively. As can be observed, the peak broadens and shifts to higher wavenumbers as the dopant concentration increases. This behaviour can be ascribed either to the lowering of the crystallite size, thus affecting the force constants and the vibrational amplitudes of the nearest neighbour bonds [7], or to internal strain fields induced by the dopants and affecting the Raman peak positions [8].

6.3.2 SEM and EDXS characterization

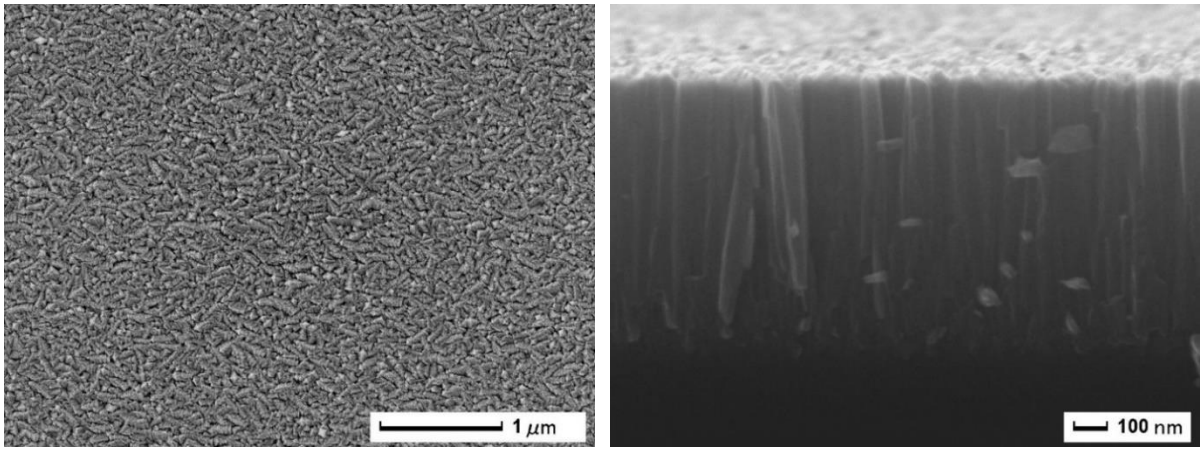

Figure 6.3: SEM micrographs of the sample 310 in a top-view (left) and cross section configuration (right), representative of the whole set of samples morphology. The scale is reported in the figures.

Figure 6.3 shows, on the left panel, the surface morphology of the sample named 310 and, on the right panel, the cross-sectional SEM image of the same sample, where the film exhibits a nanometric columnar structure with a width lower than 50 nm. This morphology was detected for all the films regardless to the dopant types and concentrations.

Figure 6.4 reports the results of EDXS/SEM characterization. The thickness of the films was measured from cross-sectional SEM images. Films deposited with the same number of Cu pieces but with different nitrogen fluxes present a lowering of thickness as the nitrogen flux is increased. This is expected since the presence of nitrogen changes both the gas pressure and the sputtering rate of the process. In fact, the plasma energy is dissipated in ionizing and accelerating Ar atoms, on one hand, and in dissociating N_2 molecules on the other hand [9]. Thus, as the N_2 ratio is increased in the carrier gas, an increasing part of the plasma energy available serves to dissociate N_2 molecules, leaving thereby less energy to produce Ar ions, which in turn, translates into less efficient sputtering process.

Cu concentration, measured by EDXS, is around 1 at.% with 2 metal fragments and increases with the number of Cu pieces reaching 2.3 at.% in sample 400 and 6.8 at.% in 500. Concentrations were measured with an approximation of 0.4 at.%. As can be clearly seen from *figure 6.4*, fixed the number of fragments, Cu concentration decreases when N is inserted. The highest variation was detected in the set with 5 copper pieces where Cu concentration goes from 6.8 at.% (sample 500) to 4.6 at.% (sample 530). Nitrogen concentration could not be measured by EDXS. Indeed, nitrogen has only a weak peak centred at 392 eV, due to $K_{\alpha_{1,2}}$ lines. Near this energy, Ti has three peaks ($L_l = 395$ eV, $L_\alpha = 452$ eV, $L_{\beta_1} = 458$ eV) which are much more intense and hide the N characteristic feature. Moreover, since the resolution of the detector in this energy range is 65 eV, the fine structure of the peaks and the N peak cannot be resolved. For this reason, EDXS is not suitable for N concentration measurements.

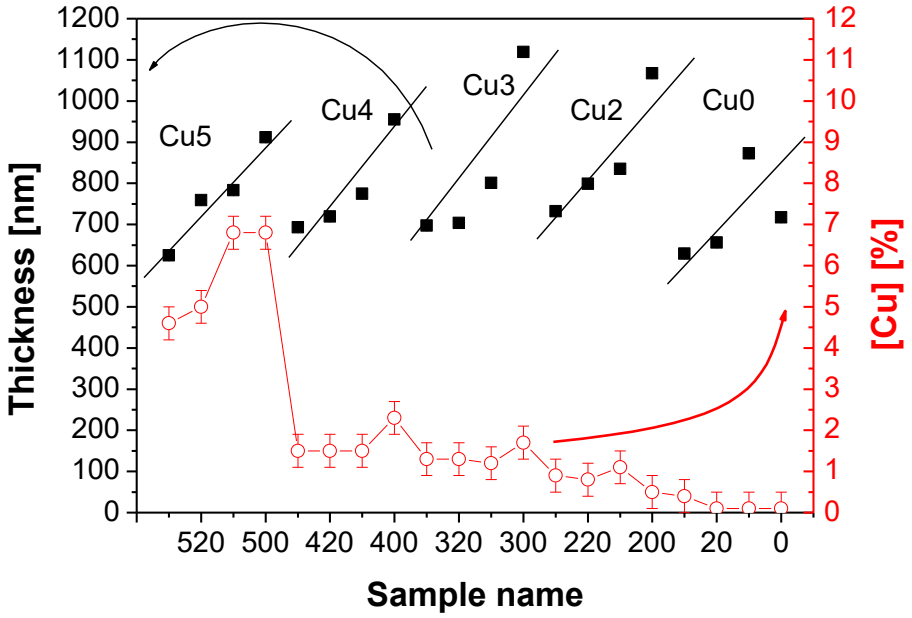

Figure 6.4: Left (black) axis refers to the thickness (± 30 nm) of the samples whose label is reported on the X-axis. Right (red) axis reports the copper concentration (± 0.4 at.%) as estimated from EDXS. All the films were deposited by keeping constant the deposition time.

6.3.3 XPS characterization

The chemical states of the elements on the surface of the samples were examined by x-ray photoelectron spectroscopy (XPS). Pure TiO_2 film display two peaks centred at 458.5 eV and 464.2 eV assigned to Ti $2p_{3/2}$ and Ti $2p_{1/2}$ core levels of Ti^{4+}, respectively. These two peaks shift positively by 0.2 eV with Cu or/and N doping, thus indicating a variation of Ti^{4+} chemical environment in the matrix due to the incorporation doping species. The O *1s* core level of all

samples present a broad peak that can be de-convoluted into two peaks: a small peak centred at 531.4 eV, attributed to O-H bond, and the main peak centred at 529.7 eV (for pure TiO_2), related to the O-Ti bond inside TiO_2. This peak shifts by 0.2 eV in Cu/N doped and co-doped samples. Samples doped with nitrogen present a small peak at 457.5 eV, which is related to Ti^{3+}, indicating oxygen vacancies created by N doping.

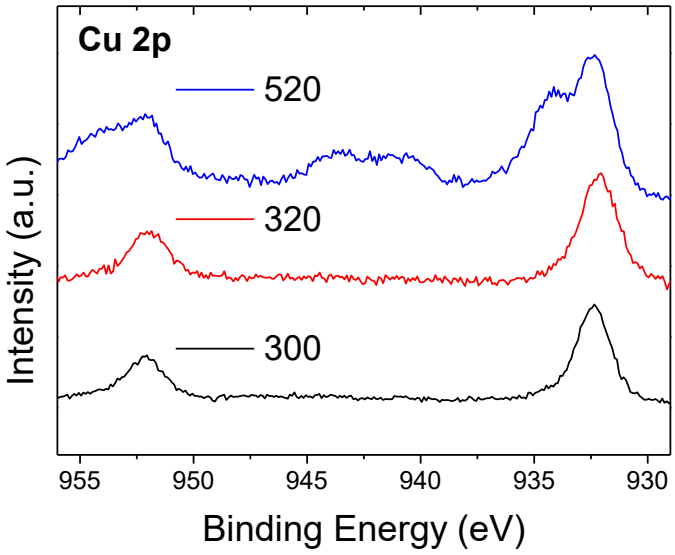

Figure 6.5: XPS spectra of Cu 2p core levels of samples 300, 320 and 520.

Samples with low Cu concentration (ca. 2 at.%) show two peaks centred at 932.3 eV and 952.0 eV (*figure 6.5*), which are attributed to Cu $2p_{3/2}$ and Cu $2p_{1/2}$ core levels, respectively, in Cu_2O (Cu^{1+}) [10, 11]. N incorporation does not alter Cu XPS features, as can be inferred comparing 300 and 320 curves in *figure 6.5*. Both signals show a faint contribution at higher energies (934.2 and 954.3 eV), which become very intense in films with higher Cu content (about 5 at.%), as can be observed in the spectrum corresponding to sample 520. The peak at 934.2 eV is attributed to Cu $2p_{3/2}$ and the one at 954.3 eV to Cu $2p_{1/2}$ in CuO (Cu^{2+}) [11]. In addition, Cu^{2+} has three Cu $2p_{3/2}$ satellite peaks at 941.9, 943.0, and 944.8 eV [12], giving rise to the broad feature between 940.0 and 945.0 eV. This analysis evidences that at low concentrations copper is present mainly as Cu^{1+} and that the amount of Cu^{2+} species increases as the concentration is increased. In particular, by means of convolution analyses we evaluated a distribution of 94% for Cu^{1+} and 6% for Cu^{2+} in sample 300 while in sample 520 the two values are 32% and 51%, respectively.

Figure 6.6 shows the XPS spectra of N 1s core levels of some samples. A different nature of nitrogen doping was found for different nitrogen contents. At low nitrogen concentrations,

only one peak is observed, at B.E. ~ 399.8 eV (*figure 6.6* - sample 010). This peak can be assigned to N substitutionally replacing oxygen to form O-Ti-N linkage. With increasing the nitrogen doping, a second peak at 396 eV is observed (*figure 6.6* - sample 020). This binding energy is close to Ti-N-Ti bond and can be attributed to N ions that substitute oxygen ions in the TiO_2 lattice. With further increasing the N content (*figure 6.6* - sample 030), a third peak arises at 402 eV, due to interstitial occupation of N and oxidized N species (NO) to form Ti-O-N and Ti-O-N-O linkages. These three peaks of nitrogen are present in all co-doped samples, suggesting that Nitrogen is present both as interstitial and substitutional dopant (*figure 6.6* - sample 520) [13].

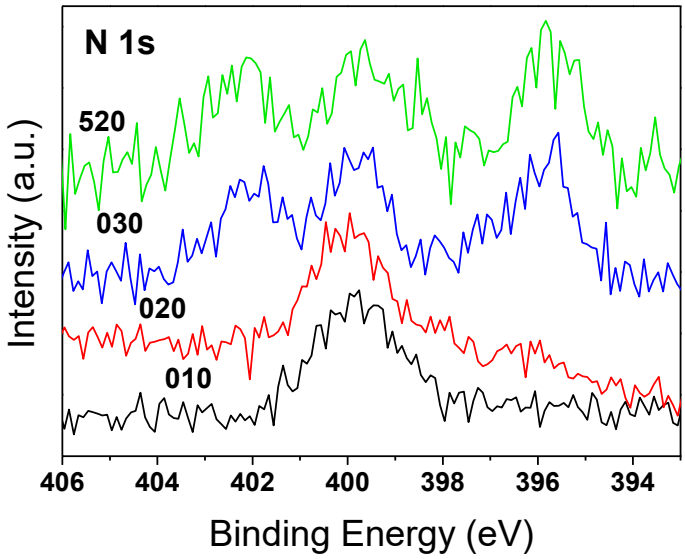

Figure 6.6: XPS spectra of N 1s core levels of samples 010, 020, 030, and 520.

XPS analysis was used also to quantify the concentration of the dopants. Copper concentrations obtained by XPS are in good agreement with those given by EDXS analysis. In addition, XPS allowed the quantification of the nitrogen concentration in the samples. The nitrogen content increases with the nitrogen flux, giving 0.7±0.4 N at.% for 10 sccm, 1.1±0.4 N at.% for 20 sccm, and 1.3±0.4 N at.% for 30 sccm. It is known that the nitrogen incorporation efficiency depends on the flow rate ratio of Ar and nitrogen. Three N incorporation regimes were reported in literature [9]. For very low N_2/Ar flux ratios, the amount of nitrogen in the plasma is low and as a consequence also the number of dissociated N atoms. As the nitrogen flux is increased, more and more molecules become available, and the probability of N_2 ionization increases. In this case a strong dependence of the nitrogen concentration from N_2/Ar ratio was observed. In general, if the ratio is furtherly increased a saturation regime is observed, since the increment of N_2 flux decreases the deposition rate but does not change significantly

the incorporation rate of N. We are very near to the saturation regime, as confirmed by the weak dependence of the nitrogen content in the films on the nitrogen flux variation and by the decrement of the films thickness discussed in the previous section.

6.3.4 Optical characterization

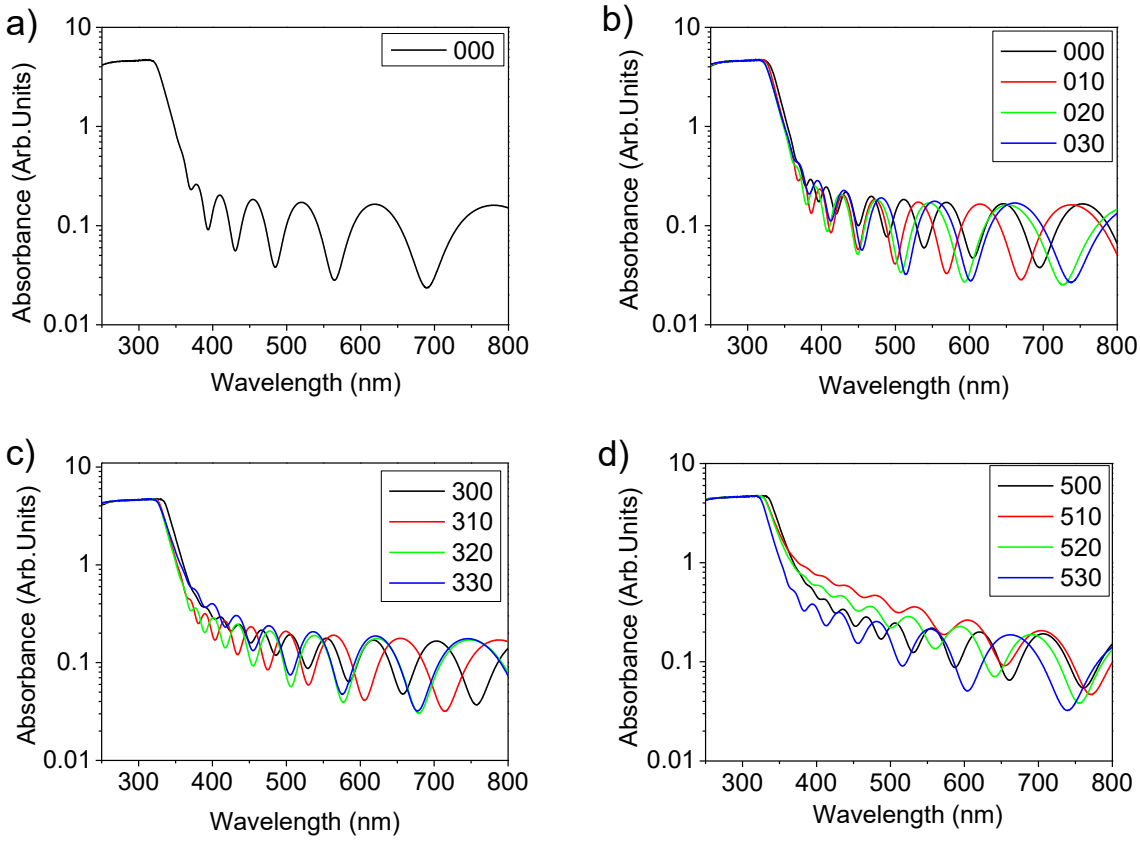

Figure 6.7: Absorbance spectra of pure TiO_2 (a) and three different sets of samples (b-d).

Figure 6.7 shows the optical absorbance spectra of pure TiO_2 and of samples doped with different concentrations of Cu and N. As can be observed, the films are transparent, exhibiting fringes related to multiple interface reflections. At high copper concentrations (*figure 6.7-d*), the sample absorbs in the visible region between 400 and 600 nm, as evidenced by the fringes damping. When the copper dopant is concentrated enough, the nitrogen content affects significantly the optical properties of TiO_2 films. The film absorbing more in the visible region is 510, which is codoped with Cu and N, 5 at.% and 1 at.%, respectively. This effect could be related to the co-doping of copper and nitrogen, which in turn affects the bandgap region in such a way that a relatively wide defect-related visible absorption appears where usually TiO_2 is optically transparent [5].

Figure 6.8 shows the PL spectra of four different sets. In each set the concentration of Cu is fixed (0, 1, 2 or 6 at.%, respectively) while N content is varied. The typical wide photoluminescence spectrum of Anatase TiO_2 has been recorded and the superimposition of the interference fringes due to multiple reflections at the film interfaces of the PL emission is observed. Photoluminescence envelope is compatible for its width as well as for its lineshape with radiative recombination of self-trapped excitons and impurity trapped excitons [14].

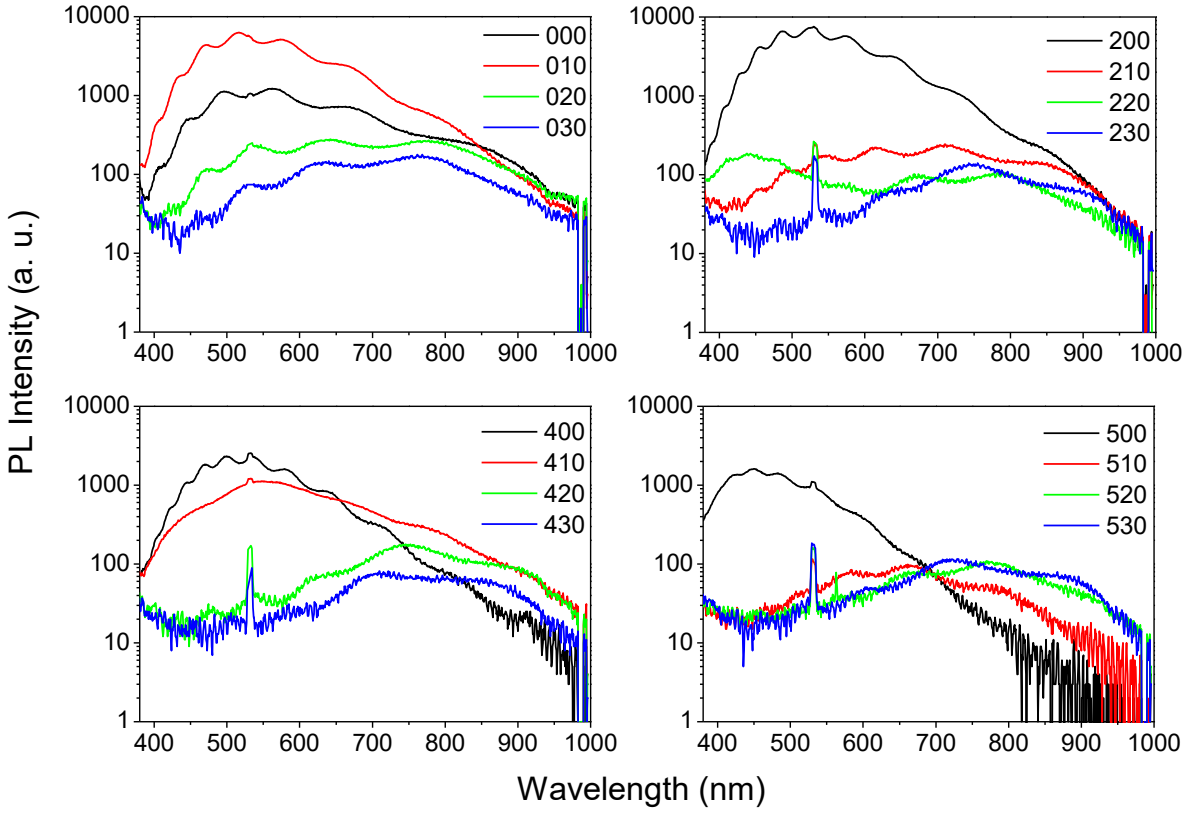

Figure 6.8: Photoluminescence spectra of four different sets of samples. The 532 nm peak is the laser residual transmitted through the UV filter.

In pure TiO_2 and in samples doped only with Cu, the PL spectrum is constituted by a very broad feature centered at around 500 nm, whose intensity lowers by increasing the dopant concentration. The insertion of Nitrogen in the structure quenches the main emission band (400-650 nm), leaving a faint component in the NIR region, around 750-800 nm. From these results, it appears that Cu and N play two different roles in the network. In particular, copper is dispersed in the matrix in such a way to leave an Anatase connected structure allowing the exciton formation and radiative recombination, giving rise to the characteristic PL feature. On

the other hand, Nitrogen more heavily affect the oxide structure, through Ti-N linkages, in such a way to quench the TiO_2 exciton luminescence through charge trapping or energy transfer mechanisms.

Time-resolved photoluminescence (performed on the samples grown on silicon) gave interesting information about the carrier recombination dynamics (*figure 6.9*). In particular it can be seen that pure TiO_2 shows two different PL centers. At around 400-450 nm a typical single exponential decay, with a recombination lifetime in the order of 100 μs, ascribed to the exciton recombination, can be observed. For longer wavelengths, the decay becomes more and more complex, and at around 600 nm the temporal law which better explains the photoluminescence decay is the so-called stretched exponential decay:

$$I_{PL} = I_0 e^{-(\frac{t}{\tau})^{\beta}}$$

where I_0 is the photoluminescence intensity at time t = 0 sec, τ the time decay parameter and β a pure number between 0 and 1. So, at higher wavelengths, the PL components are related to intrinsic TiO_2 defects, probably present at the nano-column surfaces [15].

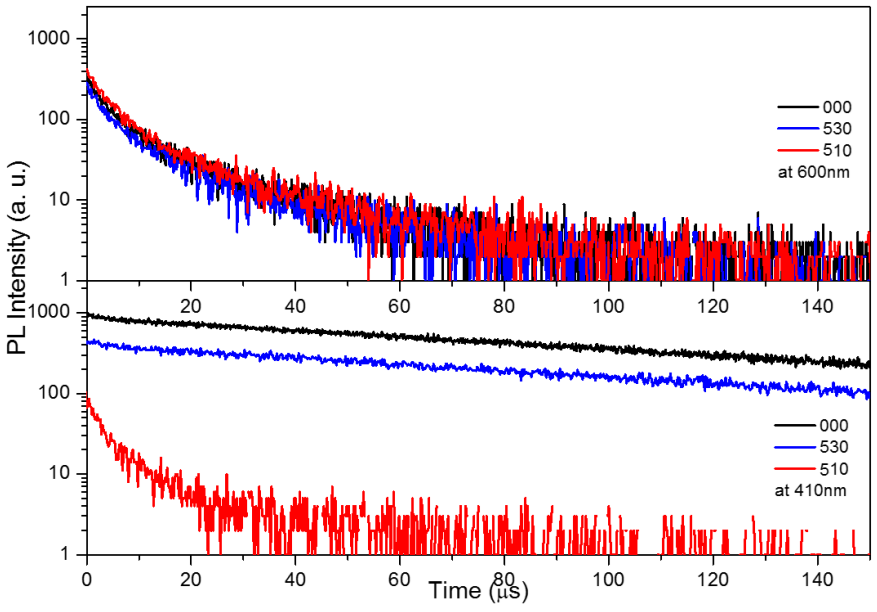

Figure 6.9: Top panel shows the photoluminescence decay for samples 000, 530 and 510 in the defects region around 600 nm. Bottom panel the decay in the bandgap recombination related region.

In doped samples 530 and 510 (*figure 6.9*), the single exponential decay with ≈100 μs characteristics lifetime is present only close to the bandgap spectrum region, whilst at lower energies the decay curve again becomes a stretched exponential, indicating a recombination

path involving carrier diffusion/hopping through the defects matrix before their radiative or non-radiative recombination. In particular, sample 510 shows no bandgap emission and the recombination is purely a stretched one, with a lifetime of about 6 μs and $\beta = 0.7$, corresponding to a mean relaxation time $\langle\tau\rangle \approx 7.6$ μs [16]. It is clear that the increasing concentration of centers related to the doping elements creates nonradiative recombination-centers hindering the emission feature of pure TiO_2 and leaving the components related to network defects. *Figure 6.9* gives a glance of such a behavior. The lifetimes observed in this work are compatible with those observed by Wakabayashi et al. and Sekiya et al. [17, 18], in particular when they used high-quality (colorless) anatase crystals and approached 300 K. However, it has to be taken into account that in literature carriers lifetimes in TiO_2 present values ranging from nanoseconds to microseconds, due to the different microstructures [19-23] allowing different paths to photocarrier recombination and affecting the lifetimes of charge-layers on the surface.

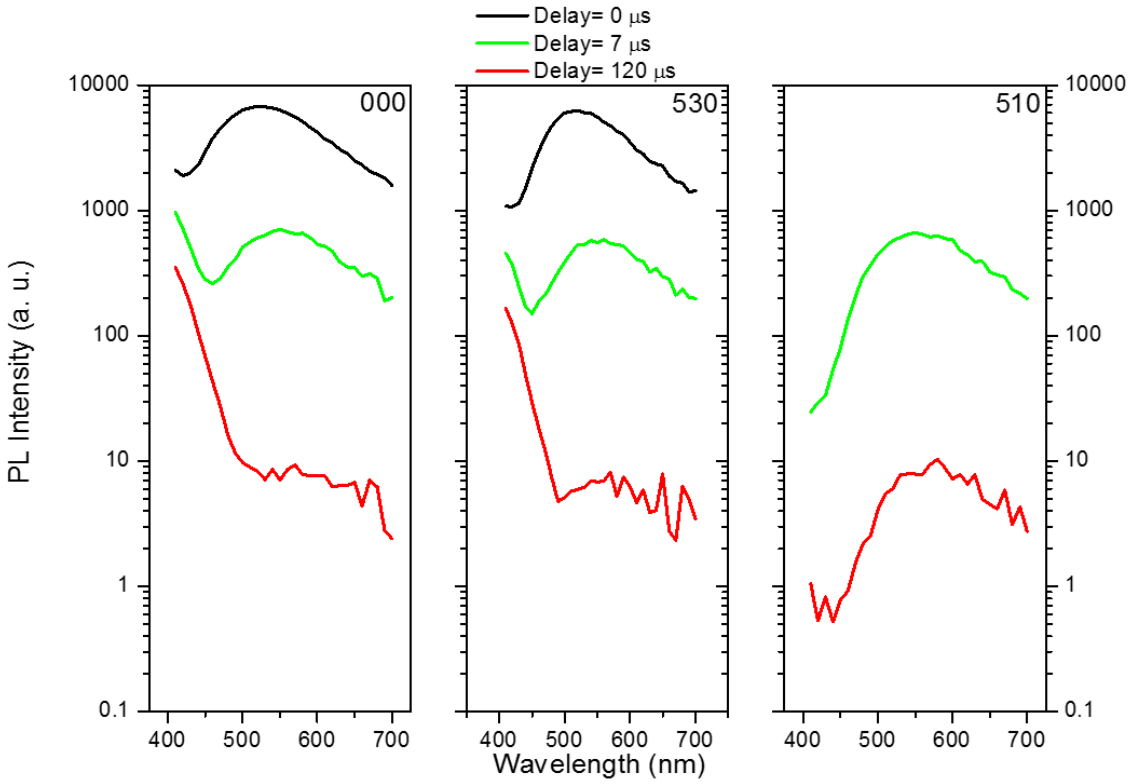

Figure 6.10: The panels report, for the samples indicated in the insets, the time-resolved spectra at different delays. It can be clearly seen how the bandgap UV emission (the right part of it at above 400 nm) becomes dominating at wider time windows.

Time resolved spectra, shown in *figure 6.10*, enlighten the different contributions of TiO_2 matrix and defect related features. In particular, the latter has longer lifetimes and it prevails in

the spectrum collected 120 μs after the laser-pulse arrival. It can be clearly seen also how the Cu-N co-doping changes the film optical properties when the dopant concentration is high; in fact, the bandgap related recombinations are completely quenched in favor of defect ones.

6.3.5 Electrochemical and photo-electrochemical measurements

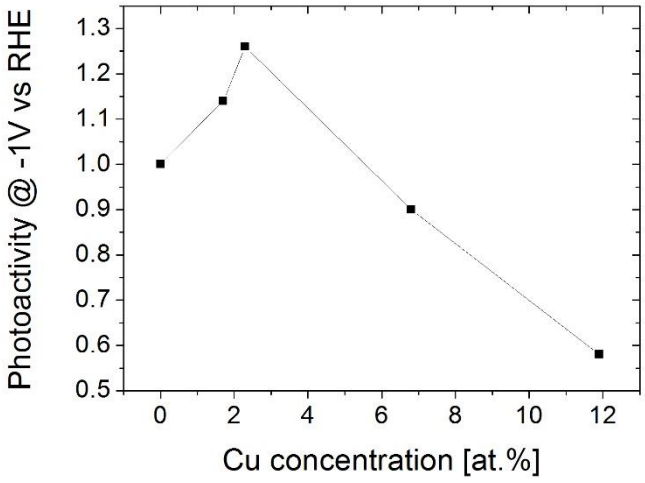

Figure 6.11: TiO_2 photocatalytic activity at different Cu concentrations. The photo-activity is normalized to pure TiO_2 one.

Comparing the photo-electrochemical behaviour of the samples with different concentrations of species, a dependence of the photocatalytic activity on the type and concentration of dopants is observed. In particular, a major influence is observed on the reduction part, whereas oxidation process seems to be inhibited. The effect of copper doping on the photoactivity of TiO_2 is shown in *figure 6.11*. As can be observed, the photoactivity is enhanced of 30% by increasing the copper concentration up to 2%. For higher concentrations, the photoactivity drops down and the sample behaves worse than pure TiO_2.

Figure 6.12 shows the linear sweep voltammetries vs. RHE of the set doped with Cu at 2.0 at.% and different N concentrations. The photoactivity is enhanced by copper doping and it is further improved by adding N. The best film is the one with the highest nitrogen content (1.3 at.%). The enhancement of water reduction reaction and the detriment of water oxidation, can be clearly seen from the LSVs. The overpotential for water reduction, recorded at 200 μA, goes from 244 mV for pure TiO_2 down to 174 mV for Cu doped TiO_2 and to 114 mV for Cu and N co-doped TiO_2. This fact clearly indicates an enhanced electro-activity towards water reduction. This behaviour of Cu doped and Cu and N co-doped TiO_2 films can be explained by the different electrical properties of the samples. Sputtered TiO_2 has an *n*-type character due to the presence

of oxygen vacancies, which act as electron donors. The presence of oxygen vacancies is known to originate from the preferential sputtering of oxygen atoms by argon ions in the deposition process [9].

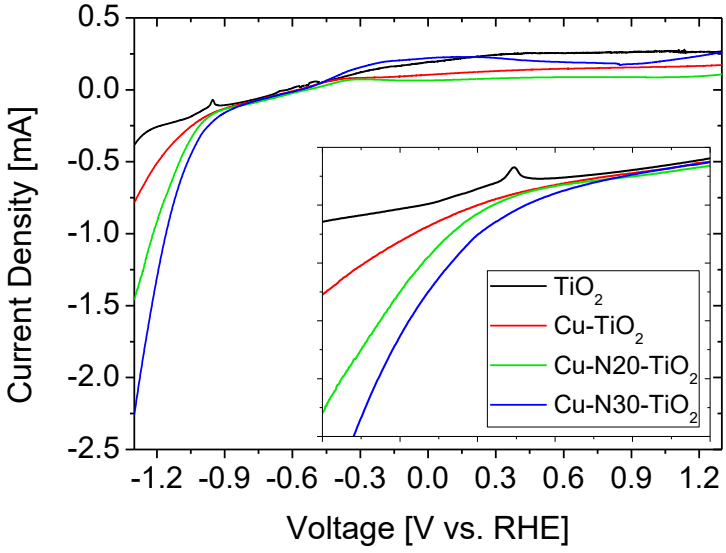

Figure 6.12: Linear sweep voltammetries of pure, 2% Cu-doped, and 2% Cu-N co-doped TiO_2, under illumination. The photoactivity of TiO_2 is enhanced by Cu doping and improves after co-doping with Cu and N.

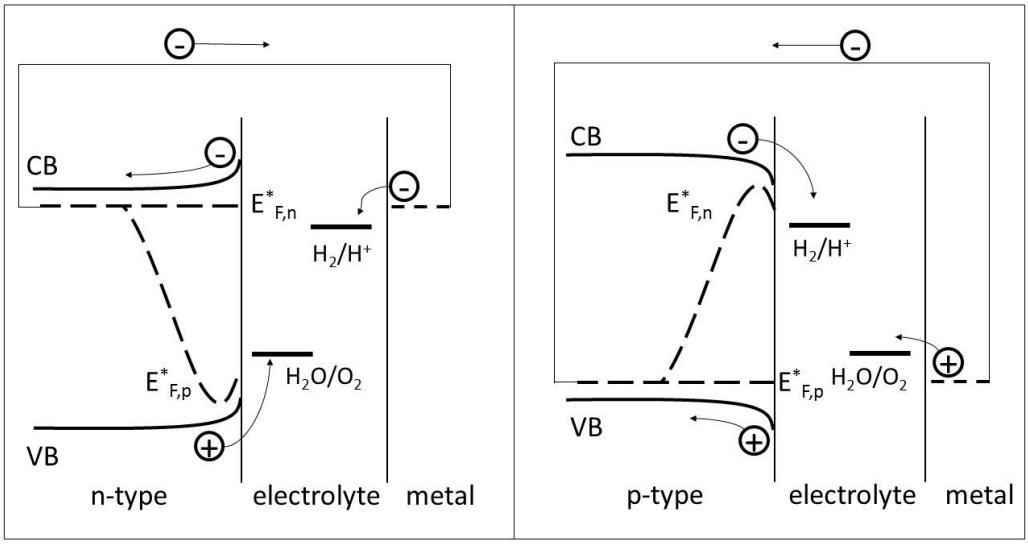

Figure 6.13: Band diagram for a photo-electrochemical cell based on a semiconducting photoelectrode (n-type on the left, p-type on the right) that is electrically connected to a metal counter electrode under illumination. Near the semiconductor/electrolyte interface, the Fermi level splits into quasi-Fermi levels for the electrons and holes.

When a *n*-type semiconductor gets in contact with the electrolyte, the equilibration of its Fermi level with the redox level of water results in a band bending that enhances the flow of holes

from the semiconductor to the solution (*figure 6.13* - left). Therefore, TiO_2 is normally employed as photo-anode. The observed enhancement of the water reduction and concomitant decrease in the water oxidation efficiency, can be explained by the transformation of Cu/N TiO_2 into a *p*-type semiconductor [2]. In fact, in this case the equilibration of the Fermi level with the redox potential of the water results in a band bending that enhances the flow of electrons from the semiconductor to the solution (*figure 6.13* - right). Moreover, the CB of TiO_2, is more negative than the water reduction potential, which results in a low rate of reduction reaction. In *p*-type doped TiO_2 the whole band gap shifts upward, enhancing the efficiency of water reduction as represented in *figure 6.13.*

The sample giving the highest photocurrent is the one co-doped with Cu and N at 2.0 at.% and 1.3 at.%, respectively. Copper concentration coincides with the optimal concentration reported by Jaiswal *et al*. [5], while N concentration is lower. In fact, the optimal concentration of N is reported to be around 3 – 4 at.% [5, 9]. At these doping concentrations, as we have seen in previous sections, codoped films did not show any significant enhancement in visible light absorption. Therefore we think that co-doped samples could work even better if we succeed in incorporating more nitrogen into the films.

6.4 Conclusions

A set of twenty samples of TiO_2 thin films doped and codoped with different amounts of Cu (1-7 at.%) and N (0.7-1.3 at.%) were deposited by RF-magnetron sputtering. Raman spectra showed that all the films grew in the Anatase phase, even in doped and codoped samples. XPS measurements evidenced that at low concentrations Cu is present mainly as Cu^+, while at higher concentrations the Cu^{2+} oxidation state prevails. N is present both as substitutional and interstitial dopant. Time resolved PL analysis showed that Cu-N co-doping hinders the exciton radiative recombination in the Anatase network, giving rise to an increase of the mean lifetime and increasing the recombination probability on defects at the nano-column surface. Photo-electrochemical characterization of codoped samples exhibited an enhancement of the reduction reaction and a concomitant weakening of the oxidation reaction that was explained by a change of the electrical character of the samples from n-type (pure TiO_2) to p-type (codoped TiO_2). Future work will be aimed at depositing codoped films with a higher content of nitrogen, which should enhance the visible light absorption and thus the photo-electrochemical activity of the samples.

6.5 References

1. Zhu, W., et al., *Band gap narrowing of titanium oxide semiconductors by noncompensated anion-cation codoping for enhanced visible-light photoactivity.* Physical review letters, 2009. **103**(22): p. 226401.
2. Dashora, A., et al., *Formation of an intermediate band in the energy gap of TiO_2 by Cu–N-codoping: First principles study and experimental evidence.* Solar Energy Materials and Solar Cells, 2014. **125**: p. 120-126.
3. Wang, S., et al., *Enhanced optical absorption and photocatalytic activity of Cu/N-codoped TiO_2 nanocrystals.* Materials Science in Semiconductor Processing, 2014. **24**: p. 247-253.
4. Song, K., et al., *Photocatalytic activity of (copper, nitrogen)-codoped titanium dioxide nanoparticles.* Journal of the American Ceramic Society, 2008. **91**(4): p. 1369-1371.
5. Jaiswal, R., et al., *Copper and Nitrogen co-doped TiO_2 photocatalyst with enhanced optical absorption and catalytic activity.* Applied Catalysis B: Environmental, 2015. **168–169**: p. 333-341.
6. Ohsaka, T., *Temperature dependence of the Raman spectrum in Anatase TiO_2.* Journal of the Physical Society of Japan, 1980. **48**(5): p. 1661-1668.
7. Choi, H.C., Y.M. Jung, and S.B. Kim, *Size effects in the Raman spectra of TiO_2 nanoparticles.* Vibrational Spectroscopy, 2005. **37**(1): p. 33-38.
8. Bianco, F., et al., *Two-dimensional micro-Raman mapping of stress and strain distributions in strained silicon waveguides.* Semiconductor Science and Technology, 2012. **27**(8): p. 085009.
9. Delegan, N., et al., *Bandgap tailoring of in-situ nitrogen-doped TiO_2 sputtered films intended for electrophotocatalytic applications under solar light.* Journal of Applied Physics, 2014. **116**(15): p. 153510.
10. Ertl, G., et al., *XPS study of copper aluminate catalysts.* Applications of Surface Science, 1980. **5**(1): p. 49-64.
11. Jolley, J.G., et al., *Auger electron and X-ray photoelectron spectroscopic study of the biocorrosion of copper by alginic acid polysaccharide.* Applied surface science, 1989. **37**(4): p. 469-480.
12. Parmigiani, F., et al., *Studies of the Cu-O bond in cupric oxide by X-ray photoelectron spectroscopy and ab initio electronic structure models.* Journal of electron spectroscopy and related phenomena, 1992. **59**(3): p. 255-269.

13. Benoit, R., *LaSurface Web Site*. 2001, Centre National de la Recherche Scientifique (CNRS) in conjunction with Thermo Fisher Scientific: France.
14. Tang, H., et al., *Photoluminescence in TiO_2 anatase single crystals.* Solid State Communications, 1993. **87**(9): p. 847-850.
15. Vial, J., et al., *Mechanisms of visible-light emission from electro-oxidized porous silicon.* Physical Review B, 1992. **45**(24): p. 14171.
16. Gradshteyn, I. and I. Ryzhik, *Table of integrals, series, and products: corrected and enlarged edition*. 1980, Academic Press, Inc. San Diego.
17. Wakabayashi, K., et al., *Time-resolved luminescence spectra in colorless anatase TiO_2 single crystal*. Journal of luminescence, 2005. **112**(1): p. 50-53.
18. Sekiya, T., et al., *Relaxation process in anatase TiO_2 single crystals with different colors*. Journal of luminescence, 2004. **108**(1): p. 69-73.
19. Xu, M., et al., *Photocatalytic activity of bulk TiO_2 anatase and rutile single crystals using infrared absorption spectroscopy.* Physical review letters, 2011. **106**(13): p. 138302.
20. Yamada, Y. and Y. Kanemitsu, *Determination of electron and hole lifetimes of rutile and anatase TiO_2 single crystals.* Applied Physics Letters, 2012. **101**(13): p. 133907.
21. Bahnemann, D.W., M. Hilgendorff, and R. Memming, *Charge carrier dynamics at TiO_2 particles: reactivity of free and trapped holes.* The Journal of Physical Chemistry B, 1997. **101**(21): p. 4265-4275.
22. Cavigli, L., et al., *Volume versus surface-mediated recombination in anatase TiO_2 nanoparticles.* Journal of Applied Physics, 2009. **106**(5): p. 053516.
23. Fujihara, K., et al., *Time-resolved photoluminescence of particulate TiO_2 photocatalysts suspended in aqueous solutions.* Journal of Photochemistry and Photobiology A: Chemistry, 2000. **132**(1): p. 99-104.

Chapter 7

Pulsed-laser deposition of nanostructured Fe_2O_3 catalysts for efficient water oxidation[1]

In this chapter, we study the functionalization of indium tin oxide surface by nanostructured iron oxide coatings. On one side, we demonstrate the validity of pulsed laser deposition for the preparation of nanoparticles assembled coatings of amorphous iron oxide. On the other side, we show the good efficiency of this nanostructured material as water oxidizing catalyst.

7.1 Introduction

Materials designed for a photo-driven fuel synthesis must perform two essential functions: (1) sunlight absorption to generate electron-hole pairs and (2) catalysis of the fuel-forming reactions. The latter becomes critical when multi-electron redox reactions are involved, leading to slow kinetics and consequent loss of efficiency. A significative example of this is photochemical water electrolysis as performed in a photo-electrochemical cell (PEC), where the strict kinetic requirements dictated in particular by the oxygen evolution reaction (OER), which involves the exchange of four electrons, have driven for decades the search for efficient catalysts [1-3].

In recent years, the research efforts have been increasingly directed towards schemes were the two functions are separately optimized and then integrated by functionalization of absorber

[1] This chapter is based on the results published in: M. Orlandi, S. Caramori, F. Ronconi, C. A. Bignozzi, Z. El Koura, N. Bazzanella, L. Meda, and A. Miotello; ACS Appl. Mater. Interfaces 6 (2014) 6186−6190

materials with redox catalysts. Examples include inorganic semiconductors or molecular chromophores as absorbers functionalized by coupling with molecular catalysts or nanostructures of metals or metal-oxides [4-11]. This kind of scheme allows for a simpler yet more in-depth screening of candidate catalysts while taking advantage of materials with already optimized optical properties (e.g. for photovoltaic applications), but also presents new challenges. A critical issue is the parasitic light blocking [5, 12] by catalysts deposited on the absorber surface. In the case of metal-oxides OER catalysts deposited on photoanodes, the effect of optical losses on the overall efficiency is so severe that in a recent investigation the best performance was obtained with a subnanometer film thickness [13]. The use of hydrogen evolving catalysts such as Ni-Mo, MoS_2 and WS_2 deposited on photocathodes faced similar problems [14, 15]. On the other hand, a higher catalyst mass loading is generally beneficial in terms of overpotential performance. This trade-off between optical losses and catalyst loading limits the application of earth-abundant, cheap and scalable alternatives to noble-metal based catalysts, since the replacement generally has lower catalytic activity and higher quantities would be needed to produce a comparable performance [16, 17].

Amorphous iron oxide (a-Fe_2O_3) has been identified as a suitable water oxidation catalyst, conjugating an overall good catalytic performance [18, 19] in both electrolysis [20] and solar water oxidation [21] to the advantage of being earth-abundant, nontoxic, and environmentally safe. Moreover, for this application, the low absorbance of iron oxide becomes an advantage and the low diffusion length of holes is not an issue if the film is sufficiently thin and nanostructured.

To our knowledge, three techniques are commonly employed for the preparation of a-Fe_2O_3: successive ionic layer adsorption and reaction (SILAR) [21], electrodeposition [22, 23] and photochemical metal-organic deposition (PMOD) [20]. All three methods require contact of the substrate with a solution phase. SILAR is a fast and cheap technique requiring only common laboratory glassware, which leads, however, to incomplete surface coverage and poor adhesion, and it grants no control over morphology of the deposited catalyst. Electrodeposition, which could lead to nanostructured surfaces, suffers from similar problems. PMOD is a versatile technique to obtain amorphous metal and mixed-metal oxides by spin-coating solutions of metal-organic precursors followed by UV irradiation. However, the resulting films present smooth and featureless surfaces, whereas a high roughness is generally beneficial in catalysis.

Pulsed-laser deposition (PLD) of thin-films is a technique that employs high-energy-density laser pulses to generate, in the regime of phase explosion, ablated material from a solid target,

consisting of a mixture of vapor/liquid nanodroplets. PLD could present some significant advantages over the methods listed above: precise control of the quantity of the deposited material, enhanced adhesion due to the energetic nature of the process, and, most important, the possibility of nanostructuring the surface by deposition of nanoparticles (NPs) [24-26]. Additionally, being essentially a physical deposition method, it is suitable to all kind of substrates. The main drawback of the PLD technique is the need of specialized equipment, although this is already employed in industrial applications [27]. A more detailed description of this deposition technique is given in Appendix1.

We report here the successful application of PLD to the synthesis of a-Fe_2O_3 NPs for functionalization of indium-tin oxide (ITO) electrodes showing very good electrocatalytic activity toward water oxidation. ITO as a conductive substrate has been chosen for its transparency to visible light, in the perspective of extending the methodology to functionalization of silicon-based photovoltaic cells, following the approach to solar hydrogen generation proposed by Kanan and Nocera [28, 29]. In such commercially available multijunction cells, ITO is commonly present as a protecting anodic conductive layer.

7.2 Experimental methods

7.2.1 Samples preparation

ITO thin films were deposited by radio-frequency magnetron sputtering (RF-MS) using a commercial (Sematrade) ITO disk (purity 99.99 %) as target and Ar (purity 99.99%) as working gas at a pressure of $8x10^{-3}$ mbar. Before deposition, a base pressure of about $2x10^{-7}$ mbar was attained and contaminations on the target surface were removed by pre-sputtering for 20 min. The sample-target distance was kept constant at 5.5 cm and the RF power was maintained at 100 W throughout the deposition. Each deposition was done on both silicon and glass substrates to allow a complete characterization of the catalysts: glass substrates are suitable for electrochemical and spectroscopic characterization and silicon substrates for electron microscopy and elemental analysis. Samples were then annealed in a tubular furnace in air at 220°C for 2 hours (heating ramp: 2°C/min.) to increase transmittance and lower sheet resistance (R_s) and resistivity (ρ).

Subsequently, the electrodes were employed as substrates for pulsed laser deposition (PLD) and were covered by iron oxide nanoparticles (NPs) assembled coatings. Laser ablation was

carried out by using a pure (99.9%, Sematrade) Fe target and a KrF excimer laser (Lambda Physik LP 220i) with an operating wavelength of 248 nm and pulse duration of 25 ns. The repetition rate was set to 20 Hz and the laser fluence to 2.0 J/cm^2. The PLD chamber was evacuated up to a base pressure of 10^{-6} mbar prior to the deposition and then an oxygen flux was let in such that a constant pressure of $4.5x10^{-2}$ mbar was maintained throughout the deposition time. Target to substrate distance was 5.5 cm and substrate temperature (T_S) was set at different values, namely: 30, 100, 200, 300 °C. Either 2000 (2K) or 6000 (6K) pulses were applied during the deposition process. Some of the samples were annealed after preparation at 500°C in air for 2 h to obtain crystalline hematite films to use as reference.

7.2.2 Characterization

Sheet resistance and resistivity measurements were carried out with a I/V apparatus equipped with an in-line four-point probe as described in reference [30].

GIXD analysis were carried out on a Philips X'Pert θ/2θ automatic diffractometer with grazing incidence geometry, with fixed incidence angle ω = 1.0°, employing Cu K_α (λ=1.5416 Å, 1.6 kW) radiation. Angular range was 5-90° (2θ), with 0.02° (2θ) steps and acquisition time 25 seconds per step. Inorganic phases identification was performed with the Hanawalt method on PDF-2 (Powder Diffraction File, ICDD) data-set. Crystallite size, when indicated, is estimated by peak broadening with a method taken from Fundamental Parameter Approach (FPA – TOPAS software).

X-ray Photoelectron Spectra (XPS) were recorded using a PHI-5500–Physical electronics spectrometer, equipped with a monochromatized source with an Al anode (Ka = 1486.6 eV), operating at 200 W of applied power, 5.85 eV pass energy, and 0.05 eV energy-step. XPS spectra were collected at take-off angles of 45°. The analyzed area is around 0.5 mm^2 and the sampling depth is within 10 nm. During measurements, the vacuum level was around 10^{-9} mbar residue pressure. The spectrometer was calibrated assuming the Ag(3d 5/2) binding energy (BE) at 368.3 eV with respect to the Fermi-level and the measured full-width-half-maximum (FWHM) was 0.46 eV. In order to neutralize the surface electrostatic charge of non-conductive samples, an electron gun was used. Furthermore, the charging effect on the analysis was also corrected considering the BE value of C(1s), due to adventitious carbon, at 284.8 eV. The BEs were measured at the maximum of the peaks without any baseline subtraction.

Scanning electron microscopy (SEM) was used to analyze the morphology and thickness of films. The surface of the films was analyzed by a JEOL JSM-7001F field effect gun (FEG-SEM) apparatus at 30 keV beam energy. SEM apparatus is equipped with an Energy Dispersive X-ray Spectroscopy detector (EDXS, Oxford INCA PentaFETx3). Working Distance (WD) was maintained between 4 to 8 mm. Surface morphology images were acquired at 20° tilt angle whereas cross section analysis were performed putting the films on a 90° stub.

UV-Vis Transmittance spectra were recorded on a Cary 5000 spectrophotometer using a microscope glass slide as blank, while microRaman analysis was carried out on a Horiba LabAramis setup equipped with a HeNe 633 nm laser as source.

Electrochemical measurements were performed on a PGSTAT 302/N workstation equipped with FRA2 frequency response analyzer. Electrochemical experiments were generally performed in a three-electrode configuration, by using either different types of catalytic Fe(III) electrodes or bare ITO as anodes, Pt as counter-electrode and Saturated Calomel (SCE) as reference electrode, in a 0.5 M carbonate buffer solution at pH 11.8. Linear sweep measurements were obtained between 0.2 V and 1.8 V vs RHE with a scan rate of 50 mV s^{-1}. Chronoamperometry was recorded by imposing a constant potential of 1.64 V vs RHE, without dynamic iR-drop compensation.

7.3 Results and discussion

7.3.1 ITO layer characterization

	Fe 2p	O 1s	Sn3d5	In3d4	C 1s	Si 2p
B.E. (eV)		532.5 – 530.0	486.5	444.5	284.5	102.5
Conc. (atomic %)	---	32.2	0.6	5.4	42.8	19.0

Table 7.1: XPS analysis of ITO surfaces. Binding Energies (BE) were measured with an approximation of 0.5 eV.

Some of the ITO films deposited on glass and silicon were not covered by iron oxide coating to allow a complete characterization of bare ITO. XPS was used to identify the composition and chemical states of the elements in the ITO. The results are summarized in *table 7.1* and indicate the presence of indium(III) (In $3d_4$ peak; binding energy (BE) = 444.5 ± 0.5 eV) and tin(IV) (Sn $3d_5$ peak; BE = 486.5 ± 0.5 eV) with a In/Sn ratio of 9/1 (atomic %). Si is included

as a common contaminant and C is present both as an environmental contaminant and as adsorbed carbonate. Grazing incidence X-ray diffraction (GIXD) reveals a crystalline phase with face-centered-cubic (fcc) structure and unit-cell parameter a = 10.16 Å (*figure 7.5*). The combined results of these analyses are definitely compatible with ITO identification. Scanning electron microscopy (SEM) was employed for thickness measurement via cross-sectional analysis and for surface imaging, revealing compact films of about 450 nm with a polycrystalline surface (*figure 7.*1).

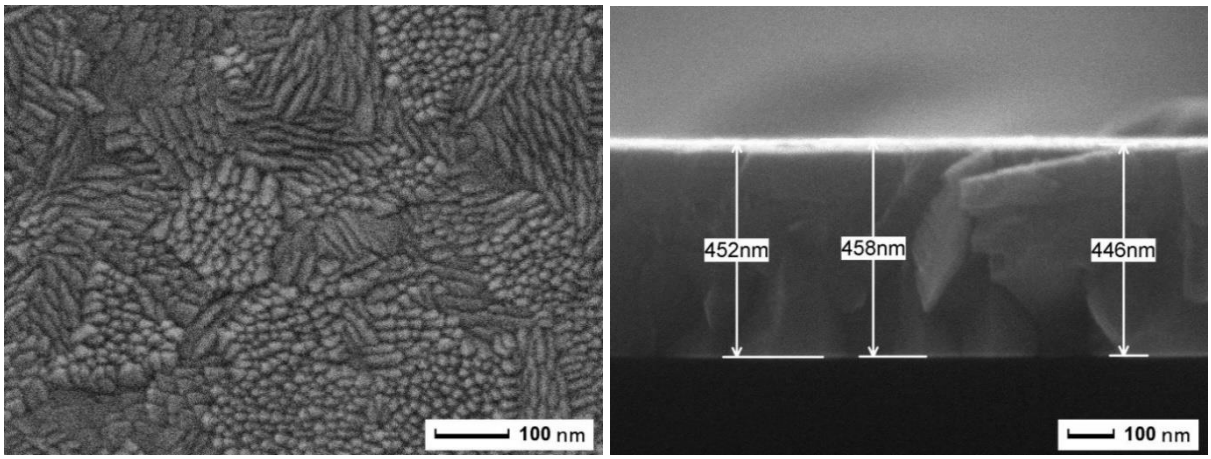

Figure 7.1: SEM top-down (left) and cross-sectional (right) analysis for a typical ITO film.

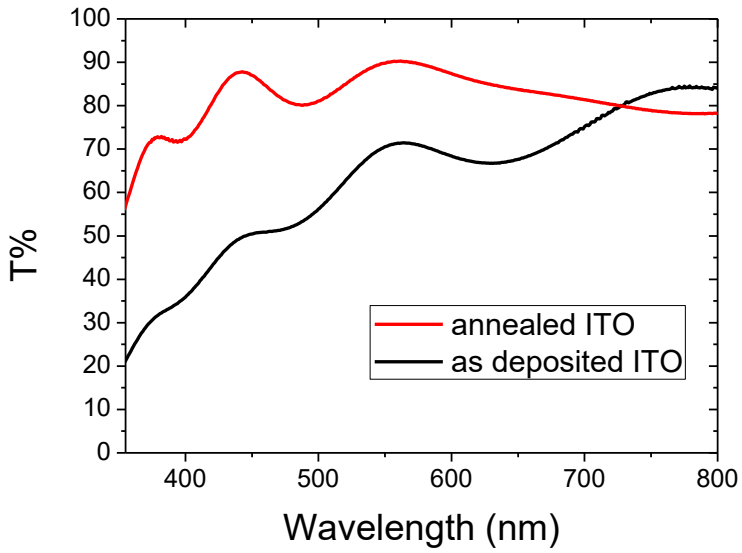

Figure 7.2: UV-Vis transmittance in the 400-800 nm range for a typical ITO film over glass substrate. Comparison between as deposited and annealed films.

The post-annealing of the samples at 220 °C in air for two hours was very beneficial for the optical and electrical properties of the films. *Figure 7.2* shows the transmittance spectra of an ITO film before and after thermal treatment. As deposited films have a transmittance of 35-80% in the range 400-800 nm, which becomes 70-80% in the same range after annealing. At the same time, the sheet resistance (R_S) decreases from 28-22 Ω/sq. to 10-15 Ω/sq., which corresponds to $\rho = (3.6\text{-}5.3) \times 10^{-6}$ Ω. These optical and electrical properties of the deposited films are similar to those of the best ITO thin films commercially available.

7.3.2 Iron oxide coatings characterization

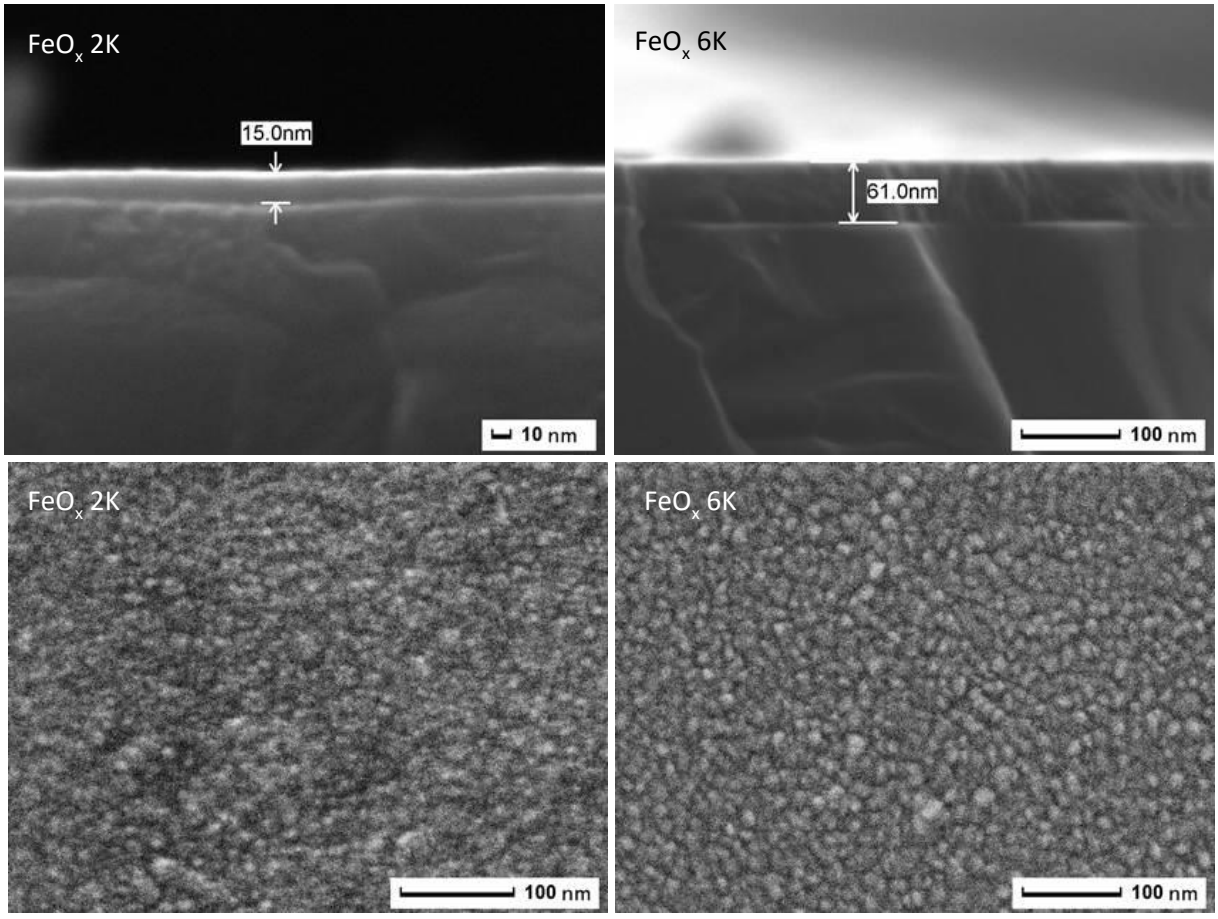

Figure 7.3: SEM images of FeO_x functionalized ITO electrodes: cross-section (top); top-down (bottom).

Pulsed laser deposition on the ITO films results in a complete coverage of the surface, both with 2k and 6k pulses. SEM top-down imaging (*figure 7.3*, bottom) reveals a structured surface, formed by 10-15 nm average diameter round-shaped features of homogeneous size-distribution, present in all samples up to T_S = 300°C. This morphology is common to thin and thick samples and is compatible with a NPs-assembled coating. SEM cross-section images (*figure 7.3*, top)

were used to measure the thickness of the coatings. 6k pulses deposition leads to a thickness of 60 ± 5 nm and 2k to 15 ± 5 nm. It is noteworthy that in the latter case the thickness of the coverage is similar to the diameter of the nanoparticles constituting the coating, meaning that ideally we have a monolayer of NPs completely covering ITO. Thick films were prepared specifically for some characterization techniques such as Raman spectroscopy and GIXD, instead, thin films are the ones useful for the application.

Deposition Temp. (°C)	Fe2p (atomic %) BE (eV)	O1s (atomic%) BE (eV)	C1s (atomic%) BE (eV)	Si2p (atomic%) BE (eV)
30	16.9 710.5	43.5 532.5-529.5	38.0 284.5	1.6 102.5
100	18.7 710.5	44.3 532.5-529.5	34.7 284.5	2.3 102.5
200	11.4 710.5	38.3 532.5-529.5	50.3 284.5	--- 102.5
300	15.7 710.5	36 532.5-529.5	48.3 284.5	--- 102.5

Table 7.2: XPS analysis of 2K a-Fe_2O_3 deposited over glass at various substrate temperatures. Si is included as a common contaminant and C is present both as an environmental contaminant and as adsorbed carbonate. Binding energies were measured with an approximation of 0.5 eV.

XPS analysis of 2K pulses deposition over glass substrates at various substrate temperatures is shown in *table 7.2*. Besides Si and C, which are present as contaminants, only oxygen and iron were detected. The O-1s core level was fitted with two peaks. The main peak is at BE = 529.5 ± 0.5 eV and is generally associated to metal oxides. The second peak, at BE = 532.5 ± 0.5 eV, is associated to metal carbonates. Fe 2p core level presents two peaks associated with Fe $2p_{1/2}$ and Fe $2p_{3/2}$ of Fe(III). The main peak is at BE = 710.5 ± 0.5 eV and is the only one reported in *table 7.2*. This analysis is compatible with iron oxide in form of Fe_2O_3.

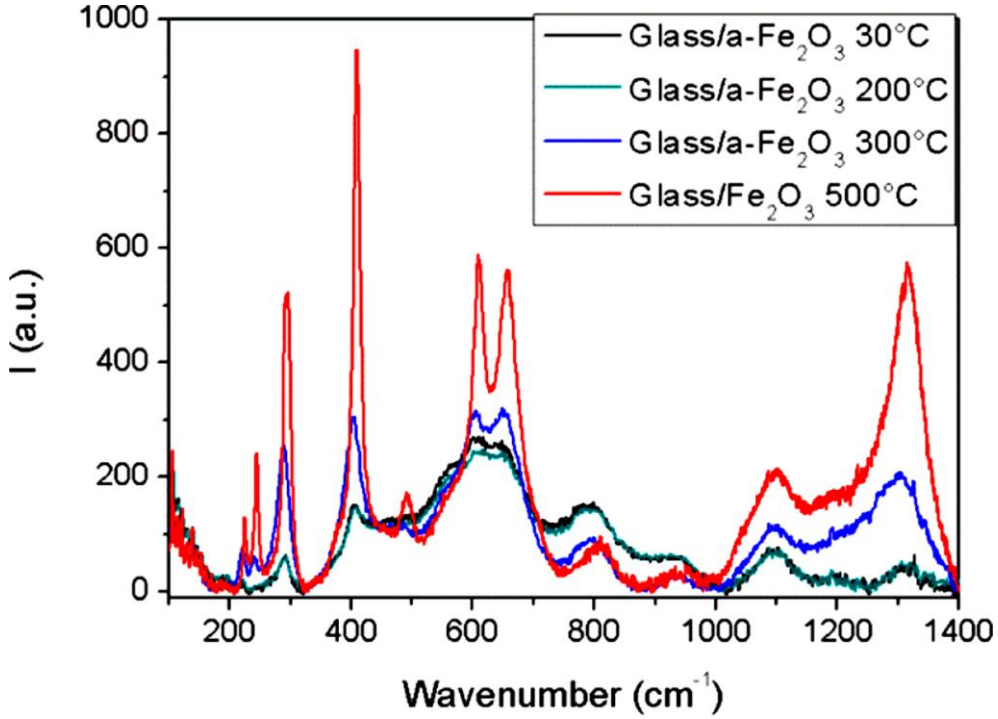

Figure 7.4: Micro-Raman spectra of 6K a-Fe_2O_3 deposited over glass at substrate temperatures of 30, 200 and 300°C and of hematite-functionalized electrodes (glass/Fe_2O_3, 6K, 500 °C).

Micro-Raman spectroscopy of 6K pulses deposition over glass substrates (*figure 7.4*) reveals mostly an amorphous material on samples up to T_S = 300 °C, although a trend of increasing crystallinity with higher T_S is clearly visible with this technique. Samples annealed at 500 °C in air for 2 h appear to be completely crystalline and present all the Raman peaks related to hematite. Hematite belongs to the D_{3d}^6 crystal space group and seven phonon lines are expected in the Raman spectrum [31], namely two A_{1g} modes (225 and 498 cm^{-1}) and five E_g modes (247, 293, 299, 412 and 613 cm^{-1}). All these peaks are present in our spectrum except that we see a band at 297 cm^{-1} instead of the two peaks at 293 and 299 cm^{-1}. However, it was reported that these two peaks can be resolved only at 100 K or less [32]. Moreover, hematite is an antiferromagnetic material and the collective spin movement can be excited in what is called a magnon. The intense feature at 1320 cm^{-1} is assigned to a two-magnon scattering which arises from the interaction of two magnons created on antiparallel close spin sites [31]. The presence of this band indicates unequivocally the hematite phase.

GIXD analysis (*figure 7.5*) of samples up to T_S = 300 °C are compatible with those of a largely amorphous material, showing only a weak signal attributable to the presence of very small (6−11 nm) hematite scattering domains (hexagonal structure, unit-cell parameters a = 5.07 Å and c = 13.90 Å). Henceforth the samples will be labelled as 2k or 6k a-Fe_2O_3.

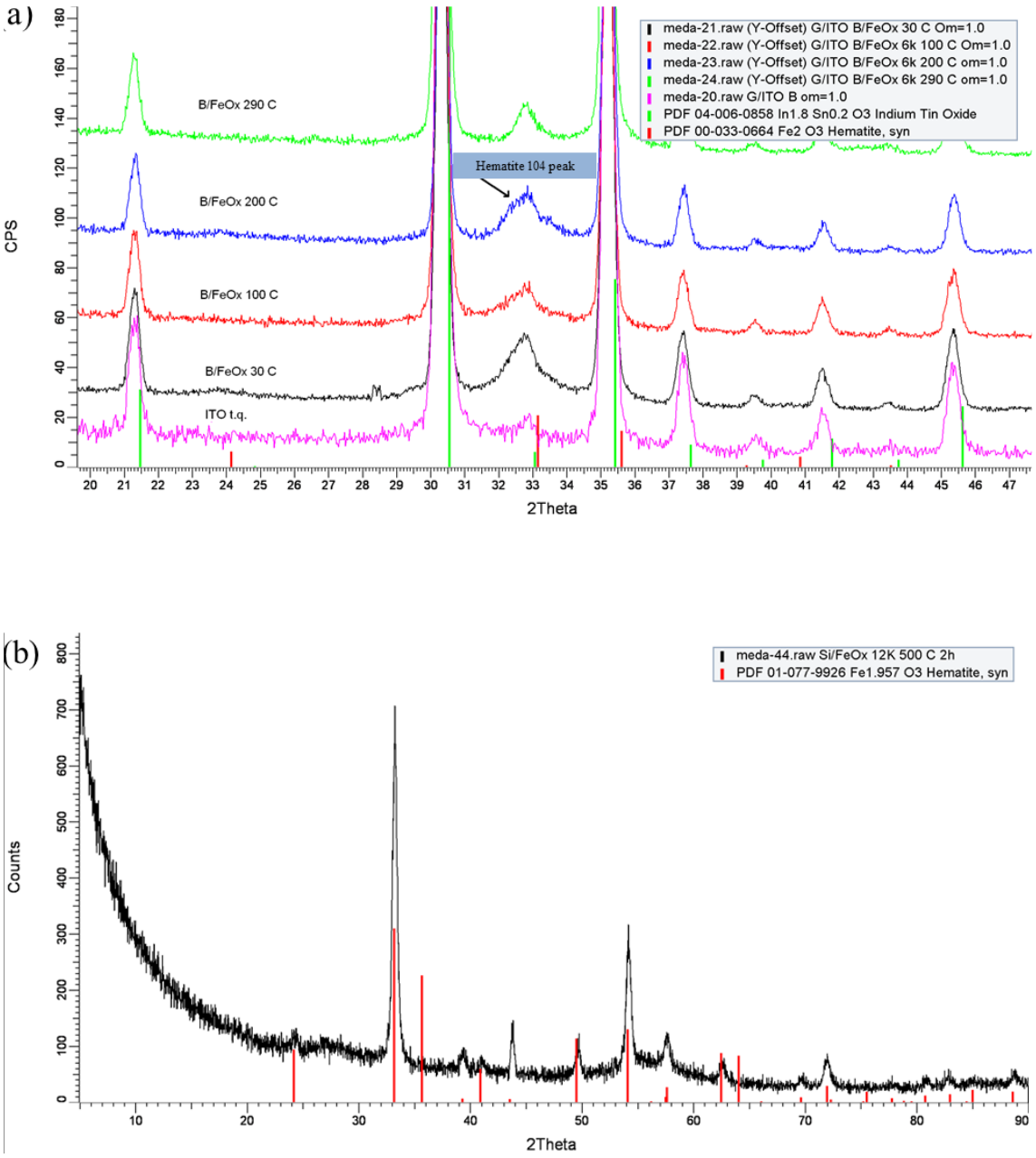

Figure 7.5: (a) GIXD analysis of Fe_2O_3 functionalized ITO electrodes at different deposition temperatures. Bare ITO is shown as reference. (b) GIXD analysis of hematite functionalized silicon substrates (room-temperature deposition followed by annealing at 500°C for 2 h.).

The effect of a-Fe_2O_3 coverage on the optical properties of the samples is shown in *figure 7.6*. Transmittance for 2K pulses samples are between 40 and 70% in the range 400-800 nm.

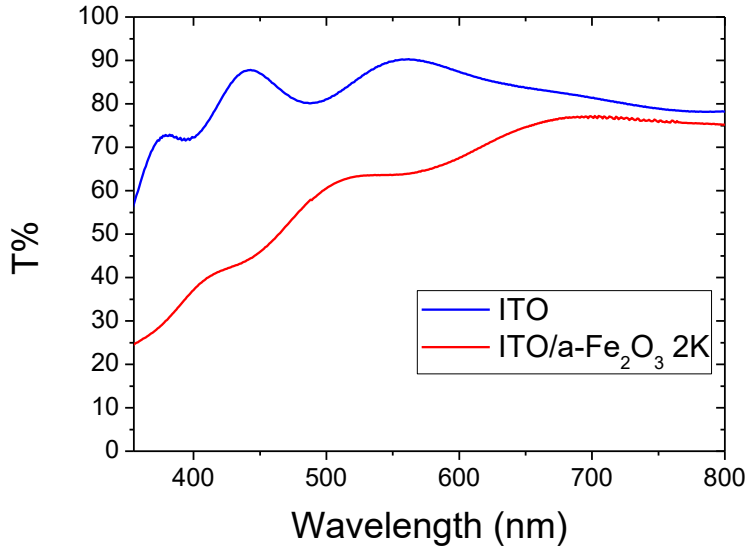

Figure 7.6: UV-Vis transmittance in the 400-800 nm range for 2K a-Fe_2O_3 deposited over ITO coated glass at substrate temperatures of 30°C.

Electrochemical water oxidation experiments were performed in a three-electrode configuration, with either 2K pulses a-Fe_2O_3 or hematite functionalized ITO as working electrode, Pt as the counter-electrode and saturated calomel electrode (SCE) as reference electrode. Because Fe_2O_3 is stable at pH >9 [21], a pH of 11.8 was maintained with 0.5 M Na_2CO_3 buffer to ensure complete stability and thus well-defined electrochemistry. Oxygen evolution at this pH is expected at potential $E_{O2/H2O} = 1.23 – 0.059\ pH = 0.53$ V versus reversible hydrogen electrode (RHE) [33].

In *figure 7.7*, a comparison of the anodic responses of various functionalized electrodes against bare ITO is presented. a-Fe_2O_3 shows considerable electro-activity toward water oxidation (*table 7.3*) when deposited both at 30 °C (ITO/a-Fe_2O_3 2K, 30 °C) and at 300 °C (ITO/a-Fe_2O_3 2K, 300 °C) with onset overpotential η (taken at current density J = 0.2 mA/cm^2) for anodic currents of 513 and 497 mV, respectively, while hematite (ITO/Fe_2O_3, 2K, 500 °C) is only slightly less active with η = 546 mV. Though not exceptional in terms of its onset overpotential, the amorphous catalyst has a remarkably low Tafel Slope, thus being able to sustain considerable current densities at moderate overpotential.

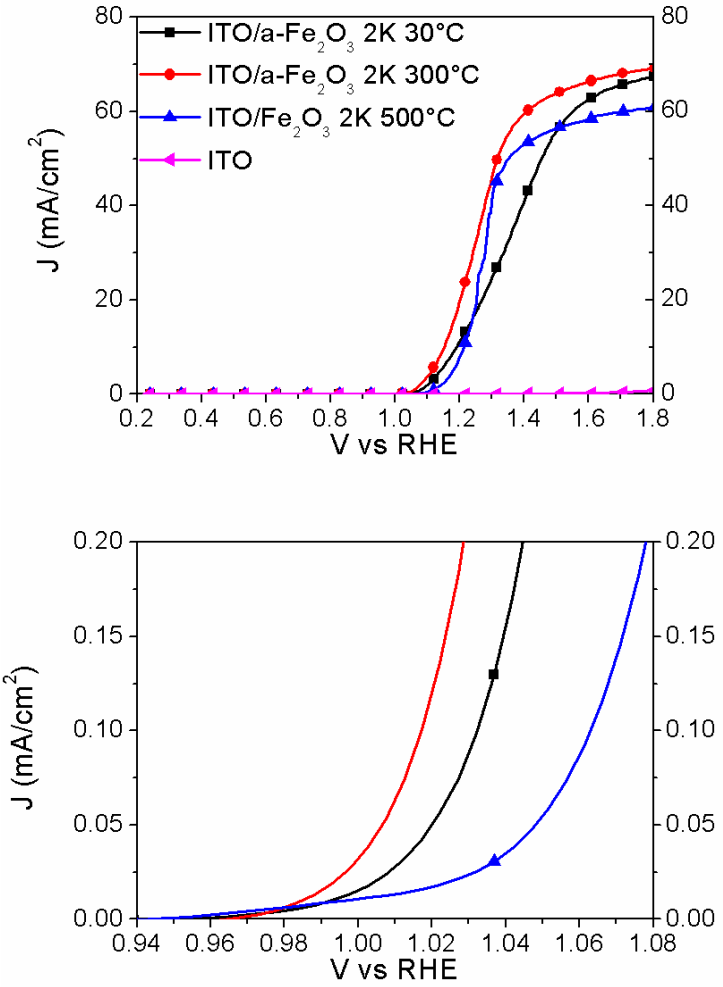

Figure 7.7: Linear sweep voltammetry (top) and its low overpotential magnification (bottom) of 2K a-Fe_2O_3 functionalized electrodes deposited at 30°C (ITO/a-Fe_2O_3, 2K, 30 °C) and at 300 °C (ITO/a-Fe_2O_3, 2K, 300 °C) and of hematite-functionalized electrodes (ITO/Fe_2O_3 2K 500 °C). Bare ITO is reported as the reference. J-V curves compensated for the iR drop.

Sample	η (mV)	Tafel Slope (mV/dec)
ITO/a-Fe_2O_3 2K 30°C	513	39.7
ITO/a- Fe_2O_3 2K 300°C	497	35.6
ITO/ Fe_2O_3 2K 500°C	546	57.3

Table 7.3: Onset (J = 0.2 mA/cm^2) overpotential η and Tafel Slope.

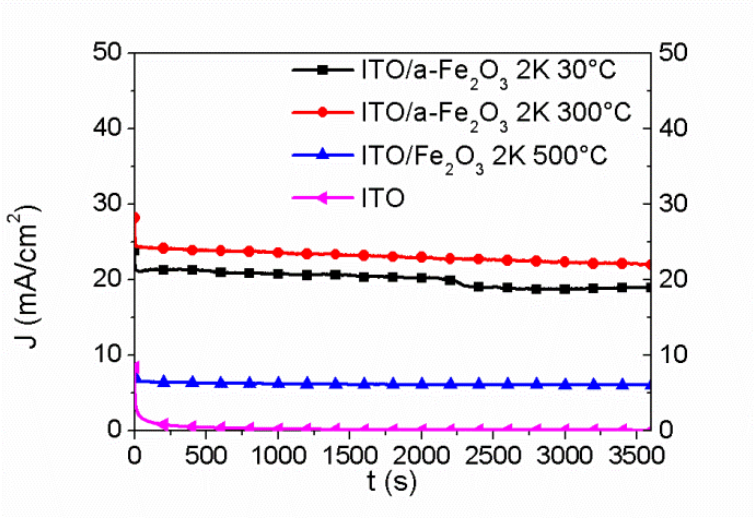

Figure 7.8: 1 h chronoamperometry of 2K a-Fe_2O_3 functionalized electrodes deposited at 30 °C (ITO/a-Fe_2O_3 2K 30°C) and at 300 °C (ITO/a-Fe_2O_3 2K 300°C) and of hematite-functionalized electrodes (ITO/Fe_2O_3 2K 500°C). Bare ITO is shown as the reference. The applied potential is 1.64 V versus RHE. J-t curves did not compensate for the iR drop.

Indeed, where the amorphous material proves superior is in the chronoamperometries ($V_{appl.}$ = 1.64 V vs. RHE for 1 h) reported in *figure 7.8*: while hematite electrodes give current densities of about 6.5 mA/cm^2, the amorphous material can sustain currents of more than 20 mA/cm^2, with ITO/a-Fe_2O_3 2K 300°C performing slightly better (24 mA/cm^2) than ITO/a-Fe_2O_3 2K 30°C (21 mA/cm^2).

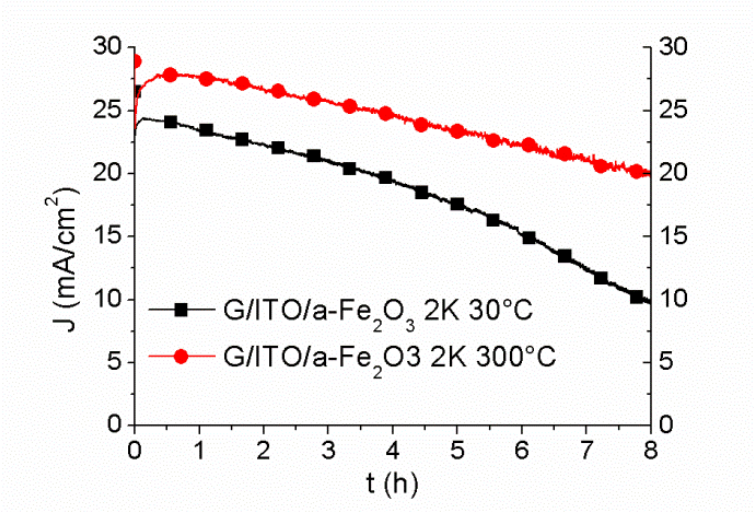

Figure 7.9: 8 h Chronoamperometry of 2K a-Fe_2O_3 functionalized electrodes deposited at 30°C (ITO/a-Fe_2O_3 2K 30°C) and at 300°C (ITO/a-Fe_2O_3 2K 300°C).

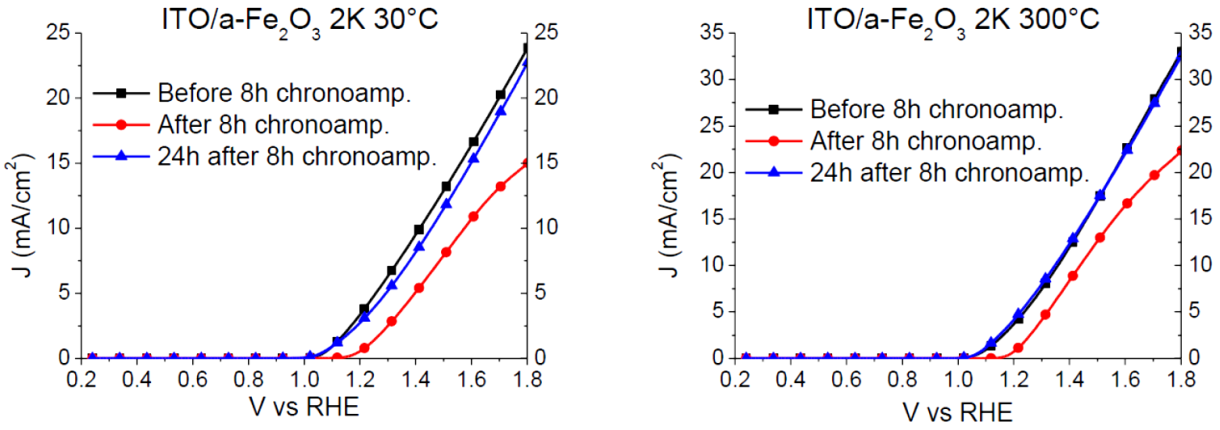

Figure 7.10: Linear sweep voltammetry of ITO/a-Fe_2O_3 2K 30°C (left) and ITO/ a-Fe_2O_3 2K 300°C (right), before (black line), immediately after (red line) and after 24 hours (blue line) the 8h chronoamperometry. Curves not compensated for iR-drop.

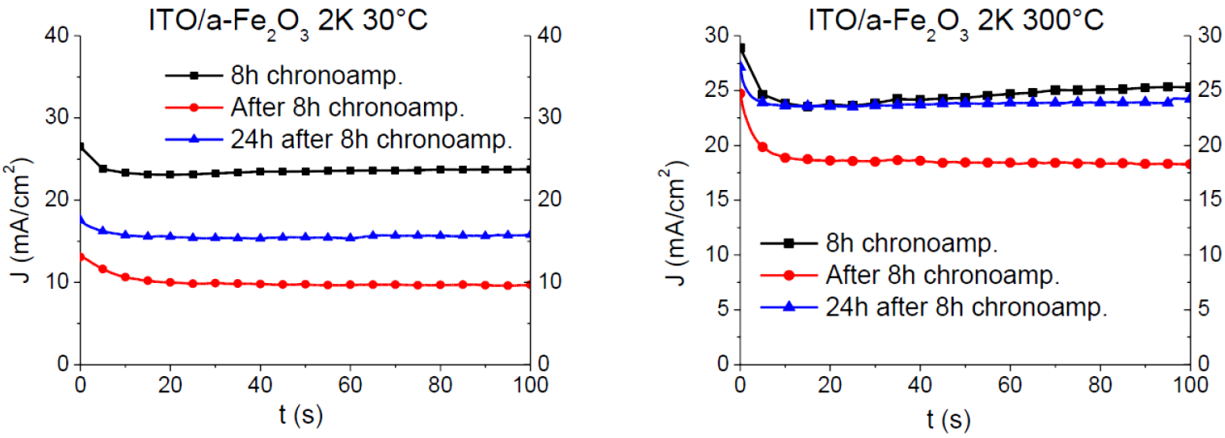

Figure 7.11: Chronoamperometry of ITO/ a-Fe_2O_3 2K 30°C (left) and ITO/ a-Fe_2O_3 2K 300°C (right): Initial scan (black line); immediately after the end of the first 8 h cicle (red line) and after 24 h (blue line) after storage in air in dark conditions. Curves not compensated for iR-drop.

These current levels could be sustained without significant loss for up to 8 h (*figure 7.9*) for ITO/a-Fe_2O_3 2K 300°C, while a drop in the current density accompanied by bleaching of the surface was observed for ITO/a-Fe_2O_3 2K 30°C. This could be due to the loss of catalyst from the electrode surface, indicating that higher $T_{S.}$ improves adhesion. It should be noted that a partial current drop, on the order of 30%, could be observed also in the ITO/a- Fe_2O_3, 2K, 300 °C, electrode, at the end of the 8 h chronoamperometry at 1.64 V versus RHE. Such loss does not appear to be permanent because the initial performance was reobserved on successive J−V

and chronoamperometry scans (*figures 7.10* and *7.11*) recorded on the following days, after rinsing and storing the electrode in air under dark conditions. Thus, the partial current decrease upon prolonged electrolysis may originate by adsorption of ions, of oxidation intermediates, and of molecular oxygen, limiting the active surface of the electrode, rather than by detachment of a-Fe_2O_3, leading to permanent loss of the catalytic performances of the electrode.

Although the exact mechanism of oxygen evolution at a-Fe_2O_3 catalysts is unknown, a recent study [34] on hematite photoelectrodes decorated by an amorphous iron(III) oxide catalyst resulted in enhanced hole trapping in sites capable of undergoing favorable proton-coupled electron transfer reactions, leading to the formation of highly valent Fe^{IV}=O species [35], which may undergo subsequent nucleophilic attack by the water molecule, finally resulting in the oxygen evolution reaction. Such a reaction pathway is probable also in a thin layer electrode, but the exact definition of the reaction intermediates remains a challenging task and requires determination of the coordination environment of the iron(III) and iron(IV) centers in the amorphous film. Such a study is currently underway.

7.4 Conclusions

Amorphous iron oxide nanoparticles assembled coatings were synthesized by pulsed-laser deposition (PLD) for functionalization of indium−tin oxide surfaces, resulting in electrodes capable of efficient catalysis in water oxidation. These electrodes, based on earth-abundant and nonhazardous iron metal, are able to sustain high current densities (up to 20 mA/cm^2) at reasonably low applied potential (1.64 V at pH 11.8 versus reversible hydrogen electrode) for more than 1 h when employed as anodes for electrochemical water oxidation. The good catalytic performance proves the validity of PLD as a method to prepare nanostructured solid-state materials for catalysis. With respect to other methods of preparation, PLD offers significant improvements in terms of material adhesion and control over critical parameters such as surface coverage and morphology. The methodology lends itself to the exploration of other metal oxide catalysts including mixed metal oxides and to functionalization of other surfaces including silicon-based photovoltaic cells or other photoactive materials for solar-powered water splitting.

7.5 References

1. Ruttinger, W. and G.C. Dismukes, *Synthetic water-oxidation catalysts for artificial photosynthetic water oxidation.* Chemical Reviews, 1997. **97**(1): p. 1-24.
2. Lewis, N.S., *Light work with water.* Nature, 2001. **414**(6864): p. 589-590.
3. Kamat, P.V. and J. Bisquert, *Solar fuels. Photocatalytic hydrogen generation.* The Journal of Physical Chemistry C, 2013. **117**(29): p. 14873-14875.
4. Youngblood, W.J., et al., *Photoassisted overall water splitting in a visible light-absorbing dye-sensitized photoelectrochemical cell.* J Am Chem Soc, 2009. **131**(3): p. 926-7.
5. Reece, S.Y., et al., *Wireless solar water splitting using silicon-based semiconductors and earth-abundant catalysts.* Science, 2011. **334**(6056): p. 645-8.
6. Cristino, V., et al., *Efficient solar water oxidation using photovoltaic devices functionalized with earth-abundant oxygen evolving catalysts.* Phys Chem Chem Phys, 2013. **15**(31): p. 13083-92.
7. Orlandi, M., et al., *Ruthenium polyoxometalate water splitting catalyst: very fast hole scavenging from photogenerated oxidants.* Chem Commun (Camb), 2010. **46**(18): p. 3152-4.
8. Klahr, B., et al., *Photoelectrochemical and impedance spectroscopic investigation of water oxidation with "Co-Pi"-coated hematite electrodes.* J. Am. Chem. Soc, 2012. **134**(40): p. 16693-700.
9. Sun, J., D.K. Zhong, and D.R. Gamelin, *Composite photoanodes for photoelectrochemical solar water splitting.* Energy & Environmental Science, 2010. **3**(9): p. 1252.
10. Sartorel, A., et al., *Tetrametallic molecular catalysts for photochemical water oxidation.* Chem Soc Rev, 2013. **42**(6): p. 2262-80.
11. Ye, H., H.S. Park, and A.J. Bard, *Screening of Electrocatalysts for Photoelectrochemical Water Oxidation on W-Doped BiVO4Photocatalysts by Scanning Electrochemical Microscopy.* The Journal of Physical Chemistry C, 2011. **115**(25): p. 12464-12470.
12. McKone, J.R., N.S. Lewis, and H.B. Gray, *Will Solar-Driven Water-Splitting Devices See the Light of Day?* Chemistry of Materials, 2014. **26**(1): p. 407-414.

13. Trotochaud, L.M., T. J.; Boettcher, S. W., *An Optocatalytic Model for Semiconductor-Catalyst Water-Splitting Photoelectrodes Based on In Situ Optical Measurements on Operational Catalysts.* J Phys Chem Lett, 2013. **4**: p. 931-935.
14. Warren, E.L., et al., *Hydrogen-evolution characteristics of Ni–Mo-coated, radial junction, n+p-silicon microwire array photocathodes.* Energy & Environmental Science, 2012. **5**(11): p. 9653.
15. Seitz, L.C., et al., *Modeling practical performance limits of photoelectrochemical water splitting based on the current state of materials research.* ChemSusChem, 2014. **7**(5): p. 1372-85.
16. Popczun, E.J., et al., *Nanostructured nickel phosphide as an electrocatalyst for the hydrogen evolution reaction.* J Am Chem Soc, 2013. **135**(25): p. 9267-70.
17. McKone, J.R., et al., *Ni–Mo Nanopowders for Efficient Electrochemical Hydrogen Evolution.* ACS Catalysis, 2013. **3**(2): p. 166-169.
18. Gondal, M.A., et al., *Production of hydrogen and oxygen by water splitting using laser induced photo-catalysis over Fe_2O_3.* Applied Catalysis A: General, 2004. **268**(1-2): p. 159-167.
19. Balu, A.M., et al., *Fe/Al synergy in Fe_2O_3 nanoparticles supported on porous aluminosilicate materials: excelling activities in oxidation reactions.* Chem. Commun., 2010. **46**(41): p. 7825 - 7827.
20. Smith, R.D.L., et al., *Photochemical route for accessing amorphous metal oxide materials for water oxidation catalysis.* Science, 2013. **340**(6128): p. 60-63.
21. Cristino, V., et al., *Efficient solar water oxidation using photovoltaic devices functionalized with earth-abundant oxygen evolving catalysts.* Physical Chemistry Chemical Physics, 2013. **15**(31): p. 13083-13092.
22. Zotti, G., et al., *Electrodeposition of amorphous Fe_2O_3 films by reduction of iron perchlorate in acetonitrile.* Journal of the Electrochemical Society, 1998. **145**(2): p. 385-389.
23. Schrebler, R., et al., *An Electrochemical Deposition Route for Obtaining α-Fe_2O_3 Thin Films Electrochemical/Chemical Deposition and Etching.* Electrochem. Solid-State Lett., 2006. **9**: p. 110-C113.
24. Warang, T., et al., *Pulsed laser deposition of Co_3O_4 nanoparticles assembled coating: Role of substrate temperature to tailor disordered to crystalline phase and related*

photocatalytic activity in degradation of methylene blue. Applied Catalysis A: General, 2012. **423-424**: p. 21-27.

25. Shaheen, M.E., J.E. Gagnon, and B.J. Fryer, *Laser ablation of iron: A comparison between femtosecond and picosecond laser pulses.* Journal of Applied Physics, 2013. **114**(8).
26. Guo, Q., et al., *Effects of oxygen gas pressure on properties of iron oxide films grown by pulsed laser deposition.* Journal of Alloys and Compounds, 2013. **552**: p. 1-5.
27. Gower, M.C., *Industrial applications of laser micromachining.* Optics Express, 2000. **7**(2): p. 56-67.
28. Kanan, M.W. and D.G. Nocera, *In situ formation of an oxygen-evolving catalyst in neutral water containing phosphate and Co^{2+}*. Science, 2008. **321**(5892): p. 1072-1075.
29. Lutterman, D.A., Y. Surendranath, and D.G. Nocera, *A self-healing oxygen-evolving catalyst.* Journal of the American Chemical Society, 2009. **131**(11): p. 3838-3839.
30. Maissel, L.I. and R. Glang, *Electrical properties of metallic thin films*, in *Handbook of Thin Film Technology*. 1970, McGraw-Hill: San Francisco. p. 1-33.
31. De Faria, D., S. Venâncio Silva, and M. De Oliveira, *Raman microspectroscopy of some iron oxides and oxyhydroxides.* Journal of Raman spectroscopy, 1997. **28**(11): p. 873-878.
32. Beattie, I. and T. Gilson, *The single-crystal Raman spectra of nearly opaque materials. Iron (III) oxide and chromium (III) oxide.* Journal of the Chemical Society A: Inorganic, Physical, Theoretical, 1970: p. 980-986.
33. Van De Krol, R. and M. Grätzel, *Photoelectrochemical Hydrogen Production*. 2012. 75.
34. Dalle Carbonare, N., et al., *Hematite Photoanodes Modified with an Fe^{III} Water Oxidation Catalyst.* ChemPhysChem, 2014. **15**(6): p. 1164 - 1174.
35. Klahr, B., et al., *Electrochemical and photoelectrochemical investigation of water oxidation with hematite electrodes.* Energy and Environmental Science, 2012. **5**(6): p. 7626-7636.

Chapter 8

A transparent water oxidation catalyst for photo-anodes functionalization[1]

In the first part of this chapter, we optimized the deposition parameters of pulsed laser deposition (PLD) and obtained porous coatings of a-Fe_2O_3 formed by very small nanoparticles (~ 5 nm). This morphology resulted in electrodes with enhanced surface area and transmittance. In the second part, we functionalized the surfaces of mesoporous hematite photo-anodes with either compact or porous catalyst and studied the photo-electrochemical properties of the integrated absorber-catalyst system.

8.1 Introduction

An important improvement of the a-Fe_2O_3 nanoparticles assembled coatings studied in the previous chapter would be transmittance enhancement. A recent investigation [1] on hematite optical properties observed a remarkable blue-shift of up to 0.3 eV for both direct and indirect transitions when decreasing an hematite film thickness from 20 to 4 nm, leading to an high degree of transparency in the visible region. The effect is size-dependent and ascribed by the authors to quantum confinement. While reducing hematite dimensions to this level could help alleviate the problem of a very short hole-diffusion length, lying in the nanometer range [2], the resulting low absorption is an issue in the design of photoactive devices based on a single

[1] M. Orlandi, N. Dalle Carbonare, A. Mazzi, Z. El Koura, N. Bazzanella, S. Caramori, N. Patel, C. A. Bignozzi, A. Miotello. *Manuscript in preparation.*

material. This effect can instead be exploited to functionalize an absorber with a transparent iron oxide OER catalyst. In this chapter, we address the issue of parasitic light absorption by taking advantage of the quantum confinement effect to generate transparent coatings of an iron oxide OER catalyst over tin-doped hematite photo-anodes. The choice of iron oxide as both the absorber material and the OER catalyst is motivated by the need to find earth-abundant, cheap and scalable materials to enable the large-scale application of solar water-splitting schemes. Iron oxide not only satisfies all these requisites [3] but it is also non-toxic and environmentally safe.

Capitalizing on the versatility of pulsed-laser deposition, we investigated the response of the optical and electrochemical properties of an iron oxide catalyst to the tuning of film morphology, ranging from a low-transmittance compact layer to a porous nanoparticle-assembled coating, which resulted to be highly transparent. We then functionalized the surfaces of mesoporous hematite photo-anodes with both catalyst morphologies and studied the photo-electrochemical properties of the integrated absorber-catalyst. While the dense film deposition leads to a decrease in photocurrents, photo-anodes decorated with the transparent catalyst show a two-fold increase in photocurrents.

To demonstrate the potential for application of this approach, the transparent catalyst was deposited over a mesoporous hematite photo-anode including a nanometric spin-coated iron oxide underlayer. These kind of electrodes, recently developed in our laboratories [4] exhibit a four-fold improvement in photo-activity over the simple hematite porous film. The integrated photoanode-catalyst yields a photocurrent density of almost 1mA/cm^2 at moderate applied voltage (0.65 vs SCE) in a pH 13.3 solution.

8.2 Experimental

8.2.1 Samples preparation

Amorphous iron oxide (a-Fe_2O_3) pulsed laser deposition

Amorphous iron oxide (a-Fe_2O_3) was deposited by laser deposition technique on commercial (Sigma-Aldrich) quartz, p-type Si substrates, and on Fluorine-doped Tin Oxide (FTO) coated glass slides (FTO, TEC 8 Ω/cm^2, Hartford Glass). Laser ablation was carried out by using a pure (99.9%, Sematrade) Fe target and a KrF excimer laser (Lambda Physik LP 220i) with an operating wavelength of 248 nm, pulse duration of 25 ns, repetition rate of 20 Hz, and laser

fluence of 2.0 J/cm^2. The deposition chamber was evacuated up to a base pressure of 10^{-6} mbar, and then oxygen gas was backfilled into the chamber through a mass flow controller. Three different oxygen pressures were employed, namely: $4.5x10^{-3}$ mbar, $4.5x10^{-2}$ mbar (the same used in the previous chapter), and $4.5x10^{-1}$ mbar. The distance between the metallic iron target and substrates was set to 5.5 cm and the number of pulses was fixed (2000 pulses), to ensure that all samples have the same quantity of material. Substrate temperatures were either room temperature (RT) or 300°C (DEP 300°C). For comparison, some samples were deposited at room temperature and then annealed at 300°C and 550°C in air in a tubular furnace. These are labelled AN300°C and AN550°C respectively. The heating rate was set to 10 °C/min and the desired temperature was kept constant for two hours.

Preparation of hematite photo-anodes (absorbers)

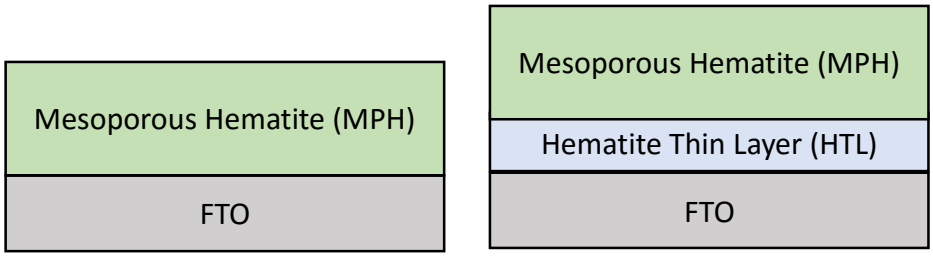

Figure 8.1: Structure of the hematite photo-anodes coupled as absorbers with the PLD deposited catalyst.

The structure of the absorbers coated with the PLD a-Fe_2O_3 catalyst is shown in *figure 8.1*.

Substrate pretreatment. Fluorine-doped Tin Oxide glass slides (FTO, TEC 8 Ω/cm^2, Hartford Glass) were cleaned by successive 30 minutes ultrasonic treatments in acetone, ethanol, aqueous Alconox® (Sigma Aldrich) solution and distilled water and then blown dry with a warm air stream. A portion of the slides was then masked with KAPTON tape (Tesa) to preserve an uncovered zone for the electric contact.

α-Fe_2O_3 thin underlayer (HTL) deposition. $FeCl_3 \cdot 6H_2O$ (0.54 g) was dissolved in DI water (20 mL) and then Polyethyleneglycol Bisphenol A Epichlorohydrin Copolymer (0.54 g) was added under gentle stirring to avoid the formation of bubbles. The solution was spin coated onto FTO glass (1000 rpm for 9 seconds and 2000 rpm for 30 seconds) with a KV-4A Spin Coater (Chemat Technology). After every spin coating cycle the glass slide was annealed at 550 °C for 15 minutes in air. Spin coating cycles were repeated for 3 times. $FeCl_3 \cdot 6H_2O$ (≥99%) was purchased from Alfa Aesar and Polyethyleneglycol Bisphenol A Epichlorohydrin Copolymer (mol wt 15000-20000 Da) from Sigma Aldrich.

Mesoporous α-Fe_2O_3 film (MPH) deposition. Mesoporous α-Fe_2O_3 was electrophoretically deposited on either FTO glass or on HTL samples following a literature procedure [5] by applying 10 V to either FTO or HTL samples immersed in a colloidal suspension of hydrothermally grown Fe_2O_3 nanoparticles. The electrodes were then annealed first at 550 °C for 2 hours to obtain crystalline hematite and then activated at 800 °C for 20 minutes in air.

A more detailed description of the synthetic procedures for HTL and MPH can be found elsewhere [4].

8.2.2 Characterization

Scanning electron microscopy (SEM) was used to analyse the morphology and the thickness of the films deposited on silicon substrates. Measurements were performed using a JEOL JSM-7001F FEG-SEM at 20.0 keV electron beam energy. The SEM apparatus is equipped with an Energy Dispersive X-ray Spectroscopy detector (EDXS, Oxford INCA PentaFETx3). Working distance was maintained between 3 to 8 mm. Surface morphology images were acquired in top-down and tilted mode whereas cross section analysis were performed putting the films on a 90° stub.

Raman measurements were performed on a Horiba LabAramis setup equipped with a HeNe 633 nm laser as source and a confocal microscope (100x objective) coupled to a 460 mm-focal length CCD-based spectrograph equipped with a four interchangeable gratings-turret. In the range between 450 nm and 850 nm, the wavenumber accuracy is 1 cm^{-1} with a 1800 l/mm grating. The laser power is 15 mW and the maximum spot size is 5 μm. An accumulation number of 10 and an exposure time of 7 s were employed for all measurements.

UV-Vis absorption of the samples deposited on quartz substrates was studied using a Varian Cary 5000 spectrophotometer.

XPS was performed using a PHI 5000 VersaProbe II equipped with a mono-chromatic Al Ka (1486.6 eV) X-ray source and a hemispherical analyser. Electrical charge compensation was required to perform the XPS analysis. The sample surface was sputtered for 30 sec in order to remove any surface oxidation.

Electrochemical measurements were performed on an Eco Chemie Autolab PGSTAT 302/N work-station in a 1 M KOH (98%, Alfa Aesar) solution (pH 14) using a three electrodes configuration cell with a platinum and a Saturated Calomel Electrode (SCE, +0.241 V Vs RHE) as counter and reference electrode respectively. J/V curves were recorded with a scan speed of

10 mV s^{-1} scanning the potential from 0 to 1.5 V vs SCE. For photo-electrochemistry experiments the cell was coupled to an ABET solar simulator (AM 1.5G, 100 mW/cm^2). The working electrode was irradiated from the FTO side and the illuminated area was 1 cm^2. In this case, J/V curves were recorded in a 0.1M NaOH (98%, Alfa Aesar) solution (pH 13.3).

8.3 Results and discussion

8.3.1 XPS characterization

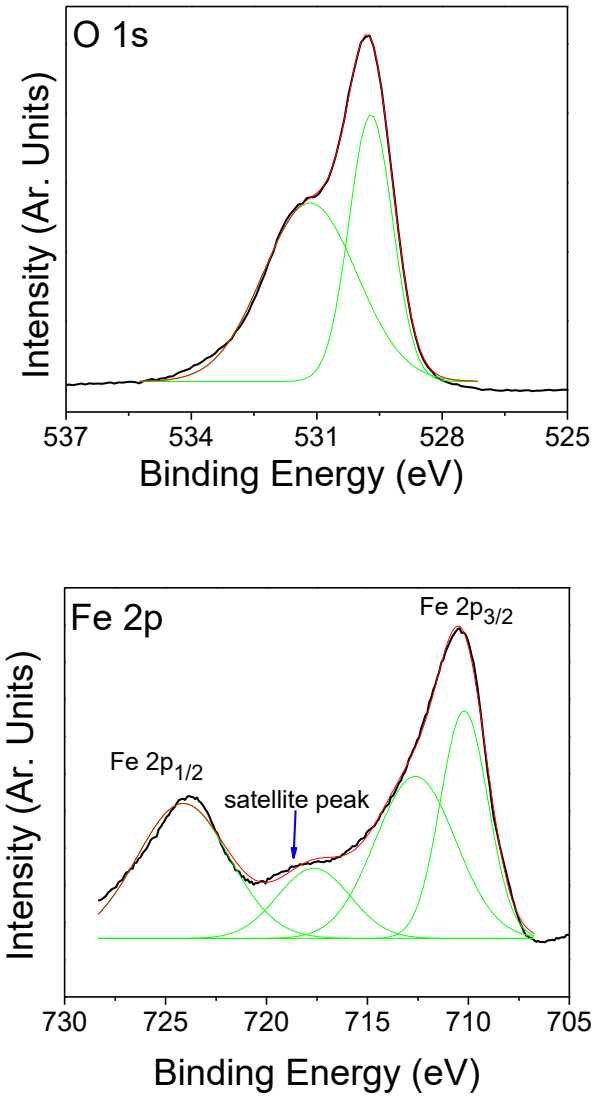

Figure 8.2: XPS peaks for O 1s (top) and Fe 2p (bottom) for RT samples.

XPS analysis on samples deposited at different oxygen pressure and substrate temperature reveals the presence of iron only as Fe(III) confirming the identification as Fe_2O_3. *Figure 8.2* presents, as an example, the XPS spectra of the sample deposited at room temperature (RT) and high pressure ($4.5x10^{-1}$ mbar). The O-1s core level was fitted with two peaks (*figure 8.2*, top).

The main peak is at BE = 529.8 ± 0.5 eV and is generally associated to metal oxides. The second peak, at BE = 531.4 ± 0.5 eV, is associated to metal carbonates. Fe 2p core level was fitted by four peaks (*figure 8.2*, bottom). The peaks at 723.7 and 710.2 eV are attributed to Fe $2p_{1/2}$ and Fe $2p_{3/2}$ of Fe_2O_3 phase, respectively. The satellite peak at 718 eV further confirms the identification of Fe_2O_3 phase [6]. The peak at 712.6 eV is difficult to understand, we suspect it might be due to Fe hydroxide.

8.3.2 SEM characterization

Effect of deposition pressure on films morphology

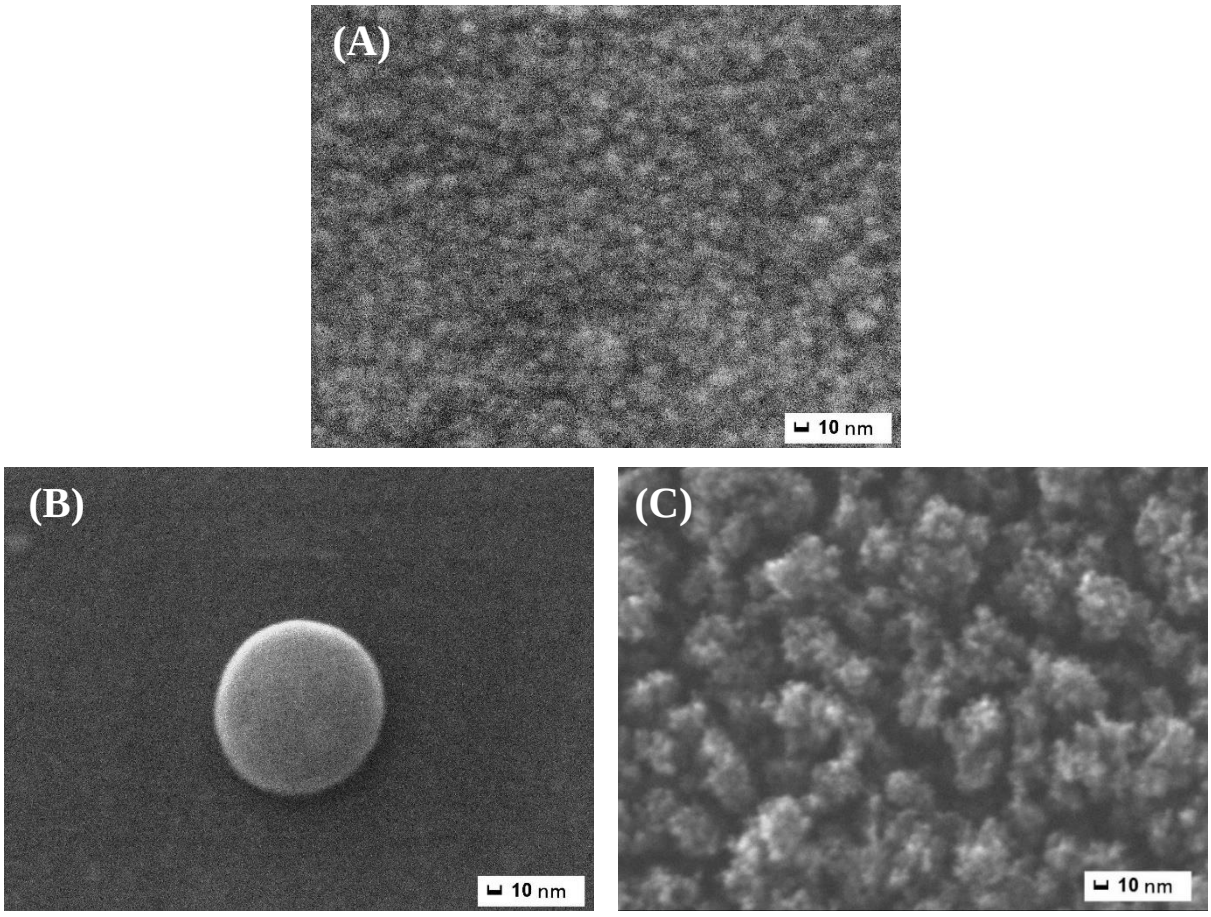

Figure 8.3: SEM top-down images showing the morphology change with oxygen pressure: (A) $4.5x10^{-2}$ mbar; (B) $4.5x10^{-3}$ mbar; (C) $4.5x10^{-1}$ mbar. All samples were deposited at room temperature.

Scanning electron microscopy images of films deposited at RT with different oxygen pressure are shown in *figure 8.3*. Films deposited at $4.5x10^{-2}$ mbar are formed by nanoparticles with average size of 10-15 nm (*figure 8.3*-A), as we have seen in previous chapter. Decreasing the pressure by one order of magnitude ($4.5x10^{-3}$ mbar) results in compact films, with some big nanoparticles (>60 nm) on the surface (*figure 8.3*-B). By contrast increasing the oxygen

pressure ($4.5x10^{-1}$ mbar), results in very porous flakes like structure (*figure 8.3*-C). In this case SEM analysis reveals a complex morphology with scattered particles of diameter in the range of about 30-300 nm and inhomogeneous size-distribution covered by a porous structure made of smaller particles assembled in irregular wires. As the size of these latter particles approaches the spatial resolution of the SEM apparatus (2 nm), a conservative estimate for their average diameter is 5 ± 2 nm. *Figure 8.4* shows cross section images, of the same sample, at different magnifications. Due to the very rough morphology, it is not possible to define a layer thickness but surface coverage appears to be complete.

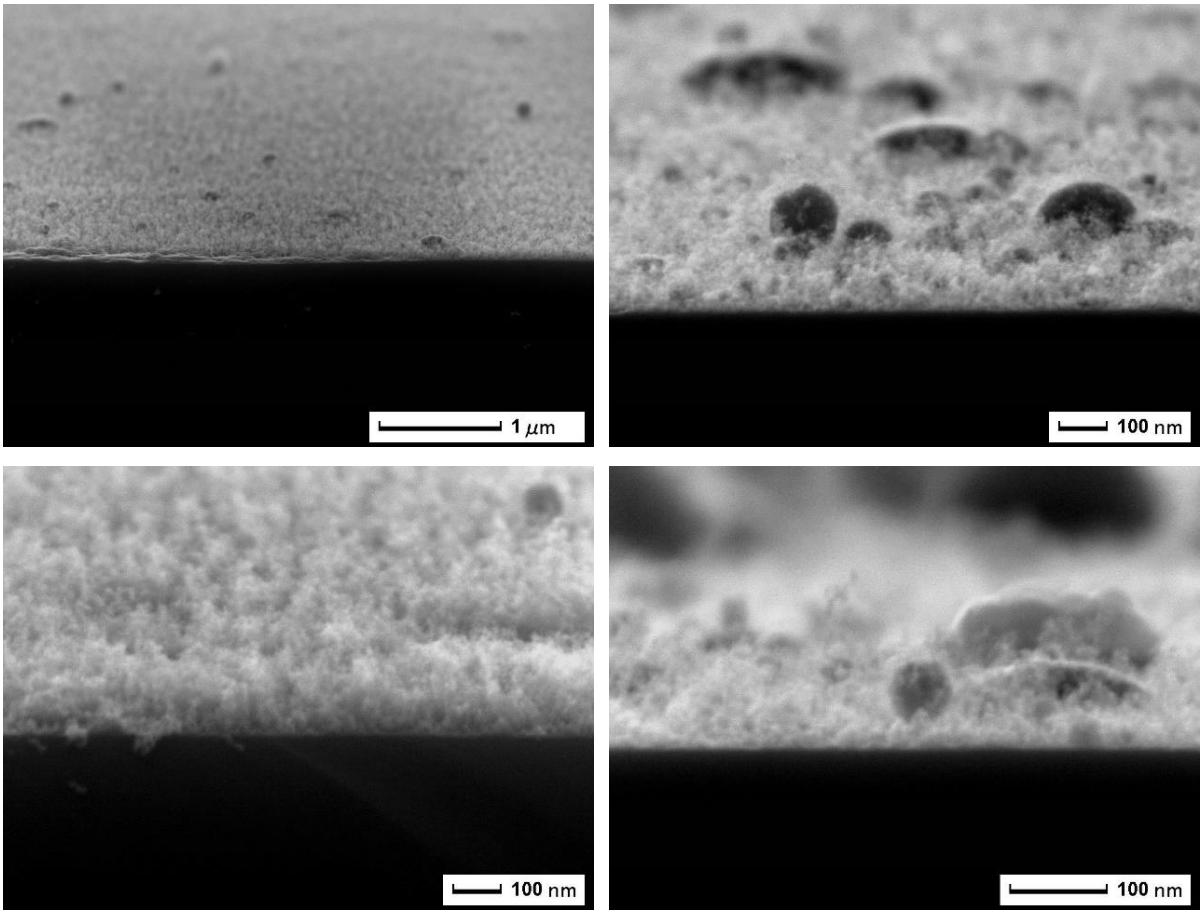

Figure 8.4: SEM cross-section images at various magnifications.

In the case of high-pressure depositions, the oxygen atmosphere reduces the kinetic energy of the ablated material, limits the plume expansion, and promotes collisions between ablated particles, resulting in the formation of nanoclusters in the plasma plume, which are stabilized and slowed down by the background gas before reaching the substrate, where they create a porous structure. By contrast, in low-pressure conditions, the plume expansion is less limited, the ablated material retains a higher kinetic energy and the higher mobility allows aggregation

of the particles after deposition on the substrate. The result is a more dense microstructure composed of partially fused NPs [7, 8]. The structure obtained at high pressure is very interesting for our application because it provides a very high surface area, which is beneficial for catalysis. Therefore, all the samples considered hereafter were deposited at 4.5 $x10^{-1}$ mbar.

Effect of post annealing and deposition temperature

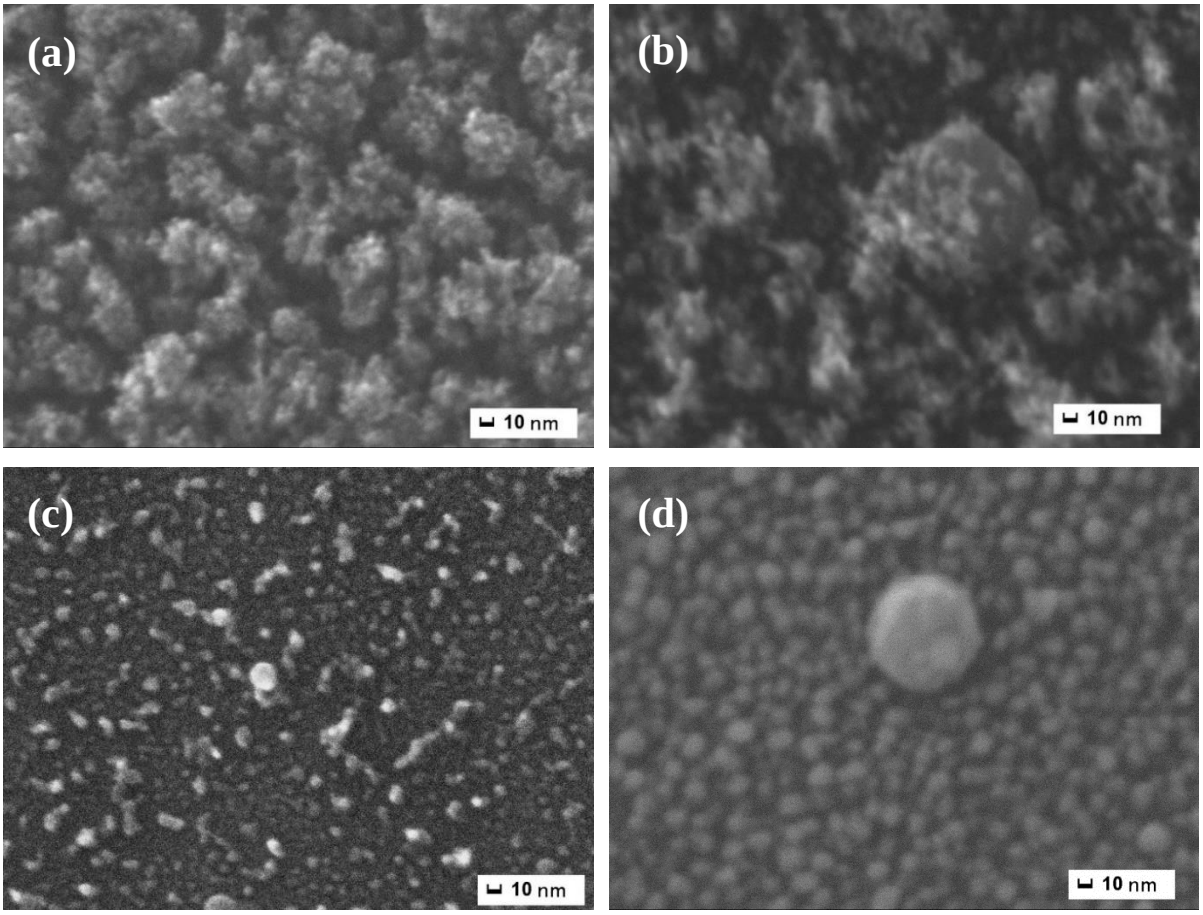

Figure 8.5: Top view SEM analysis of: (a) RT, (b) AN 300°C (c) AN 550°C and (d) DEP 300°C. Substrate is silicon for all samples.

Annealing of RT at 300 °C results in a partial collapse of the porous structure by aggregation of the smaller particles (*figure 8.5*-b), which becomes complete with annealing at 550 °C (*figure 8.5*-c).

Deposition with the substrate heated at 300°C results in a more compact NPs-assembled layer (*figure 8.5*-d) similar to the structures typical of lower deposition pressures [9]. This effect is due to the higher mobility of the particles when they hit the heated substrate, leading to aggregation and the formation of bigger and partially-fused particles, mostly of diameter > 10 nm. A comparison between the porous structure of RT film and the compact DEP 300 sample is presented in *figure 8.6.*

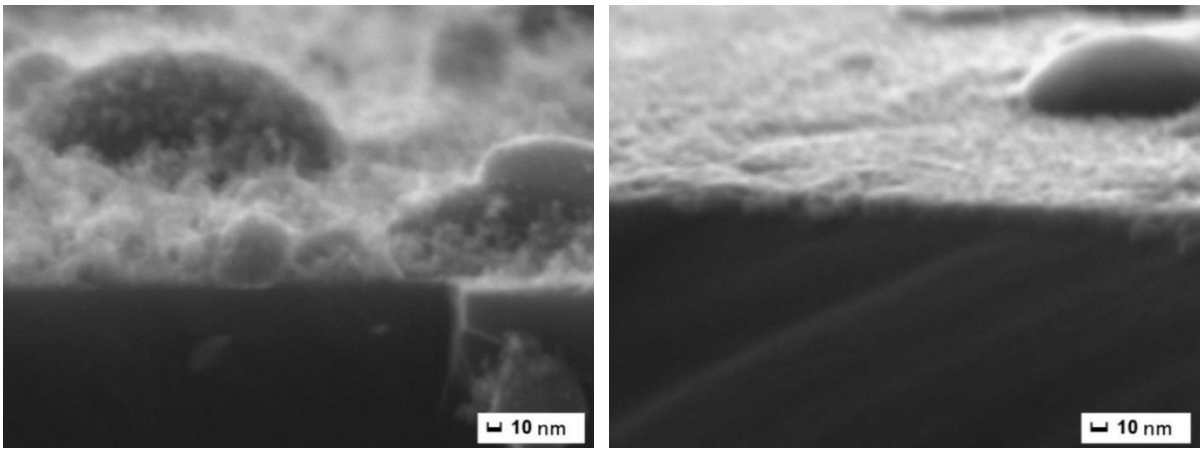

Figure 8.6: Cross-section SEM analysis of samples RT (left) and DEP 300°C (right) on Si substrates.

8.3.3 Raman characterization

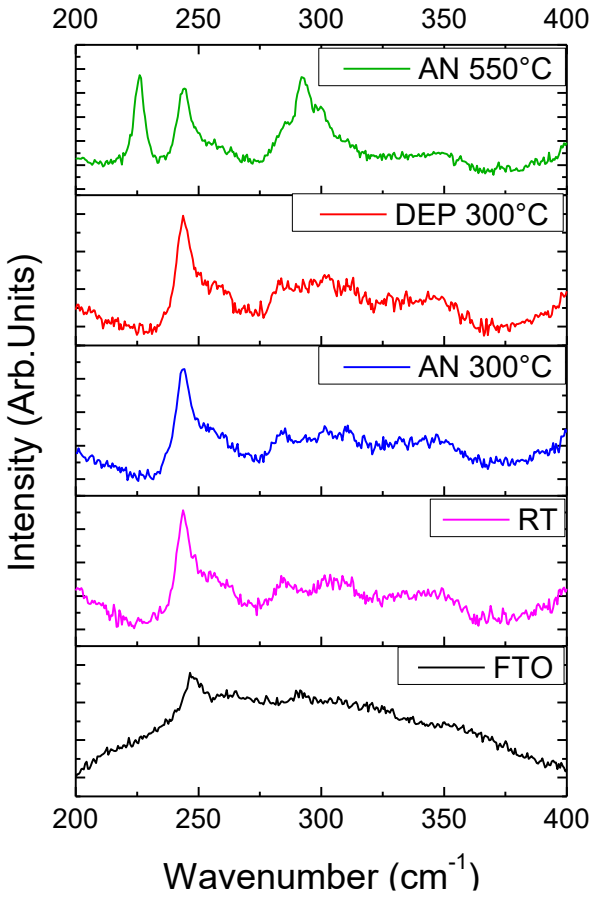

Figure 8.7: Raman spectra of iron oxide NPs-assembled coatings deposited by PLD on FTO coated glass substrates. Bare FTO spectrum is reported for comparison.

Raman analysis (*figure 8.7*) reveals the presence of the crystalline hematite main peaks [10] at 226 and 292 cm^{-1} only in the case of the sample annealed at 550°C. All other samples show spectra with features not clearly different from the FTO reference. This is an indication of the largely amorphous nature of the deposited material, which is known to yield better OER catalysis performance than the crystalline phase [11].

8.3.4 Optical characterization

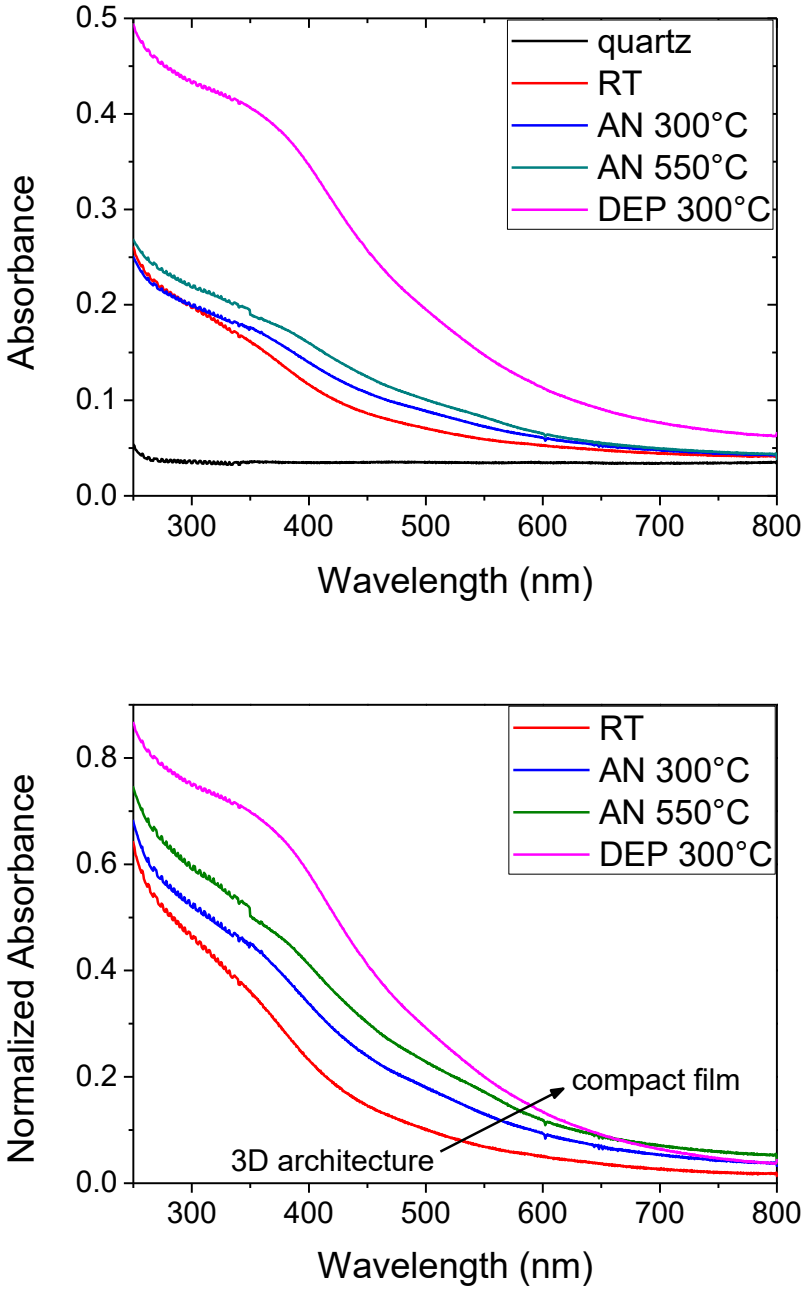

Figure 8.8: UV-Vis absorption spectra on quartz substrates, normalized version on the right.

From the analysis of UV-Vis absorption spectra on quartz substrates (*figure 8.8*), three important observations emerge:

1. the sample DEP 300°C shows a much higher absorbance in all the investigated range;
2. the absorbance correlates with morphology in the direction of higher values for more compact films
3. the absorption band edge is markedly blue-shifted for RT, as more evident in the normalized spectra on the right graph (*figure 8.8*, right).

Given that the quantity of deposited material at a given pressure is essentially set by the number of pulses, which is kept constant for all depositions, the difference between RT and DEP 300°C is all the more striking. The reason for this behavior probably lies in the different morphology of the films. While DEP 300°C is essentially a bidimensional thin-film, although with a nanostructured surface, RT exhibits a tridimensional architecture with scattered big particles and a substantial fraction of the material composed of very small particles (5±2 nm). In this latter case, a reasonable hypothesis, supported by the blue-shift of the absorption onset, is that a size effect in the form of optical quantum confinement dominates the optical properties, as reported for other materials [12] and for other nanosized hematite [13, 14].

8.3.5 Photo-electrochemical characterization

Since Fe_2O_3 is stable in alkaline environment (pH >9.8) [15], electrochemical water oxidation experiments were performed at pH=14 (KOH 1M) to ensure a well-defined electrochemistry. Oxygen evolution at this pH is expected at potential $E(O_2/H_2O) = 1.23 - (0.059pH) = 0.40$ V versus reversible hydrogen electrode (RHE) [16]. *Figure 8.9* illustrates the current responses of all iron-modified samples along with an FTO reference. The linear scan reveals that all samples are active towards water oxidation, with both DEP 300°C and AN 300°C showing considerable electroactivity with overpotentials (taken at current density J = 0.2 mA/cm^2) of 408 and 433 mV, respectively. However, the current response of RT decreased considerably in a 60 minutes chronoamperometry experiment at 1V vs RHE, designed to test stability closer to operational conditions (*figure 8.9*, right). The current density loss for RT is of 44%, while DEP 300°C is substantially stable with only a 6% loss. AN 300°C shows an intermediate stability with a 11% decrease, close to the 10% of AN 550°C. In the case of RT, the performance degradation is irreversible and is due to detachment of active material, as observed by SEM images taken after prolonged electrocatalysis (*figure 8.10*).

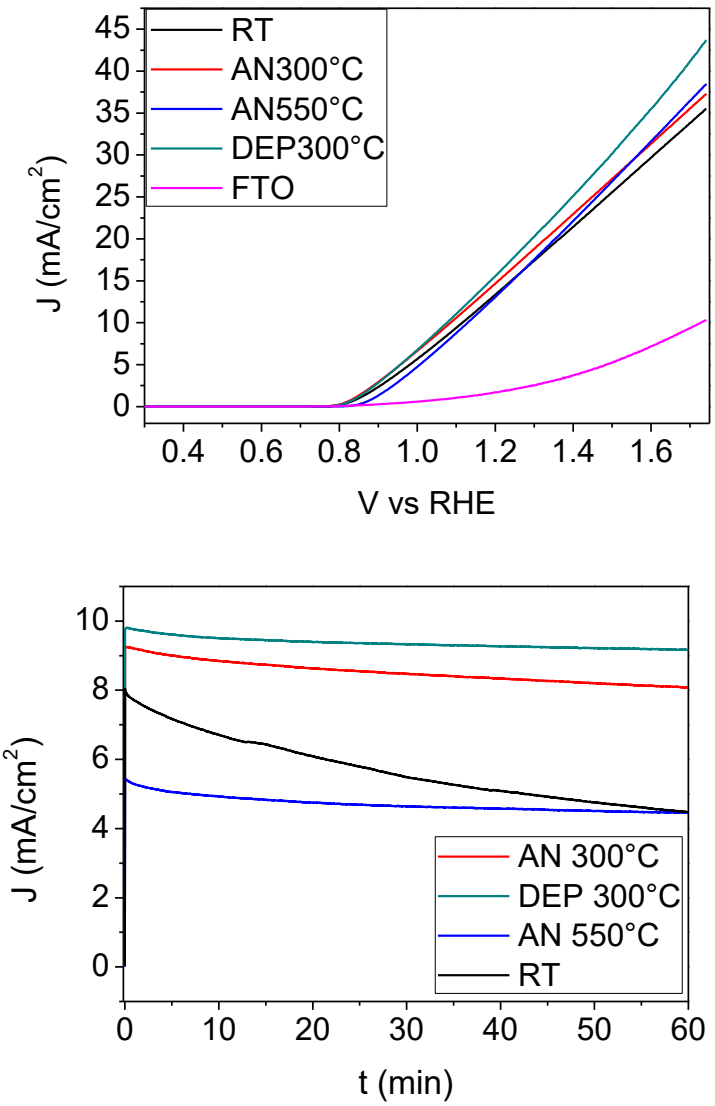

Figure 8.9: Linear sweep voltammetry on FTO substrates (left) and chronoamperometry at 1V vs RHE (right).

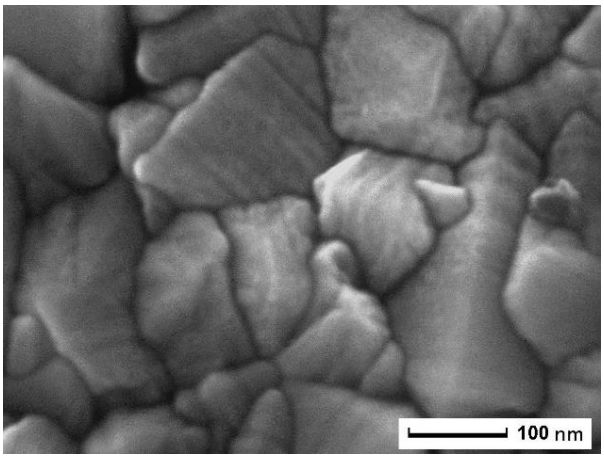

Figure 8.10: Top-down SEM imaging of RT after electrocatalysis. The morphology is typical of FTO and no NPs are present.

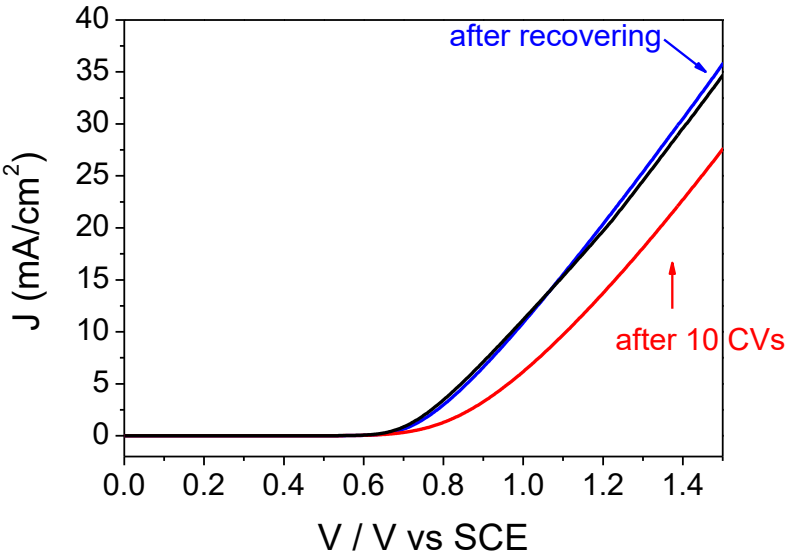

Figure 8.11: Current response of AN 300°C, initial (black), after 10 CV cycles (red) and after restoring the electrode (blue).

Conversely, the initial performance of AN 300°C was reobserved on successive JV scans (*figure 8.11*) after restoring the electrode by abundant rinsing with water and heating at 80°C in air for 2 hr. In this case, the current decrease during electrolysis may originate by adsorption of molecular oxygen, ions and oxidation intermediates, limiting the active surface of the electrode, rather than by detachment of a-Fe_2O_3. From an electrocatalysis point of view, DEP300°C is the best electrode, with J = 41.2 mA/cm^2 at 1.7 V vs RHE, while AN550°C is limited to 36 mA/cm^2 at same potential value, confirming that the amorphous material is a better catalyst than crystalline hematite, as reported by recent literature [11, 17].

These findings indicate that the more compact NPs-assembled film of DEP 300°C is better for electrocatalysis due to both a higher stability and improved performance. However, when integrated over an FTO/MPH photoanode the effect on photocurrent is detrimental (*figure 8.12*, left). By contrast, functionalization with AN 300°C, selected as the best compromise between stability and transparency, leads to a roughly two-fold increase in photocurrents in all the explored range (*figure 8.12*, right), accompanied by a shift of the current onset towards more negative potentials.

A similar improvement of performance is obtained by functionalization of FTO/HTL/MPH as reported in *figure 8.13*. In this case, while the increase in photocurrent density is less pronounced, the negative shift of the onset potential is up to 80-90 mV. The functionalized photoanode yields a current of almost 1 mA/cm^2 at moderate applied voltage (0.89 V vs RHE).

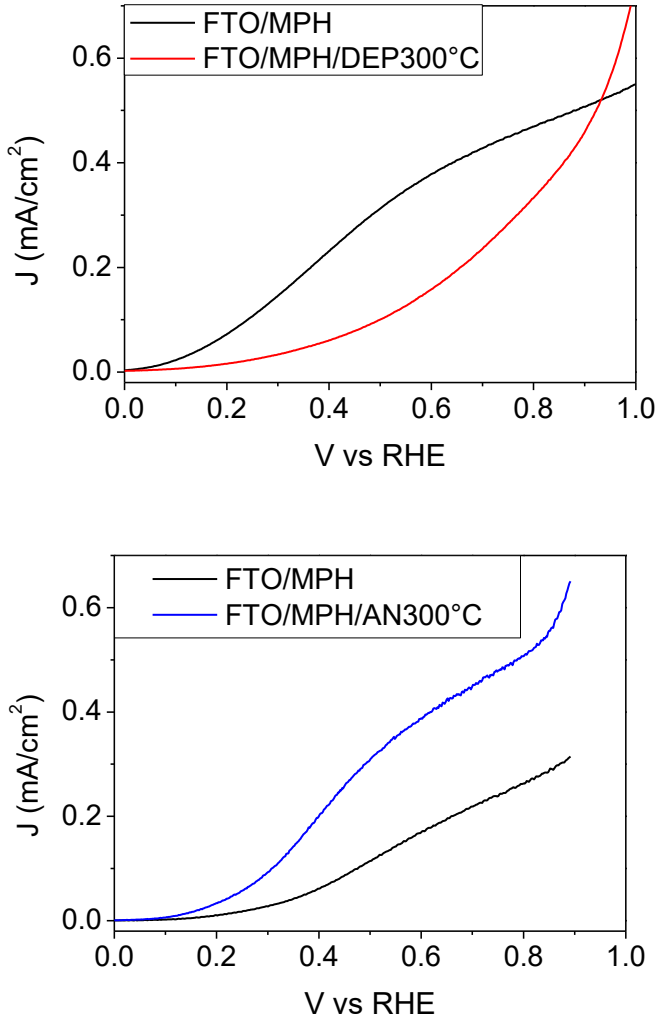

Figure 8.12: Photocurrent response of FTO/MPH/DEP300°C (left) and FTO/MPH/AN300°C (right) in NaOH 0.1 M (pH 13.3).

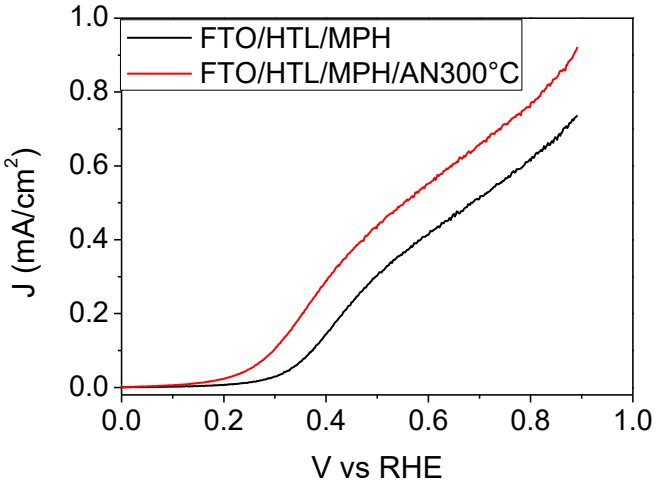

Figure 8.13: Photocurrent response of FTO/HTL/MPH/AN300°C in NaOH 0.1 M (pH 13.3).

8.4 Conclusions

Reducing the dimensions of an iron oxide OER catalyst to induce optical quantum confinement is proved to be a feasible strategy to obtain transparent coatings, which retains their activity but are unstable under electrocatalysis conditions. A simple low-temperature thermal treatment was found to improve stability enough for the successful application of catalyst coatings to hematite photoanodes, resulting in a substantial increase in the photocurrents detected in a photoelectrochemical cell. By contrast, functionalization of the photoanodes with a more compact catalyst thin-film, exhibiting better stability and performance in electrocatalysis but also a higher absorbance, leads to a decrease in photocurrents. These findings offer a strategy to circumvent the problem of parasitic light absorption in integrated absorber-catalyst photoelectrodes, currently limiting the development of solar water splitting devices, and opens up the possibility to employ higher mass-loadings of catalyst, which would be beneficial especially for earth-abundant, cheap and scalable materials such as iron oxides.

To further demonstrate the potential for application of this approach, the transparent catalyst was deposited over an optimized hematite photoanode including a nanometric spin-coated iron oxide underlayer. The catalyst application improves performance by both inducing a substantial (80-90 mV) negative shift of the photocurrent onset and by increasing the photocurrent density over all the explored range. This integrated absorber-catalyst photoanode yields a current of almost 1 mA/cm^2 at moderate applied voltage (0.89 V vs RHE, pH 13.3). This result is a step forward towards an all-iron based photoanode efficient enough for application. PLD, an easily scalable fabrication technique already applied in a variety of industrial processes [18], proves to be a versatile method to control morphology at a nanometric scale, thus allowing a systematic investigation of its effect on materials properties.

Further work will be aimed at solving the stability problem of the most transparent RT structures without resorting to the post-deposition thermal treatment, by e.g. exploring deposition temperatures lower than 300°C, and at extending the methodology to more intrinsically-active species like mixed-metal oxides.

8.5 References

1. Fondell, M., et al., *Optical quantum confinement in low dimensional hematite.* Journal of Materials Chemistry A, 2014. **2**(10): p. 3352.
2. Klahr, B.M., A.B. Martinson, and T.W. Hamann, *Photoelectrochemical investigation of ultrathin film iron oxide solar cells prepared by atomic layer deposition.* Langmuir, 2011. **27**(1): p. 461-8.
3. Vesborg, P.C.K. and T.F. Jaramillo, *Addressing the terawatt challenge: scalability in the supply of chemical elements for renewable energy.* RSC Advances, 2012. **2**(21): p. 7933.
4. Dalle Carbonare, N., et al., *Improvement of the electron collection efficiency in porous hematite using a thin iron oxide underlayer: towards efficient all-iron based photoelectrodes.* Physical Chemistry Chemical Physics, 2015. **17**(44): p. 29661-29670.
5. Zong, X., et al., *A Scalable Colloidal Approach to Prepare Hematite Films for Efficient Solar Water Splitting.* Phys. Chem. Chem. Phys. , 2013. **15**: p. 12314-12321.
6. Yamashita, T. and P. Hayes, *Analysis of XPS spectra of Fe^{2+} and Fe^{3+} ions in oxide materials.* Applied Surface Science, 2008. **254**(8): p. 2441-2449.
7. Infortuna, A., A.S. Harvey, and L.J. Gauckler, *Microstructures of CGO and YSZ thin films by pulsed laser deposition.* Advanced Functional Materials, 2008. **18**: p. 127 - 135.
8. Petrov, I., et al., *Microstructural evolution during film growth.* Journal of Vacuum Science and Technology A, 2003. **21**: p. S117 - S128.
9. Orlandi, M., et al., *Pulsed-laser deposition of nanostructured iron oxide catalysts for efficient water oxidation.* ACS Appl Mater Interfaces, 2014. **6**(9): p. 6186-90.
10. Jubb, A.M. and H.C. Allen, *Vibrational Spectroscopic Characterization of Hematite, Maghemite, and Magnetite Thin Films Produced by Vapor Deposition.* ACS Applied Materials & Interfaces, 2010. **2**(10): p. 2804-2812.
11. Smith, R.D., et al., *Photochemical route for accessing amorphous metal oxide materials for water oxidation catalysis.* Science, 2013. **340**(6128): p. 60-3.
12. Raymand, D., et al., *Investigation of Vibrational Modes and Phonon Density of States in ZnO Quantum Dots.* The Journal of Physical Chemistry C, 2012. **116**(12): p. 6893-6901.
13. K. Sivula, R.Z., F. Le Formal, R. Robert, A. Weidenkaff, J. Tucek, J. Frydrych and M. Gratzel, *Photoelectrochemical Water Splitting with Mesoporous Hematite Prepared by a Solution-Based Colloidal Approach.* J Am Chem Soc, 2010. **132**: p. 7436-7444.

14. L. Vayssieres, C.S., S. M. Butorin, D. K. Shuh, J. Nordgren and J. Guo, *One-Dimensional Quantum-Confinement Effect in α-Fe_2O_3 Ultrafine Nanorod Arrays.* Adv Mater, 2005. **17**: p. 2320-2323.
15. Cristino, V., et al., *Efficient solar water oxidation using photovoltaic devices functionalized with earth-abundant oxygen evolving catalysts.* Phys Chem Chem Phys, 2013. **15**(31): p. 13083-92.
16. Krol, R., *Principles of Photoelectrochemical Cells.* 2012. **102**: p. 13-67.
17. Smith, R.D., et al., *Water oxidation catalysis: electrocatalytic response to metal stoichiometry in amorphous metal oxide films containing iron, cobalt, and nickel.* J Am Chem Soc, 2013. **135**(31): p. 11580-6.
18. Gower, M.C., *Industrial applications of laser micromachining.* Optics Express, 2000. **7**(2): p. 56-67.

Conclusions

Hydrogen production by solar water splitting technology could play a critical role in the transition to a clean and sustainable energy future. This is subordinate to the construction of efficient and stable photo-electrodes based on earth abundant, cheap and biocompatible materials. In this thesis, we studied different processes to improve the performance of TiO_2 and Fe_2O_3.

TiO_2 has excellent characteristics as a photo-catalyst, but its performance is limited by two main shortcomings, i.e. wide band gap and fast recombination of charge carriers.

Codoping TiO_2 with V and N (4 at.% and 2 at.%, respectively) causes an effective narrowing of the band gap to 2.5 eV, because the incorporation of dopants forms isolated energy levels inside the band gap. The dopants, at low concentration, act as traps for photo-excited holes or electrons thus enhancing the separation of electron-hole pair that is also favoured by the charge separation operated at the interface between V-N-codoped TiO_2 and ITO because of the relative positions of the bottom conduction band of the two layers. The synergistic effects created by band narrowing and enhanced charge separation, by using multilayer structure and codoping strategy, resulted in improved photo-catalytic activity of V-N codoped TiO_2 as compared to pure and single mono-doped TiO_2 films.

Mesoporous ITO/TiO_2 electrodes were successfully prepared by a single RF-sputtering process, without any further processing. The electrodes resulted composed by a compact ITO layer, tapered with rod-like ITO nanocrystals on which cauliflower-like TiO_2 structure in anatase crystalline phase were grown. Electrochemical characterization revealed that electrodes resulted optimal in charge transfer since they offer an elevated interface between the ITO and the TiO_2, making them appealing for electrochemical applications.

A successful method for converting amorphous TiO_2, generally easy to synthesize, into H-doped anatase TiO_2 by a mild annealing in hydrogen atmosphere was developed. H-doped TiO_2

electrodes presented an enhanced photocatalytic activity with respect to anatase TiO_2 thin-films, which was ascribed to the dangling bonds passivation made by H atoms, which reduces the density of recombination centers.

Codoping TiO_2 with Cu and N caused only a slight increase in visible light absorption. An enhancement of the reduction reaction and a concomitant weakening of the oxidation reaction was observed. This behaviour was explained by the change of the electrical properties of the films, namely from n-type (pure TiO_2) to p-type semiconductor (Cu-N TiO_2).

Future work will be aimed at depositing codoped films with a higher content of nitrogen. Indeed, it was reported in literature that nitrogen doping is efficient in the range 3-4 at.%.

Fe_2O_3 was studied for the functionalization of absorbers surfaces. For this application, the low absorbance of iron oxide becomes an advantage and the low diffusion length of holes is not an issue if the film is sufficiently thin and nanostructured. Amorphous iron oxide nanoparticles assembled coatings were synthesized by pulsed-laser deposition (PLD) for functionalization of indium−tin oxide (ITO) surfaces, resulting in electrodes capable of efficient catalysis in water oxidation. These electrodes, based on earth-abundant and non-hazardous iron metal, were able to sustain high current densities (up to 20 mA/cm^2) at reasonably low applied potential (1.64 V at pH 11.8 versus reversible hydrogen electrode) for more than 1 h when employed as anodes for electrochemical water oxidation. Subsequently, the response of the optical and electrochemical properties of the coating to the tuning of film morphology was studied, ranging from a low-transmittance compact layer to a porous nanoparticles-assembled coating, which resulted to be very transparent. The functionalization of hematite absorbers with the compact catalyst thin-film, exhibiting better stability and performance in electrocatalysis but also a higher absorbance, lead to a decrease in photocurrents. By contrast, functionalization of the same absorber with the porous and more transparent coating enhanced substantially the performance of the photoelectrode. This integrated absorber-catalyst photoanode yielded a current of almost 1 mA/cm^2 at moderate applied voltage (0.89 V vs RHE, pH 13.3).

These findings offer a strategy to circumvent the problem of parasitic light absorption in integrated absorber-catalyst photoelectrodes, currently limiting the development of solar water splitting devices, and opens up the possibility to employ higher mass-loadings of catalyst, which would be beneficial especially for earth-abundant, cheap and scalable materials such as iron oxides. Further work will be aimed at extending the methodology to more intrinsically-active species like mixed-metal oxides.

Appendix A

Deposition techniques

In this section, the two main deposition techniques used to prepare the samples studied in this thesis will be presented: radio frequency magnetron sputtering and pulsed laser deposition. Both techniques are based on physical vapour deposition (PVD) processes used for depositing thin films on a variety of substrates. The energetic nature of both processes ensures a good adhesion of the deposited material. Both techniques are widely used for industrial applications and in the field of materials science because they are very versatile and allow a precise control of the properties of deposited films, they have a very high reproducibility and they pose very less constraints on the usable materials as targets and substrates.

A.1 Radio Frequency Magnetron Sputtering

Sputtering is a process whereby atoms are ejected from a solid target material due to bombardment of the target by energetic ions (*figure A.1*). In sputtering deposition the ions are generate in a plasma, formed by ionization process of a neutral gas. The incident ions set off collision cascades in the target. When such cascades recoil and reach the target surface with an energy greater than the surface binding energy, an atom would be ejected. The simplest sputtering system consist in an anode (substrate) and a cathode (target) loaded into a vacuum chamber. The basic process is as follows. The pressure in the deposition chamber is decreased up to ~ 10^{-7} mbar (high vacuum). A working gas (generally Argon) is introduced into the vacuum chamber, where it is weakly ionized by cosmic radiation. When a high potential difference (of the order of 100V) is applied between the target and the substrate, the electrons in the gas accelerate and ionize neutral Ar atoms. The as formed ions are accelerated towards the target and collide with the other atoms and ions in the chamber, giving rise to emission of

secondary electrons. The secondary electrons are again accelerated by the applied voltage, and in turn ionize others atoms, so that the plasma is self-sustained.

For efficient momentum transfer, the atomic weight of the sputtering gas should be close to the atomic weight of the target, so for sputtering light elements neon is preferable, while for heavy elements krypton or xenon are used. The atoms ejected from the target travel some distance until they reach the substrate and start to condense into a film. As more and more atoms coalesce on the substrate, they begin to bind to each other at the molecular level, forming the film. Sputtered atoms ejected from the target have a wide energy distribution, typically up to tens of eV (100,000 K).

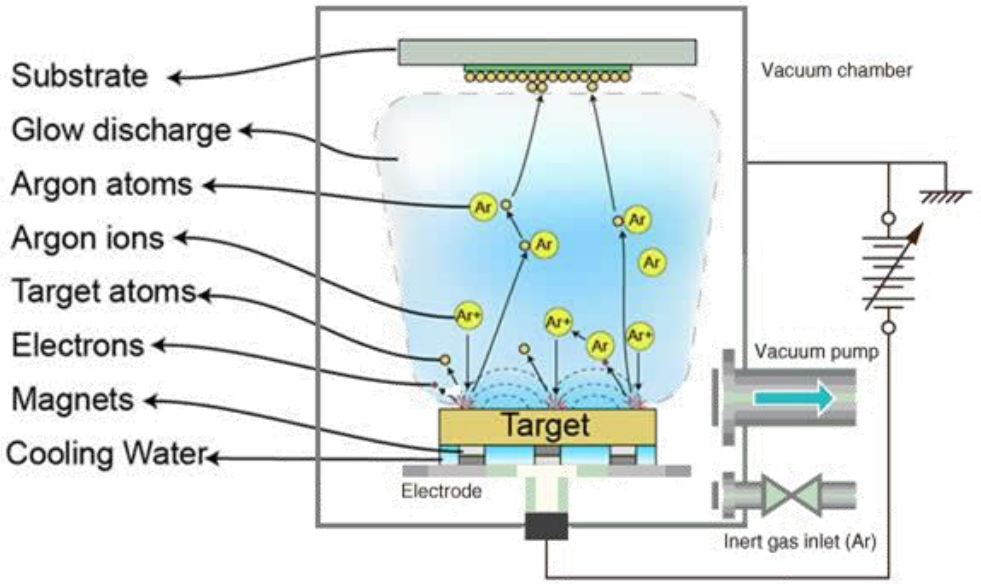

Figure A.1: Scheme showing the basic components of a magnetron sputtering system.

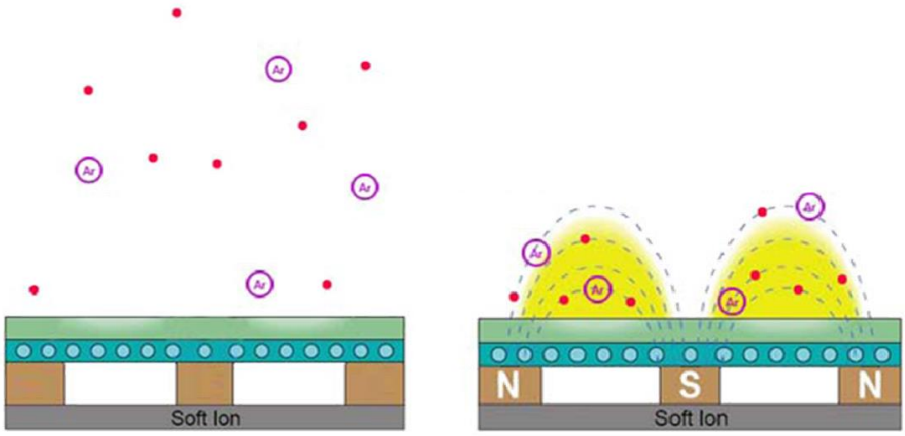

Figure A.2: Comparison between a sputtering system and a magnetron sputtering system.

Sputtering can be done either in direct (DC) or radio frequency (RF) modes. DC power supplies are generally used for conducting targets where the high conductivity of the materials prevents

the accumulation of electric charge on their surface. If the target is a non-conducting material the positive charge will build up on its surface and will hinder argon ions from reaching the target, thus stopping the sputtering process. This can be avoided using a Radio Frequency power supply, which varies the sign of the anode-cathode bias at a high rate compensating the charge after each period. For RF sputtering it is necessary an automatic or manual impedance matching network between the power supply and the sputtering gun. The radio frequency used is 13.56 MHz. RF sputtering can be done for both conducting and non-conducting materials. With RF sputtering a higher sputter rate at lower pressure is obtained. Sputtering sources are usually magnetrons that utilize strong magnetic fields to trap electrons close to the surface of the target (*figure A.2*). Moreover, the electrons traveling in the magnetic field are forced to spiral along flux lines near the target, increasing the probability of further ionizing argon atoms. This generates a stable plasma with a high density of ions. More ions means more ejected atoms from the target, that is, increased sputtering efficiency. The faster ejection rate, and hence deposition rate, minimizes impurities formation in the thin film, and the increased distance between plasma and substrate limits the damages caused by stray electrons and argon ions on the thin film being formed. As the target material is depleted, a "racetrack" erosion profile may appear on its surface. The sputtered atoms are neutrally charged and so are unaffected by the magnetic trap.

For a more detailed description of the principles behind the sputtering process and technical reviews of the current state of the art see [1, 2].

A.1.1 Deposition parameters

The properties of the deposited film depend the RF power used, on the sample-target distance, on the substrate temperature, and on the deposition pressure. The availability of many parameters that control sputter deposition makes it a complex process, but also provides a large degree of control over the growth and microstructure of the film. Two fundamental parameters are the deposition pressure and the substrate temperature. In 1974 Thornton published a “structure zone model” that illustrates the dependence of the deposit morphology from these two parameters [3]. The substrate temperature affects the mobility of the particles reaching the substrate. The temperature of the substrate is important because it affects the crystallinity and the crystal phase of the film and thus its morphological and optical properties. Good crystalline films are usually obtained at higher temperatures, while low temperature often produces an amorphous film. The deposition pressure governs, via the mean free path, the energy

distribution with which they impinge on the surface of the growing film. The collision of sputtered atoms (only a small fraction – order 1% – of the ejected particles are ionized) with the gas particles results in deflection of their trajectory. At low pressures the probability of these collisions is low and most of the sputtered material flies in straight lines and impacts energetically on the substrate (ballistic range), sometimes causing re-sputtering, i.e. re-emission of the deposited material during the deposition process by ion or atom bombardment. As the gas pressure is increased, the probability of collisions rises: the working gas acts as a moderator and sputtered atoms move diffusively, reaching the substrates and condensing after undergoing a random walk. If the pressure is further increased, more and more atoms are backscattered and re-deposit on the target, so that the re-deposition rate increases with the gas pressure. On the other hand, increasing gas pressure leads to an increasing discharge current for constant RF power due to increasing plasma potential. As a final result, the sputtering rate may have a maximum value somewhere as the pressure is increased. The entire range from high energy ballistic impact to low-energy thermalized motion is accessible by changing the background gas pressure, called also working gas pressure.

A.1.2 Experimental setup

Figure A.3: A picture of the RF magnetron sputtering apparatus used in this thesis work.

The RF-magnetron sputtering apparatus used is an Alcatel SCM 441 powered by a RF PlasmaTherm HFS-500e power generator (*figure A.3*). Sputtering chamber is equipped with three target holders enabling sequential deposition of three different materials without breaking the vacuum. The cathodes are 6 inch radio-frequency magnetron diode source. The vacuum system is made up of a rotary as primary pump and a turbo-molecular pump. A base vacuum of 10^{-7} mbar can be reached before deposition. A substrate heater along with a PID controller allows the control of substrate temperature from RT to 350 °C (temperature oscillation: ± 2 °C). A step motor moves the substrate holder back and forth over the target to enhance the homogeneity of the film's thickness. Mass-flow controllers allow the controlled injection of working gas (argon) and reactive gas (nitrogen).

A.1.3 Improvements made to the apparatus

During the three years of PhD two important improvements have been made to the apparatus. First of all, in order to improve the thickness homogeneity of the deposited films, a substrate mover was developed. This is composed by a step motor that moves substrates back and forth over the target.

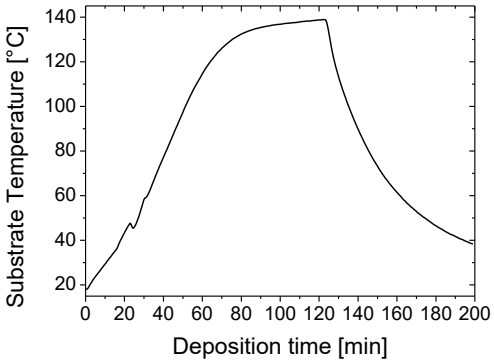

Figure A.4: Substrate temperature dependence on the deposition time. In our apparatus we measured the variation of substrate temperature with deposition time, using the old metallic substrate holder. We deposited ITO at 100 W RF power for 22 minutes and substrate temperature raised up to 47.7 °C. Then we turned to TiO_2 (150 W) and in a 100 minutes of deposition, substrate temperature raised and stabilized at almost 140 °C. Then sputtering was stopped and temperature dropped and decreased continuously.

The second upgrade has been the implementation of a substrate heater with a thermocouple and a PID controller: temperatures range from RT to 350 °C, temperature oscillation: ± 2 °C. With the old substrate holder the substrate temperature could not be measured or set at a desired value, but was dependent from other deposition parameters such as substrate to target distance, RF power and deposition time. Since the first two parameters were always the same, in our case

substrate temperature varied with deposition time. *Figure A.4* shows this dependence. Temperature increases almost constantly at a rate of 2 °C/min and saturates at 140 °C after more than one hour deposition. At least three important observations underline the importance of the substrate heater:

1. For short deposition time, the substrate temperature is very low and this results in amorphous films, which are not useful for our applications.
2. The variation of the substrate temperature during the deposition affects the morphology and crystallinity of the film.
3. The maximum value reached by the substrate temperature is not high enough to get films with a good crystalline degree.

A.2 Pulsed Laser Deposition

Pulsed laser deposition (PLD) is a physical vapour deposition technique where a high-power pulsed laser beam is focused inside a vacuum chamber to strike a target of the material that is to be deposited. For sufficiently high laser energy density, each laser pulse vaporizes or ablates a small amount of the material creating a highly forward-directed plume. The ablation plume provides the material flux for film deposition and growth on a substrate placed in front of the target (*figure A.5*). This process can occur in ultra-high vacuum or in the presence of a background gas, such as oxygen which is commonly used when depositing oxides to fully oxygenate the deposited films.

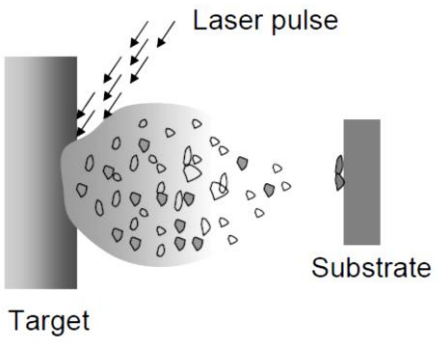

Figure A.5: Schematic presentation of the pulsed laser deposition process.

Pulsed laser deposition can be applied to essentially any material, from simple metals, through binary compounds, to multicomponent high-quality single crystals. Moreover, during PLD many experimental parameters can be changed, which then have a strong influence on the deposited materials. First, the laser parameters such as laser fluence, wavelength, pulse duration, and repetition rate can be altered. Second, the preparation conditions, including target-

to-substrate distance, substrate temperature, background gas and pressure, may be varied, which all influence the film growth. The inherent versatility and flexibility of the technique as well as the speed of the process, has made PLD emerge as one of the most popular techniques for films deposition in the last 25 – 30 years [4].

A typical PLD setup consists of a high energy pulsed laser, a vacuum chamber, target and substrate. While the basic setup is simple relative to many other deposition techniques, the physical phenomena of laser-target interaction and film growth are quite complex. Here the mechanism for lasers with pulse duration of ns will be discussed, for shorter pulse durations further considerations should be made. We can divide the process into three parts:

1. Laser – target interaction
2. Ablated material interaction with laser and background gas
3. Nucleation and growth on the substrate

A.2.1 Laser – target interaction

The interaction of the laser beam with the target depends on several parameters including the absorption coefficient and reflectivity of the target, the wavelength, pulse duration and fluence of the laser. When the laser pulse is absorbed by the target, energy is first converted into electronic excitation, then it is transferred to the lattice through electron-phonon interactions within picoseconds. There is an energy threshold over which the ablation process can start. Indeed, efficient ablation of the target material requires the non-equilibrium excitation of the ablated volume to temperatures well above the melting point. This generally requires short laser pulses (< ns), high energy density, and high absorption by the target material. For ceramic targets, this is most easily achieved via the use of short wavelength lasers operating in the ultraviolet [4].

There are three thermodynamic processes which lead to the ablation of the material from the target irradiated by the laser [5]:

1. Evaporation (or normal vaporization)
2. Normal boiling
3. Phase explosion (or explosive boiling)

The relevance of the three processes depends on the laser pulse duration as well as on the temperature attained in the irradiated zone.

Normal vaporization is the emission of particles from the target surface and it includes sublimation and evaporation. Normal vaporization could occur with metal or semiconductor material and it does not imply any threshold value of temperature. However, it was observed that for low laser fluence (i.e. low temperatures) and for short pulses (time scales of < 1ns) there is no relevant vaporization.

Normal boiling involves heterogeneous nucleation of vapour bubbles in the irradiated volume of the target. In the case of liquids, the vapour bubbles initiate heterogeneously from defects or impurities then tend to diffuse and may escape from the liquid outer surface if the temperature is slightly higher than the boiling temperature (T_b) for sufficient time interval. In this case T_b is a threshold temperature. Since T_b is always higher than the melting temperature (T_m) of a material, wavelike structures on the target surface may be observed after laser irradiation due to localized melting.

The third process, called explosive boiling or phase explosion, happens when short pulses (ns ÷ fs duration) and high energy density heat up the target material at a rate of ~ $10^8 \div 10^{10}$ K/s and a temperature of about 0.9 Tc (critical temperature) is reached. Strong homogeneous nucleation occurs in a super-heated metastable liquid and just below the target surface. At about 0.9 Tc vapour and liquid nano-droplets leave the surface, turn into the plasma plume and finally they deposit in the substrate as nanoparticles.

A.2.2 Ablated material interaction with laser and background gas

The species ejected from the target expand adiabatically and interact with the laser (inverse bremsstrahlung and photo-ionization processes) forming a plasma plume composed of atoms, ions, electrons and photons. At the end of the laser pulse, ions recombine with electrons and the excited states lose their potential energy by radiative emission [6]. After the termination of the laser pulse, the plume expands adiabatically in three dimensions. If the expansion takes place in vacuum, the shape and velocity distribution in the plume will reach asymptotically constant values. If the ablation takes place in a background gas, the expansion is initially driven by the high plume pressure as if it were occurring in vacuum, then is slowed by the interaction with ambient gas. After several μs, the plume expansion is entirely determined by the interaction of the plume atoms with the atoms and molecules of the background gas [6]. Therefore, ambient gas type and pressure have significant influence on the deposited material properties and is used essentially for two reasons. Firstly, it reduces the kinetic energies of the ablated species, from the typical hundreds of eV up to values much lower than 1 eV. This can be useful for example

to control the morphology and the compressive strain of the deposited film. Secondly, background gas may participate actively in the chemistry of the deposited film. This is the case of reactive ablation where the targets consist of the constituent cations, while the anion is supplied by the background gas. For example we used a metallic iron target and oxygen as the background gas to obtain iron oxide.

A.2.3 Nucleation and growth on the substrate

The nucleation process and growth kinetics of the film depend on many tuneable parameters such as: laser fluence, substrate temperature, background pressure and deposition rate. One of the properties that makes PLD particularly attractive is the preservation of the stoichiometry when using multicomponent targets. Indeed, unlike thermal evaporation, the non-equilibrium nature of phase explosion, due to absorption of high laser energy density by a small volume of material, makes the ablation process independent from the vapour pressure of the target constituents.

Pulsed laser deposition can be used for the deposition of compact or porous films, thin or thick samples. Moreover, if the background pressure is sufficiently high for heterogeneous particle nucleation, nanoparticles form in the gas phase and deposit on the substrate. In this way NPs-assembled coatings are obtained, which are very interesting for catalysis applications.

A.2.4 Experimental apparatus

The apparatus for PLD (*figure A.6*) was designed and realized by the IdEA laboratory of Trento University. The high energy pulsed radiation is given by an excimer laser (KrF), Lambda Physics LPX 220i, with an operating wavelength of 248 nm and a nominal pulse duration of 20 ns. The repetition rate can be varied in the range 1-200 Hz. The energy per pulse can be tuned by changing the pumping high voltage. The laser beam passes through a slit where it is cleaned of haloes. It is deflected by 90° by means of a dielectric mirror and then focused by a 40 cm focal length lens, which is mounted on a slide permitting it to be translated along the beam direction from the focusing position (where the beam is focused onto the target) away by about ±15 cm. The slide is used to change the energy fluence on the target. The focused beam finally enters the treatment chamber through a fused silica window and impinges on the target at 45°. The vacuum system was developed in a way to allow the achievement of a wide range of pressures. Generally thin-film deposition processes require high vacuum conditions and controlled atmosphere. It consist of a primary pump (Scroll pump) and a wide range turbomolecular pump (Varian type V550). To preserve the turbomolecular pump, when an

ambient gas is introduced into the treatment chamber, the pump itself is separated from the chamber by a gate valve and pumping occurs only through a bypass with an angle valve with adjustable transverse section. The gas mixture is introduced into the vacuum chamber through two mass-flow meters, which receive a feedback pressure signal from a capacitance–pressure transducer, thus maintaining constant the pressure and the partial pressure ratio.

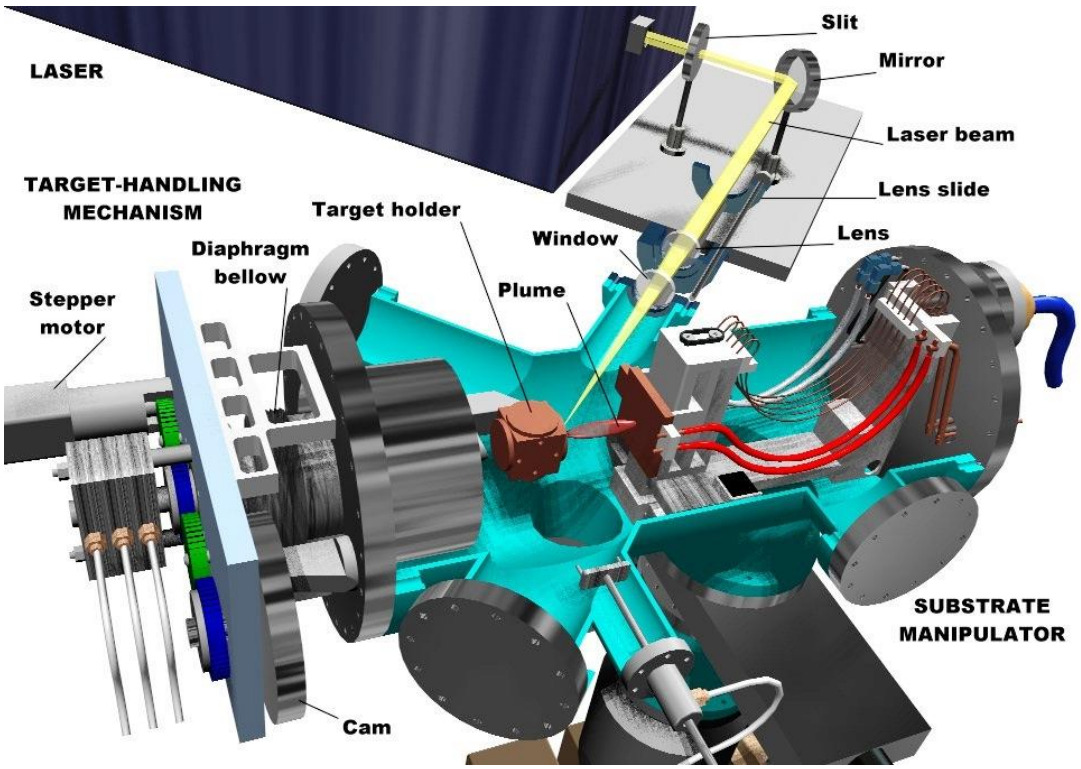

Figure A.6: A schematic 3D view of the laser deposition apparatus

A complete description of the PLD apparatus can be found in [7].

A.3 References

1. Chapman, B.N., *Glow discharge processes*. 1980: Wiley.
2. Lieberman, M.A. and A.J. Lichtenberg, *Principles of plasma discharges and materials processing*. 2005: John Wiley & Sons.
3. Thornton, J.A., *Influence of apparatus geometry and deposition conditions on the structure and topography of thick sputtered coatings.* J Vac Sci Technol, 1974. **11**(4): p. 666-670.
4. Chrisey, D.B. and G.K. Hubler, *Pulsed laser deposition of thin films.* 1994.
5. Miotello, A. and R. Kelly, *Laser-induced phase explosion: new physical problems when a condensed phase approaches the thermodynamic critical temperature.* Applied Physics A, 1999. **69**(1): p. S67-S73.
6. Phipps, C., *Laser ablation and its applications*. Vol. 129. 2007: Springer.
7. Bonelli, M., C. Cestari, and A. Miotello, *Pulsed laser deposition apparatus for applied research.* Measurement Science and Technology, 1999. **10**(3): p. N27-N30.

Appendix B

Characterization techniques

B.1 Scanning Electron Microscopy

Scanning electron microscopy is a high resolution microscopy technique based on using a focused beam of electrons to irradiate a sample material in order to investigate its surface topography, morphology and composition. Interaction of beam electrons with sample's atoms produces several signals containing information about the material. Electron microscopes were developed when the wavelength became the resolution-limiting factor in light microscopes.

Indeed, the imaging resolution of a microscope is limited by aberration and by diffraction. These two phenomena have different origins and are unrelated. Aberrations can be explained by geometrical optics and can in principle be solved by increasing the optical quality of the system. On the other hand, diffraction comes from the wave nature of light and is determined by the finite aperture of the optical elements. The lens' circular aperture is analogous to a two-dimensional version of the single-slit experiment. Light passing through the lens interferes with itself creating a ring-shape diffraction pattern, known as the Airy pattern (*figure B.1*). The bright region in the centre is called the Airy disk and its angular radius is given by[1]:

$$\theta = 1.22\frac{\lambda}{D}$$

where: θ is the angular resolution in radians, λ is the wavelength of light in meters, and D is the diameter of the lens aperture in meters. Two adjacent points in the object give rise to two diffraction patterns. If the angular separation of the two points is smaller than the Airy disk angular radius, then the two points cannot be resolved in the image, but if their angular

[1] The factor 1.220 is derived from a calculation of the position of the first dark circular ring surrounding the central Airy disc of the diffraction pattern. The calculation involves a Bessel function—1.220 is approximately the first zero of the Bessel function of the first kind, of order one (i.e., J_1), divided by π.

separation is greater than this, distinct images of the two points are formed and they can therefore be resolved (*figure B.1*). This is the so-called *Rayleigh criterion*.

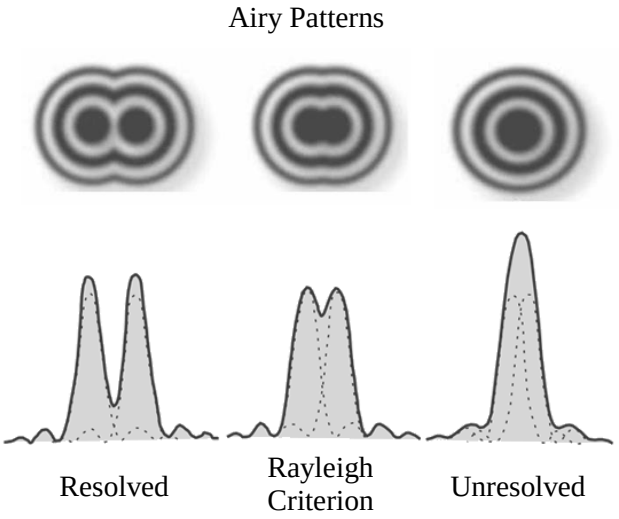

Figure B.1: Intensity curves for the radial distribution of the diffracted light for different separations and the relative Airy patterns.

The average wavelength used in a visible light microscope is 550 nm which results in a theoretical resolution limit of about 200 – 250 nm. In order to get a better resolution either bigger lenses (as in telescopes) or shorter wavelengths can be used. Electrons have a wavelength 10^5 times shorter than visible light, enabling better resolution. Furthermore, electric and magnetic fields can be used to shape the paths followed by electrons similar to the way glass lenses are used to bend and focus visible light. These two observations were crucial for the construction of a scanning electron microscope.

B.1.1 Operation of an SEM

Figure B.2 shows a schematic representation of an SEM. The electron gun at the top of the column produces an electron beam that is accelerated and passes through a series of electromagnetic lenses and apertures. In this way, the electron beam is focused into a fine spot as small as 1 nm in diameter on the specimen surface. A final lens deflects the beam in the x and y axes so that it scans in a raster fashion over a rectangular area of the sample surface. Interaction of the electron beam with the sample results in the generation of a variety of signals: reflected electrons, secondary electrons, Auger electrons, transmitted electrons, cathodoluminescence (photons) and X-rays. All these phenomena are interrelated and all of them depend to some extent on the topography, the atomic number and the chemical state of the specimen. Different types of signals can emerge from different volumes of interaction

(*figure B.3*). The size and the shape of the volume depends on many factors, including beam energy and sample composition. The signals are stored in computer memory and then mapped as variations in brightness on the image display. The most commonly imaged signals in SEM are secondary electrons and back-scattered electrons. Characteristic X-rays are also widely used in SEM for elemental microanalysis (in this case a specific detector is required).

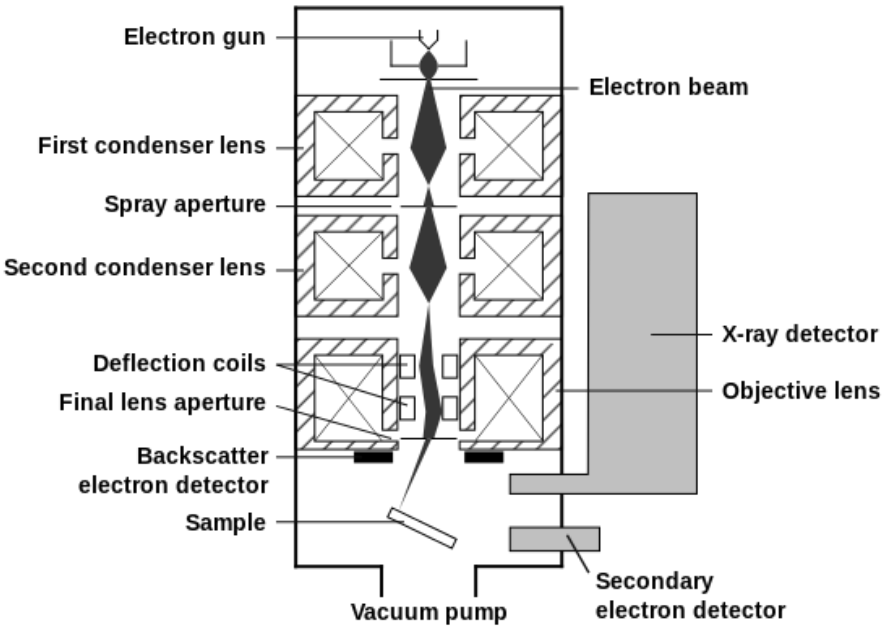

Figure B.2: Scheme showing the main components of a scanning electron microscope.

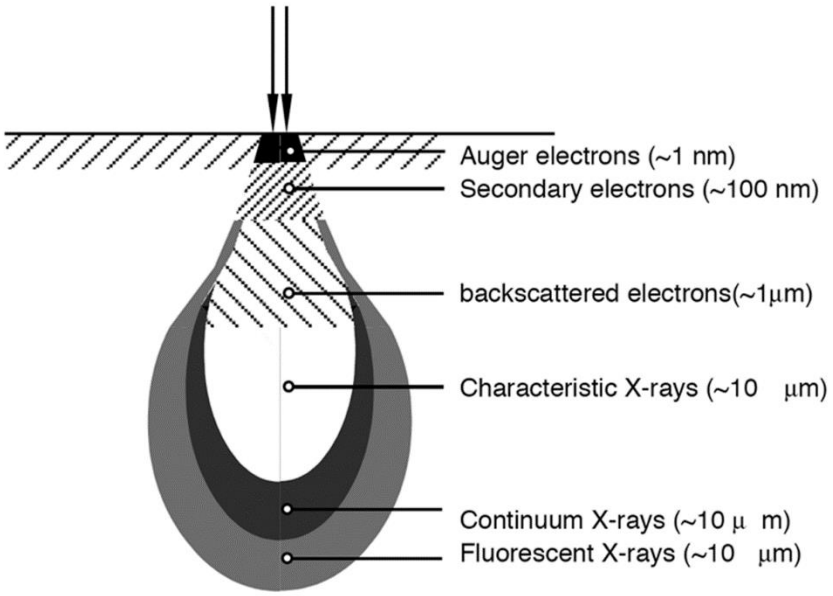

Figure B.3: Interaction volume for the various scattering types, and imaging modes. Back-scattered electrons are seen to have a much larger interaction volume than secondary electrons.

Secondary electrons (SEs) are produced as a result of the interactions between energetic beam electrons and the weakly bound conduction-band electrons in metals or valence electrons in semiconductors and insulators. Secondary electrons have low kinetic energy (< 50 eV) so only the electrons produced near the surface can escape from the sample. The signal of SEs varies with the topography of the sample surface much like an aerial photograph: edges are bright, recesses are dark. Indeed, the main cause of the image contrast is the existing angle between the incident beam and the surface. The ratio of the size of the displayed image to the size of the area scanned on the specimen gives the magnification. Increasing the magnification is achieved by reducing the size of the area scanned on the specimen [1].

Backscattered electrons (BSEs) are elastically scattered electrons by the nuclei of the atoms in the specimen. BSEs exit from the surface with a high energy and contain information on chemical composition of the elements in the specimen. The number of BSEs increases with the atomic number Z of the atoms, so a material with a high Z will appear brighter on the image than a material having a lower Z [1].

The interaction volume for the various scattering types, and imaging modes is illustrated in *figure B.3* where BSE electrons are seen to have a much larger interaction volume than SE electrons. The larger interaction volume results in BSE mode having a lower resolution than SE mode.

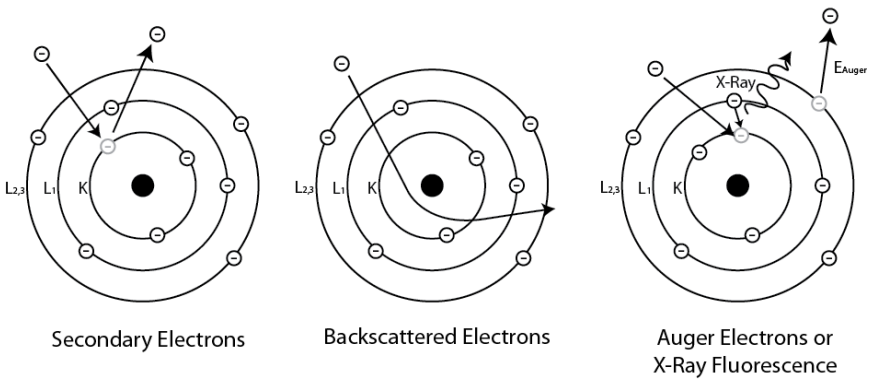

Figure B.4: Various modes of electron emission from incident x-rays or electrons.

During inelastic scattering of the beam electrons, x-rays can be formed by two distinctly different mechanisms: Bremsstrahlung and inner-shell ionization processes. In the first case, beam electrons undergo deceleration in the Coulombic field of the atom and the lost energy is emitted as x-rays. Because of the random nature of this interaction, the electron may lose any amount of energy in a single deceleration event. This results in a continuum spectrum of x-rays,

which is not useful for material's analysis. In the second case, a beam electron interacts with a tightly bound inner-shell electron, ejecting the atomic electron and leaving a vacancy in that shell; the atom is left as an ion in an excited state and relaxes to its ground state through a limited set of allowed transitions of outer-shell electrons to fill the inner-shell vacancy. The energies of the electrons in the shells are sharply defined, with values characteristic of the atomic species. The energy difference of the transition is therefore also a characteristic value, and this excess energy can be released from the atom in one of two ways:

1. in the Auger process, the difference in shell energies can be transmitted to another outer-shell electron, ejecting it from the atom as an electron with specific kinetic energy;
2. in the characteristic x-ray process, the difference in energy is expressed as a photon of electromagnetic radiation that is sharply defined in energy, in contrast to the bremsstrahlung process, which produces photons spanning an energy continuum.

The number and energy of the characteristic x-rays can be measured by an energy-dispersive spectrometer (EDS), which provides information about the elemental composition of the sample and concentration of each element [1].

B.2 Raman spectroscopy

Raman spectroscopy is a spectroscopic technique used to observe vibrational, rotational, and other low-frequency modes in a system. It relies on inelastic scattering, or Raman scattering, of monochromatic light, usually from a laser in the visible, near infrared, or near ultraviolet range.

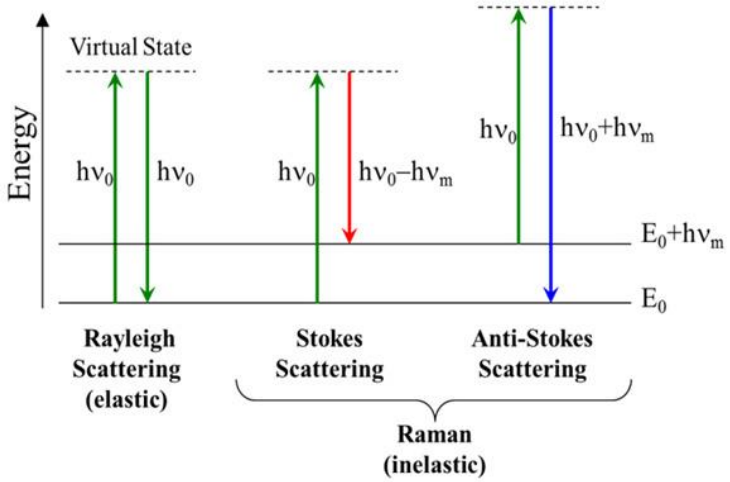

Figure B.5: Diagram representing quantum energy transitions for Rayleigh and Raman scattering.

Incident photons may interact with the molecules and excite them to a virtual energy state (*figure B.5*). When this occurs, there are three different potential outcomes. First, the molecule

can relax back down to the original state and emit a photon of equal energy to that of the incident photon. This process is referred to as elastic (or Rayleigh) scattering. In some cases, the molecule can relax to a different rotational and/or vibrational (rovibronic) state and emit a photon with a different energy. If the final vibrational state of the molecule is more energetic than the initial state, the inelastically scattered photon will be shifted to a lower frequency for the total energy of the system to remain balanced. This shift in frequency is designated as a Stokes shift (second outcome). If the final vibrational state is less energetic than the initial state, then the inelastically scattered photon will be shifted to a higher frequency, and this is designated as an anti-Stokes shift (third outcome).

In solid-state physics, Raman spectroscopy is used to characterize materials, measure temperature, find the crystallographic orientation of a sample, and for other applications. As with single molecules, a given solid material has characteristic phonon modes that can help an experimenter to identify it. In addition, Raman spectroscopy can be used to observe other low frequency excitations of the solid, such as plasmons, magnons, and superconducting gap excitations. Raman scattering by an anisotropic crystal gives information on the crystal orientation.

A Raman spectrometer consists of a source of monochromatic light (laser), illumination system, focusing lenses, an optical filter, detectors and computer control software. The sample is irradiated by a beam of monochromatic light and the scattered photons are focused on an optical filter which separates low intensity Raman scattered photons (around 0.001% of total intensity) from high intensity Rayleigh scattered photons. The Raman scattered photons are amplified and transferred toward a detector. Plotting the intensity of Raman scattered light versus frequency results in a Raman spectrum of the sample. Generally, Raman spectra are plotted with respect to the laser frequency such that the Rayleigh band lies at 0 cm^{-1}. On this scale, the band positions will lie at frequencies that correspond to the energy levels of different functional group vibrations.

For the investigation of small areas, the laser can be passed through an optical microscope, thus reducing the sample area. This technique is generally referred to as micro-Raman. In a micro-Raman spectrometer monochromatic light, generated by a laser, is reflected by an optical filter towards the microscope and the focused beam impinges on a target where transmission, absorption, elastic and inelastic scattering occur. The Raman scattered light is transmitted through the filter towards the confocal slit-hole at the entrance of the spectrograph. The

spectrograph in turn disperses the polychromatic Raman signal onto CCD multichannel detector.

B.3 X-ray Photoelectron Spectroscopy

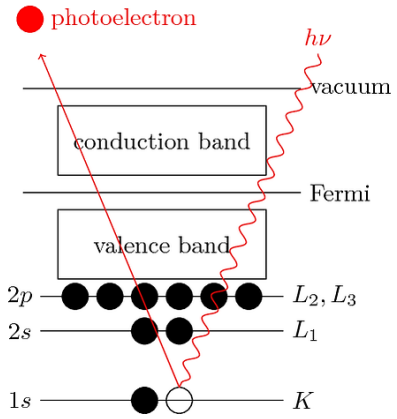

Figure B.6: The photoemission process involved in XPS. The discs represent electrons and the bars represent energy levels within the material being analysed.

X-ray photoelectron spectroscopy (XPS) is a surface-sensitive quantitative spectroscopic technique that measures the elemental composition at the parts per thousand range (0.1 at. %), chemical state and electronic state of the elements that are present within the first surface layers of a material. The sample is placed in an ultrahigh vacuum environment and exposed to a low-energy, monochromatic x-ray source. The incident x-rays (of energy around 1.5 keV) cause the ejection of electrons from the atoms of the sample (photoelectric effect, *figure B.6*). An electron energy analyser is used to measure the energy of the emitted photoelectrons and a detector to count their number. The number of photoelectrons as a function of their energy gives the XPS spectrum of the sample.

The kinetic energy of the generated photoelectrons is given by:

$$K_e = h\nu - BE - \phi$$

where $h\nu$ is the incident photon energy, BE the binding energy of the emitted electron in the atom and ϕ is the work function of the analysed material. The kinetic energy of a photo-emitted electron is a function of its binding energy and thus is characteristic of the element from which it was emitted. For this reason, the energy corresponding to each peak in the XPS spectrum is characteristic of an element present in the sampled volume and can be used for composition analysis. The area under a peak in the spectrum is a measure of the relative amount of the element represented by that peak. The peak shape and precise position indicates the chemical state for the element. XPS is a surface sensitive technique because only those electrons

generated near the surface escape without losing energy and are detected. The photoelectrons of interest have relatively low kinetic energy. Due to inelastic collisions within the sample's atomic structure, photoelectrons originating more than 20 to 50 Å below the surface do not contribute to XPS signals.

B.4 UV-Vis spectroscopy

UV-visible spectroscopy, also known as electronic spectroscopy, refers to the absorption of electromagnetic radiation by atoms or molecules that leads to valence electrons promotion from ground state to excited states. Generally, the explored range of wavelengths includes UV (10-200 nm), near UV (200-380 nm) and visible (380-780 nm) light. Sometimes, also the near infrared region (>780 nm) is investigated. To encompass the majority of electron transitions the spectrum between 190 and 900 nm is usually considered. Valence electrons can be found in one of three types of electron orbital:

1. single, or σ, bonding orbitals;
2. double or triple bonds (π bonding orbitals); and
3. non-bonding orbitals (lone pair electrons).

Sigma bonding orbitals tend to be lower in energy than π bonding orbitals, which in turn are lower in energy than non-bonding orbitals. When electromagnetic radiation of the correct frequency is absorbed, a transition occurs from one of these orbitals to an empty orbital, usually an antibonding orbital, σ* or π*. For molecules, electrons are promoted from the highest occupied molecular orbital to the lowest unoccupied molecular orbital.

There are different mechanisms of light absorption by semiconductors: interband (fundamental) absorption, dopant absorption, excitonic absorption, absorption by free charge carriers, absorption by crystalline lattice. The fundamental absorption leads to the generation of electron-hole pairs as a result of optical excitation of electrons from the valence band to the conduction band. Since the minimum quantum energy sufficient to electron excitation from the valence band to the conduction band is equal to the band gap, the threshold energy of the fundamental absorption is related to the band gap of the semiconductor.

The amount of absorbed light is expressed as either transmittance (T) or absorbance (A) of the material. Transmittance is given in terms of fraction or percentage and is defined as:

$$T(\lambda) = \frac{I(\lambda)}{I_0(\lambda)} \quad or \quad \%T = 100\left(\frac{I}{I_0}\right)$$

where I is the intensity of transmitted light and I_0 is the intensity of incident light. Absorbance is defined as:

$$A(\lambda) = -\log T(\lambda)$$

The intensity of the absorbed light follows the Lambert-Beer's law:

$$I(\lambda) = I_0(\lambda)e^{-\alpha(\lambda)d}$$

where d is the thickness of the sample and $\alpha(\lambda)$ is the absorption coefficient of the material. A common way to extract the indirect and direct gaps from optical absorption spectra is the Tauc plot, which is based on the assumption that the energy-dependent absorption coefficient $\alpha(E)$ can be expressed as:

$$\alpha(E) = a\left(E - E_g^{direct}\right)^{0.5} + b\left(E - E_g^{indirect} + - E_{phonon}\right)^2$$

with two parameters a and b, the indirect and direct gaps E_g, and the phonon energy E_{phon}. Thus, straight line segments in $(\alpha E)^2$ indicate direct gaps and straight-line segments in $(\alpha E)^{0.5}$ indicate indirect gaps [2].

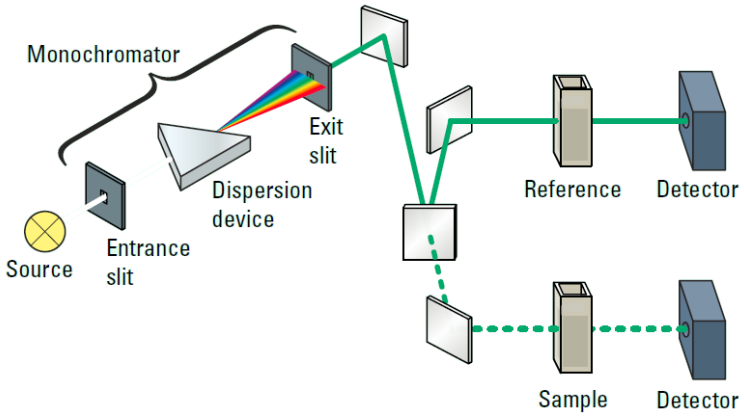

Figure B.7: Schematic optical system of a common double-beam spectrophotometer [3].

A UV-Vis spectrometer (*figure B.7*) consists of a light source, a monochromator, a beam splitter, two holders (one for the sample and one for the reference), and two photodiode detectors. The light source should be stable and should provide sufficient intensity over a large region of the electromagnetic spectrum. A combination of tungsten-halogen and deuterium arc bulbs provide visible and UV light, respectively. The monochromator separates the light emitted by the source into its component wavelengths. The beam is separated into two beams with equal intensity: one beam is used as the reference and the other passes through the sample. The reference beam intensity is taken as 100% Transmission (or 0 Absorbance), and the measurement displayed is the ratio of the two beam intensities.

B.4 Electrochemical and Photo-electrochemical characterization

In a three electrodes configuration photo-electrochemical cell, the potentiostat allows controlling/measuring simultaneously the potential between the working electrode and the reference electrode and the current between the working and the counter electrode. This consents performing different types of measurements, which provide complementary information on the properties of the working electrode. In this thesis, we did three different measurements to characterize electrocatalytic performance of the samples: linear sweep voltammetry, cyclic voltammetry and chronoamperometry.

In linear sweep voltammetry (LSV) experiments, the current (I) at the working electrode is measured while the potential (V) between the working electrode and the reference electrode is swept linearly in time. The slope of V(t) linear graph is called the voltage scan rate and it can be altered by changing the time interval taken for a sweep. The scan rate of voltage sweep is generally set in a range of 10-100 mV/sec. Since the electric current is proportional to the reaction rate over the electrode, the analysis of LSV data provides important information on the electrocatalytic activity of the electrodes. A Tafel relationship describes well the catalytic performance of electrodes for the hydrogen or oxygen evolution half-reactions:

$$\eta = b \cdot \log\left(\frac{I}{I_0}\right)$$

where η is the overpotential, I is the measured current, I_0 is the exchange current, and b is called Tafel slope. The overpotential is the potential difference (voltage) between the potential at which the reaction starts and its standard potential. The Tafel slope is a measure of the potential increase required to increase the resulting current one order of magnitude, usually reported as mV/decade. The exchange current corresponds to the intercept at $\eta = 0$, extrapolated from a linear portion of a plot of η versus log(I) (i.e., a Tafel plot). This reaction rate under dynamic equilibrium is also described in terms of geometric area as the exchange current density, J_0 (e.g., A cm^{-2}). Qualitatively, J_0 can be thought of as a measure of how vigorously the forward and reverse reactions occur during dynamic equilibrium, while b is a measure of how efficiently the electrode can respond to an applied potential to produce current [4].

Cyclic voltammetry experiments involve the measurement of the current between working electrode and counter electrode while varying the potential between the working electrode and the reference electrode. In this case, however, the variation of the potential is repeated back and forth for a fixed number of cycles. The voltage range typically includes the redox potentials of

the reactions under study and so this measure allows to evaluate the redox potential values, the electrochemical reaction rates and the reversibility of the reaction. If the reaction is irreversible, cyclic voltammetry will not give any additional data as compared to linear sweep voltammetry. This technique is used also for the investigation of electrode's stability during electrocatalytic performance. If the electrode is stable the J/V curves of the single cycles will overlap, otherwise a difference between the cycles will be detected.

Another type of voltammetry which provides information about electrode's stability is the Chronoamperometry (CA) analysis. Chronoamperometry refers to the measurement of the current generated at the electrode at fixed applied voltage for a given time interval. The potential is stepped from a value where the species of interest are not reduced (or oxidized) to a value where the current is diffusion-controlled, i.e. there is no mass-transport saturation effects; furthermore, the step potential must be selected so that only the redox species is electrolyzed, in order to avoid currents due to undesired reactions in the solution.

B.5 References

1. Buckley, A., *JI Goldstein, DE Newbury, P. Echlin, DC Joy, AD Romig Jr, CE Lyman, C. Fiori & E. Lifshin 1992. Scanning Electron Microscopy and X-Ray Microanalysis. A Text for Biologists, Materials Scientists, and Geologists, xviii+ 820 pp. New York, London: Plenum Press. Price US $49.50 (hard covers). ISBN 0 306 44175 6.* Geological Magazine, 1993. **130**(03): p. 402-403.
2. Meinert, M. and G. Reiss, *Electronic structure and optical band gap determination of NiFe2 O4.* Journal of Physics: Condensed Matter, 2014. **26**(11): p. 115503.
3. Owen, T., *Fundamentals of modern UV-Visible spectroscopy, agilent technologies*. 2000, Germany.
4. Walter, M.G., et al., *Solar water splitting cells.* Chemical reviews, 2010. **110**(11): p. 6446-6473.

Publications

Papers:

1. Nainesh Patel, Trupti Warang, Rohan Fernandes, Claudio Cestari, Damiano Avi, Nicola Bazzanella, Raju Edla, Zakaria El Koura, Antonio Miotello: "*A new apparatus for carbon monoxide oxidation studies performed over thin film catalysts*" Meas. Sci. Technol. 24 (2013) 125901

2. Raju Edla, Nainesh Patel, Zakaria El Koura, Rohan Fernandes, Nicola Bazzanella, Antonio Miotello: "*Pulsed laser deposition of Co_3O_4 nanocatalysts for dye degradation and CO oxidation*" Applied Surface Science 302 (2014) 105–108

3. Michele Orlandi, Stefano Caramori, Federico Ronconi, Carlo A. Bignozzi, Zakaria El Koura, Nicola Bazzanella, Laura Meda, and Antonio Miotello: *"Pulsed-Laser Deposition of Nanostructured Iron Oxide Catalysts for Efficient Water Oxidation"* ACS Appl. Mater. Interfaces 6 (2014) 6186−6190

4. Zakaria El Koura, Nainesh Patel, Raju Edla, Antonio Miotello: "*Multilayer films of indium tin oxide/TiO_2 codoped with vanadium and nitrogen for efficient photocatalytic water splitting*" Int. J. Nanotechnol., Vol. 11 Nos. 9/10/11 (2014) 1017-1027

5. Enrico Binetti, Zakaria El Koura, Nicola Bazzanella, Gianfranco Carotenuto, Antonio Miotello: *"Synthesis of mesoporous ITO/TiO_2 electrodes for optoelectronics"* Materials Letters 139 (2015) 355–358

6. Enrico Binetti, Zakaria El Koura, Nainesh Patel, Alpa Dashora, Antonio Miotello: *"Rapid hydrogenation of amorphous TiO_2 to produce efficient H-doped anatase for photocatalytic water splitting"* Applied Catalysis A: General 500 (2015) 69–73

7. Z. El Koura, M. Cazzanelli, N. Bazzanella, N. Patel, R. Fernandes, G. E. Arnaoutakis, A. Gakamsky, A. Dick, A. Quaranta, and A. Miotello: *"On the effect of Cu and N codoping on RF-sputtered TiO_2 photo-catalyst films"* (Manuscript in preparation).

8. M. Orlandi, N. Dalle Carbonare, A. Mazzi, Z. El Koura, N. Bazzanella, S. Caramori, N. Patel, C. A. Bignozzi, A. Miotello: *"A transparent water oxidation catalyst for photo-anodes functionalization"* (Manuscript in preparation).

Book chapter:

Martino Bernard, Allegra Calabrese, Tatevic Chalyan, Zakaria El Koura, Francesco Dallari, Simone Donadello, Nicola Gatti, Teodoro Klaser, Matteo Leonardi, Veronica Regazzoni, Alberto Sartori "*Industrial Torque sensor*"; Industrial Problem Solving with Physics (IPSP – 2015).

Attended conferences

1) XXIII SILS (Società Italiana Luce di Sincrotrone) Meeting 8-10 July 2015, Trento (Italy).
    a. Poster: *"Local structure and oxidation state of Vanadium (V) in V-doped TiO_2 nanostructured thin films for photocatalytic applications"*
2) Industrial Problem Solving with Physics (IPSP – 2015), 20 – 25 July 2015, Trento (IT)

3) XAFS characterization of V-doped TiO_2 and V-N codoped TiO_2 at the European Synchrotron Radiation Facility (ESRF – Grenoble, France), May 2015

4) 2nd Euro-Mediterranean Hydrogen Technologies (EmHyTeC - 2014) Conference, 9-12 December 2014, Taormina (Italy);
    a. Talk: *"Improved H_2 production by photocatalytic water splitting using multilayer films of TiO_2 codoped with Copper and Nitrogen"*
    b. Poster: *"Doping TiO_2 with hydrogen for efficient solar water splitting"*

5) European Materials Research Society (E-MRS) Spring Meeting, 27-31 May 2013, Strasbourg (France);
    a. Poster: *"Multilayer films of Indium Tin Oxide/TiO_2 codoped with Vanadium and Nitrogen for efficient photocatalytic water splitting"*

Acknowledgments

I would like to express my gratitude to Prof. Antonio Miotello for giving me the opportunity to work in his research group. I highly appreciate his unrestricted and permanent support in all respects and his extensive proof reading of this thesis.

Sincere thanks go to all the people who spent their time on the projects described in this thesis: it's been a pleasure working with you all.

In particular, I would like to express special gratitude to the following people:

Nicola Bazzanella and Raju Edla, with whom I have been working for more than four years, learning from their experience and enjoying their company.

Nainesh Patel, who followed me in the first period of PhD, for his valuable suggestions and guidance at the beginning of my research career.

Binetti Enrico and Orlandi Michele, my two mentors in the subsequent period.

Alberto Mazzi, Loredana Schiavo, and Federico Gorrini, my PhD mates, for the nice time spent together. I wish to all of them a good luck for their dissertation and for their future work life.

Claudio Cestari, Luigino Vivaldi and Marco Bettonte: this work could not have been completed without their technical support.

Massimo Cazzanelli, with whom unfortunately I worked only in the last period and did not get the chance to learn much from him.

Luca Ravelli, Pushkar Patil, and David Roilo

Thank you all for being such a fantastic group of people to work with.

Un grazie dal profondo del cuore:

A Valentina, per avermi supportato e sopportato in questi anni.

Ai miei genitori, che mi hanno sempre incoraggiato a studiare ed a migliorarmi, giorno dopo giorno.

Alle mie sorelle, che mi fanno disperare perché sembra che a nessuna di loro interessi la fisica. Spero che questa passione contagi almeno una di voi!

A tutte le persone che, consapevolmente o non, mi hanno aiutato a crescere.

الحمد لله اولا واخرا

وما توفيقي الا بالله عليه توكلت وهو رب العرش العظيم